AD NUMBER: AD0342463
CLASSIFICATION CHANGES
TO: Unclassified
FROM: Confidential
LIMITATION CHANGES
TO: Approved for public release; distribution is unlimited.
FROM: Distribution authorized to U.S. Government Agencies and their Contractors; Administrative/Operational Use; 31 Jul 1963. Other requests shall be referred to Office of Naval Research, Arlington, VA 22203.
AUTHORITY
C to U per DoDD 5200.1 dtd 31 Dec 1972; ST-A per ONR ltr dtd 4 May 1977

GENERAL DECLASSIFICATION SCHEDULE

IN ACCORDANCE WITH
DOD 5200.1-R & EXECUTIVE ORDER 11652

THIS DOCUMENT IS:

CLASSIFIED BY [redacted]

Subject to General Declassification Schedule of Executive Order 11652-Automatically Downgraded at 2 Years Intervals- DECLASSIFIED ON DECEMBER 31, 72.

BY

Defense Documentation Center
Defense Supply Agency
Cameron Station
Alexandria, Virginia 22314

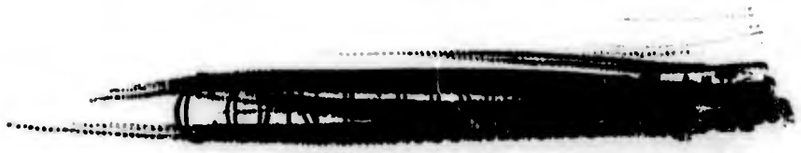

GENERAL DYNAMICS
ELECTRIC BOAT
GROTON, CONNECTICUT

~~CONFIDENTIAL~~

Contract NOnr 3383(00)
NR 097-353
Office of Naval Research

FEASIBILITY OF A NOVEL ELECTRIC POWER PROPULSION SYSTEM (NEPPS) FOR A SUBMARINE

Vol. III of III, Hydrodynamic Model Tests

by
A. J. Izzo

Applied Mechanics Section
Research and Development Department
General Dynamics/Electric Boat
Groton, Connecticut

Approved by: B. S. Ryskiewich
B.S. Ryskiewich, NEPPS
Project Engineer

L. H. Chen
L. H. Chen, Head of Basic
Engineering Division

C411-63-020
July 31, 1963

~~CONFIDENTIAL~~

FOREWORD

The Novel Electric Power Propulsion System (NEPPS) is a submarine propulsion concept consisting of a pair of free flooding AC motors, the rotors of which rotate around the stators. Segments of the envelope of the hull form the outer housings of the rotors and rotate with them. Propeller blades are mounted on the rotating segments of the hull and comprise a pair of counter-rotating propellers of unusually large ratio of hub diameter to tip diameter.

The potential advantages of the system over those of present submarines prompted a group of three correlated studies:

I An Engineering Study to determine the system's engineering feasibility and theoretical performance adequacy.

II An Operations Research Study to determine the operational advantages to be gained by adapting the system to an attack and/or FBM class submarine.

III Hydrodynamic Model Tests to support the theoretical predictions in I.

This report presents the results of the third study. It includes an evaluation of ship performance based on wind tunnel and water tunnel tests of a hydrodynamic model.

TABLE OF CONTENTS

LIST OF FIGURES

LIST OF FIGURES (CONT)

LIST OF TABLES

NOMENCLATURE

A - Maximum cross section area of hull, sq ft

C_d - Drag Coefficient, $\frac{D}{1/2\rho A V_o^2}$

C_D - Drag Coefficient, $\frac{D}{1/2\rho S_w V_o^2}$

C_f - Total coefficient of frictional resistance

C_{f_o} - Coefficient of frictional resistance due to ship speed

C_{f_s} - Coefficient of increment of frictional resistance due to propulsor slipstream

ΔC_f - Added coefficient of friction due to roughness

C_r - Coefficient of residual resistance

C_P - Pressure coefficient, $\frac{P - p_o}{1/2\rho V_o^2}$

C_Q - Torque coefficient, $\frac{Q}{1/2\rho A V_o^2 D_m}$

D - Drag force, pounds, positive downstream

D_m - Maximum diameter of hull

e_P - Propulsive coefficient, EHP/SHP

EHP - Effective horsepower, $\frac{DV_o}{550}$

J - Advance ratio, V_o/nD_m

K_Q - Propeller torque coefficient, $\frac{Q}{\rho D_m^5 n^2}$

K_T - Propeller thrust coefficient, $\frac{T}{\rho D_m^4 n^2}$

L - Length of hull, feet

N - Rotor speed, revolutions/minute

n - Rotor speed, revolutions/second

P - Local total pressure, lb/sq ft

p_o - Free stream static pressure, lb/sq ft

p - Local static pressure, lb/sq ft

p_v - Vapor pressure, lb/sq ft

Q - Torque, ft lb

R_m - Maximum radius of hull, feet

r - Radial coordinate, feet

S_W - Wetted surface, sq ft

SHP - Shaft horsepower, $\frac{2\pi nQ}{550}$

T - Propeller thrust, lb

V_o - Free stream velocity, $\sqrt{\frac{p - p_o}{1/2\rho}}$, ft/sec

V_1 - Total velocity, $\sqrt{\frac{P - p_o}{1/2\rho}}$, ft/sec

V_2 - Local velocity, $\sqrt{\frac{P - p}{1/2\rho}}$, ft/sec

x - Axial distance, ft

Y - Distance perpendicular to hull, ft

σ - Cavitation index, $\frac{p_o - p_v}{1/2\rho A V_o^2}$

ρ - Mass density of fluid, slugs/ft^3

I

SUMMARY AND CONCLUSIONS

This report describes the results of tests of a 1/28 scale model, designed and built by General Dynamics/Electric Boat Division, of A Novel Electric Power Propulsion System (NEPPS) and prediction of prototype performance. All testing was performed at the wind tunnel and water tunnel facilities of the Ordnance Research Laboratory at Pennsylvania State University. Numerical test data reported is taken from the test report, Reference 3, submitted by the Ordnance Research Laboratory.

Analysis of the test results leads to the following conclusions:

1) Comparison of model cavitation data indicates that the cavitation performance of the NEPPS propeller is better than that of the conventional propeller. The superior propulsor cavitation performance indicates that the NEPPS prototype will have a better overall acoustic quality than a conventional propeller-driven submarine. The critical cavitation index of the NEPPS model was 4.5.

2) Torque measurements over a wide range of operating conditions indicate that propeller torque does not exceed the values originally assumed in the design of the electrical machinery. Consequently, the electrical machinery as proposed will not be overloaded in any maneuver.

3) Tests made at zero advance speed both for forward and reverse propulsor rotation indicates very good reverse thrust characteristics, the reverse thrust being 78% of the forward thrust.

When a relatively large model is tested in a tunnel, small pressure perturbations may occur, which would not exist in unrestrained flow. Axial force on the body caused by these pressure perturbations may be

large compared with the skin friction, the skin friction being the major component of resistance. Consequently, the accuracy of the prediction of ship's speed and the evaluation of the matching of propeller to the hull is open to question. The following conclusions are very much subject to the above limitations.

4) The propulsive efficiency, based on the power at the blades of the model, is 90%. This efficiency is 3% less than predicted; however, this reduction in propulsive efficiency results in a change in speed of less than half a knot.

5) Self-propulsion was achieved at an advance ratio of 1.134 compared with the design value of 1.487, indicating that the propellers are underpitched.

6) The NEPPS prototype submarine will attain a speed of approximately 24 knots. This speed is approximately 1.3 knots less than was predicted and 2 knots less than an equivalent submarine propelled with a conventional propeller.

II

DESCRIPTION OF MODEL

The NEPPS hydrodynamic model (Figure 1) is a 1/28 scale model of a hypothetical full-size prototype. Hull offsets of the model are listed in Table I. The cast aluminum hull is 10 ft, 8.5 in. in length and has a maximum diameter of 14.75 in. To simplify the casting, machining, and assembly procedure, the hull was divided into four sections and bolted together. The castings were impregnated with a plastic resin for protection against water leakage and also to improve the surface finish. Bolt-on covers in two of the sections provide access to the internal propulsion machinery and test instrumentation. The stern control surfaces and sail assembly are made from mahogany and protected with a waterproof finish. The model is so constructed that all of the appendages are detachable. Sail and fairwater planes are scaled from their counterparts on the Thresher class submarine. The stern control surfaces have geometry similar to those on the Thresher class vessels; however, the surface areas were selected to approximate the required stabilizing moment by a similarity principle based on slender body theory. The body characteristics for the model and prototype are tabulated in Table II.

The propulsor is a set of counter-rotating propeller blades running on a ring-like hub forward of the control surfaces. The blades, precision-milled from stainless steel and hand-finished, are rigidly pinned to aluminum rotors. The forward rotor has nine blades, the aft rotor seven. A summary of propeller geometry for the model and the prototype is tabulated in Table III. Particular details of both rotors appear in Figures 2 & 3. Figures 4 & 5 are assembly drawings of each rotor. The rotors can be easily interchanged with a set of bladeless counterparts to accommodate test program requirements. The rotors as they are mounted on the model appear in Figure 6. Appendix III is an outline of the method used in the design of the propellers.

Both rotors are driven by a 20-horsepower synchronous motor through a series of shafts, gears, and chains within the hull (Figure 7). The rotors are directly attached to two hollow concentric counter-rotating stainless steel shafts. A third hollow shaft, concentric with the propeller shafts but non-rotating, supports the tail section and provides a passageway for oil to lubricate the propeller hub needle bearings.

Each rotating shaft is independently free to slide longitudinally through its support bearings. The axial movement is restricted by a strain-gaged thrust cell assembly for purposes of measuring propeller thrust. Strain gages are also bonded directly to the shafts for torque measurement. Brush and slip ring assemblies constitute the electrical connection between the rotating components and the bridge circuit.

The counter-rotating feature is effected using an idler shaft which is driven by the main drive shaft through a set of helical gears. By using silent chains and sprockets, the main drive shaft powers one propeller shaft while the idler shaft powers the other. Both propeller shafts rotate at the same speed but in opposite directions. In order to cover the required range of propeller speeds, the main drive shaft is also coupled to the motor by a silent chain drive. A shaft to motor speed ratio of either 1:1 or 1:2 may thus be obtained by simply changing a sprocket and chain.

The entire model is supported by two, hollowed out, stainless steel cubes, which are fastened to the rigidly fixed support strut. The cubes are capable of slight flexure in the fore and aft direction, proportional to the amount of axial force experienced by the hull. They are strain-gaged to measure this force. Between the cubes are two bellows assemblies through which the instrumentation leads and motor-cooling water run. The highly flexible bellows provide a waterproof passage from support strut to model interior without introducing appreciable error in the hull drag measurements. The general arrangement of the model appears in Figure 8.

III

FACILITIES AND RESULTS

3.1 Test Facilities

All testing was conducted at the Ordnance Research Laboratory at Pennsylvania State University. Two test facilities were utilized to accomplish the complete testing program; the four-foot, closed-return, subsonic wind tunnel, and the 48-inch diameter water tunnel. Both these facilities are described in Reference 1. Power, thrust, and cavitation tests of the fully appended model were conducted in the water tunnel. All other testing was done in the wind tunnel.

Since the model is large relative to the test facilities, tunnel wall interference would be excessive. In an effort to extend the capabilities of their facilities the Ordnance Research Laboratory has developed a technique which, in principle, eliminates wall interference effects. A tunnel liner is constructed such that its inner surface corresponds to streamlines which would exist if the model were moving through a fluid of effectively infinite extent. The resulting flow about the model simulates conditions in an extensive atmosphere. The design of such a liner requires a theoretical solution for the streamlines around the hull. The design is based on a technique employing a distribution of sources on the axis of the model. A complete description of the liner technique used is given in Reference 2. A liner constructed according to the foregoing method was installed in the water tunnel and also in the wind tunnel.

3.2 Test Results

3.2.1 Hull Pressure Measurements

The model was provided with pressure taps to measure the static pressure distribution on the surface of the hull. Boundary layer velocity profiles were measured with total pressure probes at several locations on the hull. The locations of the various static pressure taps and total pressure rakes are indicated in Figure 9 and described in Reference 3, which contains the test data.

Measurements of static pressure on the model hull were made in the wind tunnel at model speeds corresponding to advance ratios of 1.355, 1.226, 1.112, and 1.054 for the condition of the model with and without appendages.

Figure 10 compares the measured pressure distribution of the bare body, excluding propulsor blades, to the theoretical pressure distribution as obtained from Reference 4. The method of computation for the theoretical pressure distribution was adapted from Reference 5. These computations are made on the basis of a distribution of sources, with source strengths adjusted so that the normal component of velocity at the surface is zero at a large number of selected points.

The pressure distribution curves shown in Figure 10 show that the measured pressures compare closely with the theoretical pressures calculated from potential flow theory along the forward portion of the body but diverge aft of $x/L = 0.75$. This is to be expected since the boundary layer thickens toward the tail of the body and the actual pressure should be less than the theoretical value.

Figure 11 graphically illustrates the effect of adding appendages and propulsor on the measured pressure distribution. By comparing the curves of normal pressure with the physical shape of the model one can clearly see the effect that adding appendages and propulsor have upon the normal pressure distribution.

Since there is good correlation between the measured and theoretical static pressure distribution on the bare body, it may be concluded that the tunnel liner in the wind tunnel is eliminating tunnel-wall interference effects in a satisfactory manner for this configuration. However, the addition of the appendages and the working propulsor imposes a greatly different pressure distribution along the aft part of the body, which, in turn, should in principle be simulated with a change in the tunnel liner. Whether or not the effect of this change in the pressure distribution along the aft part of the body greatly affects the test results is not known; however, it is felt the tunnel liner technique should be reviewed if future testing is considered.

3.2.2 Boundary Layer Simulation:

In order to provide accurate predictions in expansion of model data to full scale, the model must operate in a flow field similar to that in which the prototype would operate. If the tunnel liner successfully eliminates all wall interference, the resulting flow about the model simulates conditions in an extensive atmosphere. The pressure distribution about the model will then be similar to that about the full scale ship. However, under a similar pressure distribution, a turbulent boundary layer always grows relatively faster at a lower Reynolds Number. Also transition occurs very nearly at the nose on a full size submarine. Consequently, in order to attain the same momentum thickness at or near the stern in a model test at a lower Reynolds Number, it is necessary to take advantage of the slower growth of a laminar boundary layer over the forward portion of the model. Transition may be fixed by stimulating turbulence at some station along the length of the body such that the turbulent boundary layer along the remaining length attains no more than the desired momentum thickness at the stern.

The growth of the boundary layer along the hull was theoretically determined by an electronic digital computation based on Truckenbrodt's analysis (Refernce 6) and utilizing the computed pressure distribution (Reference 7).

Using the above analysis, it was determined that if the momentum thickness at a plane forward of the propulsor on the model is to be proportioned to the momentum thickness at the same plane of the prototype, transition of the boundary layer would have to be fixed at $x/L = 0.295$ for the water tunnel tests and at $x/L = 0.475$ for the wind tunnel tests. Unfortunately, the Reynolds Number of the tests is high enough to cause natural transition to occur well ahead of these locations. Even at $x/L = 0.09$, approximately the minimum pressure point, the Reynolds Number based on length of model is 2.8×10^6 in the water tunnel and 5.8×10^5 in the wind tunnel. Therefore, the boundary layer momentum thickness near the aft end of the model necessarily exceeds that of the prototype scaled to model size. However, to insure

symmetry about the model and a constant location of the transition, the boundary layer was stimulated at x/L = 0.04 in both the wind tunnel and the water tunnel tests. The stimulator in both cases was a 1/16"-diameter trip wire.

That the boundary layer on the model is, in fact, a fair approximation of the scaled prototype boundary layer is exemplified in Figure 12, a comparison of the measured boundary layer velocity profile to the calculated velocity profile at an axial location between the rotor hubs. Measurements were made with bare hubs and with trip wire installed. At x/L = 0.8773 the scaled thickness of the calculated boundary layer on the prototype is 1.839" and the measured thickness on the model is 1.955". The equation for the calculated velocity profile is

$$\frac{V}{V_o} = \left(\frac{Y}{\delta}\right)^{1/5}.$$

Other boundary layer velocity profiles of interest were measured at locations before the propulsor, between the rotors, and after the propulsor while the propulsor was operating. Figures 13, 14, and 15 are representative profiles at these locations.

3.2.3 Flow Angularity

Swirl angles were measured forward, between, and aft of the counter-rotating propellers over a range of advance ratios. The effect of advance ratio on the magnitude of the swirl angle was found to be small. Figure 16 is representative of a yaw probe traverse at these locations. From these curves we may ascertain the effectiveness of the aft rotor in the cancellation of the whirl component of velocity. Further information on whirl cancellation may be inferred from the reactive torque of the stern control surfaces. Figure 17 is a plot of the fin (stern control surface) torque coefficient versus advance ratio. At self propulsion the fin torque is approximately 8% of the propulsor torque. This indicates that only a small amount of rotational energy is lost in the slip stream; however, this small torque unbalance must be compensated with a roll moment to obtain trim.

There is additional evidence of effective cancellation of whirl components in the good tail cone cavitation performance.

3.2.4 Drag, Torque and Thrust

Drag

Drag of the bare body, defined as the total axial force on the model, was evaluated from the wake surveys by the well known method of B. M. Jones, described in References 8 and 9. The drag coefficient by this method, assuming axial symmetry, is:

$$C_D = \frac{4\pi}{A} \int_0^\infty \frac{V_2}{V_o} \left(1 - \frac{V_1}{V_o}\right) r \, dr$$

where:

V_1 = Total velocity = $\sqrt{\frac{P-p_o}{1/2\rho}}$

V_2 = Local velocity = $\sqrt{\frac{P-p}{1/2\rho}}$

p_o = free stream static pressure

P = local total pressure

p = local static pressure

r = distance from the axis

Since beyond a certain radius (r) the integrand disappears, the infinite upper limit presents no difficulty. For low-resistance slender-bodies of revolution this method is especially suitable, since axial pressure gradients and support interference in a wind tunnel make reliable direct force measurements relatively difficult. The bare body drag coefficient obtained in the wind tunnel by this method was found to be 0.1036.

It is not practical to determine the added drag of appendages by the above method. Therefore appendage drag was obtained in the water tunnel from measurements with force transducers in the model support

beam. The force cubes measure the net axial force on the model; therefore, the added drag of the appendages on the unpowered model could be obtained. The total drag coefficient was obtained by adding the individual contribution of drag of the various appendages, as measured in the water tunnel, to the bare body drag coefficient obtained in the wind tunnel. The total drag is not measured by direct force measurements in the water tunnel because in a closed test section the total axial force would be subject to large errors due to very minor changes in the pressure upstream and downstream. The use of the wake momentum method to obtain the basic bare body drag obviates this difficulty. The results obtained are tabulated below:

Configuration	ΔC_d	C_d
Bare Body	-	0.1036
Sail	0.0072	0.1108
Stern Control Surfaces	0.0119	0.1155
Sail and Control Surfaces	0.0195	0.1231

Self-propulsion of the model occurs when the net axial force on the model is zero. This operational mode is obtained when the net thrust of the propulsor equals the net drag of the model. From the wake surveys of the unappended model in the wind tunnel, self-propulsion occurs at an advance ratio of 1.171. For the appended model, the self-propulsion point was obtained from axial force measurements made in the water tunnel. The results are listed below

Configuration	Advance Ratio
Unappended Model	1.175
Model with Sail	1.156
Model with Stern Control Surfaces	1.150
Fully appended Model	1.134

The design advance ratio was 1.487 compared to the self-propulsion advance ratio of 1.134. However, this lack of agreement between the design and self-propulsion advance ratio does not indicate a slower speed for the vessel, but does indicate that the propellers are under pitched.

Figure 18 shows the variation of axial force as a function of advance ratio for various appended configurations. Figures 19 and 20 are representative of wake surveys made for the bare body, powered and unpowered.

Self-propulsion is directly dependent upon drag, hence it is subject to all of the same experimental errors including the large effects of small pressure perturbations in the tunnel. It is also directly affected by the accuracy of the simulation of the infinite flow field by the tunnel liner. The degree of accuracy of the drag tests is not known, but it is felt that the results may be slightly high and therefore the advance ratio at self-propulsion may be higher than indicated.

Torque

Figure 21 shows the variation of the torque coefficient for the fully appended model over a range of advance ratio from 1.0 to 1.6. The torque coefficient as presented in this curve represents the torque delivered to the blades only. The blade torque was separated from the total torque by subtracting the hydraulic torque of the bare hubs from the total torque. The hydraulic torque of the bare hubs was determined from test runs made with the fully appended model equipped with bare hubs. In all of the subsequent torque tests, zero torque was determined with bare shafts only. The results of these tests indicate that for the fully appended model the torque coefficients for the forward and aft rotors at self-propulsion are $C_{Qfwd} = 0.0121$ and $C_{Qaft} = 0.0130$.

Admittedly, the addition of blades to the hubs changes the relative velocity past the hubs; therefore, the torque of the hubs may be increased during tests made with the blades compared to tests made with bare hubs only. However, it is felt that this effect is small and in any event the values as quoted are conservative in this respect.

In addition to the small range of advance ratio's bracketing the self-propulsion point, torque tests were made covering a large range of advance ratios for both normal and reverse rotation of the rotors through the full operational range of the model. The results of these tests appear in Figure 22. To obtain torque values at an infinite advance ratio, tests were made with the rotor shafts locked at the motors. The result of these tests appear in Figure 23. In addition to the above tests, torque and axial force tests were conducted on the model with zero tunnel speed and varying rotor speed. Figure 24 represents the results of the torque tests and Figure 25 the axial force (Thrust) tests for zero tunnel speed. These tests covering a wide range of operational modes are required to predict the performance of the propulsion machinery during transient conditions.

Thrust

The effect of the unknown local static pressure acting on the front and back face of each hub produces a large unknown contribution to the thrust of each unit. Consequently, no meaningful thrust data is available for the separate units. Therefore, individual propeller thrust and efficiency can not be determined. Effective total thrust is known from the axial force transducer measurements.

3.2.5 Effective Horsepower and Propulsive Efficiency

The propulsive coefficient of the vessel, defined as the ratio of the tow line horsepower of the fully appended, unpowered model to the shaft horsepower delivered to the blades at self-propulsion, can be determined from the existing test data.

$$e_p = \frac{EHP}{SHP} = \frac{DV}{2\pi nQ} = \frac{C_d V}{2\pi C_Q D_m n}$$

$$= \frac{C_d}{C_Q} \frac{J}{2\pi}$$

$$= \left(\frac{.1231}{.0251}\right)\left(\frac{1.134}{6.28}\right)$$

$$\approx .90$$

From Reference 10 the horsepower available at the blades is 11,560 HP; therefore, the EHP at self-propulsion is approximately 10,400 HP.

3.2.6 Cavitation

Cavitation index measurements were obtained separately from the thrust and power measurements. The procedure was to fix the propeller advance ratio and to vary the test section pressure. Tunnel static pressure was then reduced until profuse cavitation occurred on the propeller blades. This was confirmed by visual observations. The static pressure was then gradually increased and the value of the static pressure noted when the cavitation in a particular region under observation had ceased. The propeller RPM was then changed and the pressure varied once again. This procedure was performed over a range of propeller RPM's for different test section velocities. For each condition the advance ratio was calculated and the test section pressure and velocity at the inception of cavitation recorded. The results of these tests are reported in the form of critical cavitation index defined by

$$\sigma_c = \frac{p_o - p_v}{1/2 \rho A V_o^2} ,$$

where p_v equals the liquid vapor pressure. Cavitation indices were established for the inception of cavitation at the blade leading edge suction face, suction face, pressure face, tip vortex and tail cone.

The results of the cavitation tests appear in Figure 26 for the forward rotor and Figure 27 for the aft rotor. The data as presented represents the average value of cavitation index for each type of cavitation between the "best" blade and the "poorest" blade. At self-propulsion as tunnel pressure is reduced, the sequence of cavitation occurring for both rotors is: the leading edge suction face, blade tip, suction face, and tail cone. The tail cone cavitation occurred only at the lowest attainable tunnel pressure and appeared to be very weak. This indicates effective cancellation of whirl components by the two propellers. Since tail cone cavitation could only be obtained at relatively high, advanced ratios and very low

tunnel pressures, a sufficient number of cavitation indices for presentation could not be obtained. Leading edge pressure face cavitation occurred on the blades of the forward rotor at advance ratios above 1.4; however, none of this type cavitation developed on the aft rotor blades. An example of profuse suction face cavitation appears in Figure 28. Blade tip vortex cavitation is evident in Figure 29.

The critical cavitation index at self propulsion for the forward rotor is 4.5, and for the aft rotor is 4.0; therefore, cavitation-free performance is limited by the forward rotor. From Figures 26 and 27 it is seen that the cavitation performance of both rotors becomes more favorable with increasing values of advance ratio. The minimum cavitation index occurs at an advance ratio of 1.45; this is approximately at the design advance ratio, and is to be expected since the velocity relations are most favorable at this point.

Cavitation was also observed on both the sail and the tail appendages. All parts of the appendages could not be observed. However, a cavitation index of 1.10 was determined for the port fairwater plane and 1.155 for the upper stern control surface on the port side. Although the occurrence of cavitation on the appendages does not affect the performance of the propulsor, it does add to the noise level of the vessel.

IV

PREDICTED SHIP PERFORMANCE

4.1 Speed and Drag

In predicting the speed and drag of the full scale prototype from model test data, it is assumed that the total coefficient of resistance of the model is the sum of two components, one of which is subject to variation with Reynolds Number (coefficient of frictional resistance), and another which is not (residual resistance). For the prototype, the total resistance is the sum of three components, two of which are subject to the same variations as the model and a third which is an added roughness allowance. That component which is not a frictional coefficient is independent of Reynolds Number. Therefore, the coefficient of residual resistance for the model is equal to that of the prototype. For the NEPPS prototype the skin friction is of two parts, the first part is the coefficient due to the frictional resistance of the model due to the ship's speed, and the second part is the increment of frictional resistance due to the propeller slipstream. The ratio of the increased drag due to the slipstream to the frictional drag of the ship due to ship speed only was estimated to be 0.179. Therefore, the total coefficient of frictional resistance is

$$C_f = C_{f_o} + C_{f_s} = 1.179\ C_{f_o}$$

where C_{f_o} is the Schoenherr coefficient, C_{f_s} is the incremental coefficient due to the slipstram, and C_f is the total coefficient of frictional resistance.

The performance is corrected for the change in Reynolds Number from model to prototype on the assumptions that: (1) frictional resistance varies with Reynolds Number according to the Schoenherr line, and (2) there is no gain in propulsive efficiency resulting from the reduction in thrust coefficient which accompanies the reduced

resistance at higher Reynolds Number. Assumption (2) is conservative since some favorable effect would be expected.

This method of scaling the coefficient of resistance from model to full scale is graphically illustrated below:

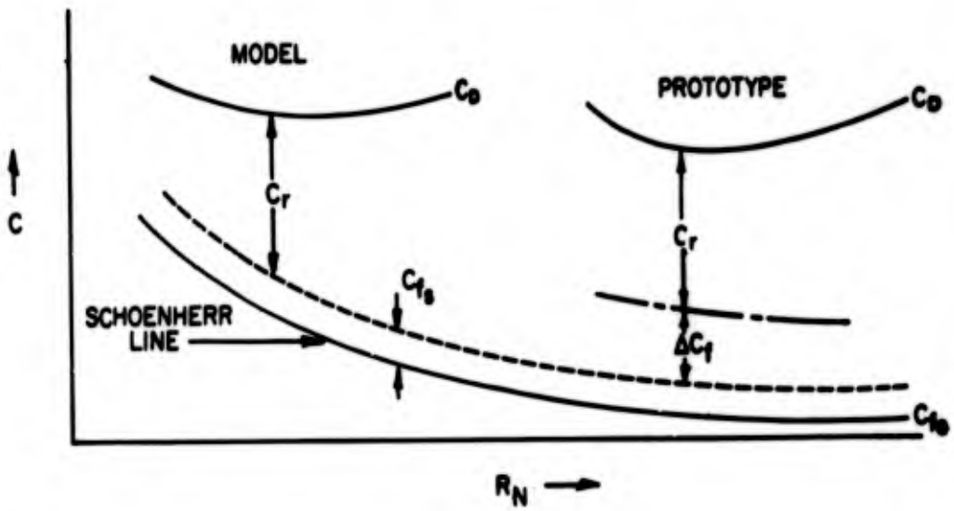

where:

C	= Coefficient of resistance
C_r	= Coefficient of residual resistance
C_f	= Coefficient of frictional resistance
C_{f_o}	= Coefficient of frictional resistance (due to ship speed)
C_{f_s}	= Coefficient of frictional resistance (due to slipstream)
ΔC_f	= Added coefficient of roughness (0.0004)
C_D	= Total coefficient of resistance

The total coefficient of resistance for the model was determined from powered tests of the model. Values of C_{f_o} (Schoenherr's friction factor) were obtained from Reference 11. Schoenherr's friction factors are non-dimensional coefficients based on the wetted surface area.

The total wetted area of the full size prototype is 29,792 ft^2. From the model test results, the following coefficients evolve

	Model (in fresh H_2O)	Prototype (in salt H_2O)
R_N	3.083×10^7	9.2×10^9
C_{f_s}	0.00044	0.00027
C_{f_o}	0.00246	0.00155
C_f	0.00290	0.00182
C_r	0.00085	0.00085
ΔC_f	0.0	0.0004
C_D	0.00385	0.00307
C_d	0.1231	0.0980

C_d is the total coefficient of resistance based on the maximum cross-sectional area of the ship.

The total resistance of the prototype can be determined from the friction coefficient and expressed as

$$R = C_D \, 1/2 \, \rho V^2 S_w.$$

The EHP can be expressed in terms of the total resistance,

$$EHP = \frac{RV}{550}.$$

Combining the above equations results in an expression for the velocity,

$$V = \left(\frac{550 \times EHP}{C_D \, \rho/2 \, S_w} \right)^{1/3}.$$

With the values of C_D and EHP from the model tests, the computed speed at full power is

$$V = \left(\frac{550 \times EHP}{C_D \, \rho/2 \, S_w}\right)^{1/3} \frac{1}{1.689} = \left(\frac{114.7 EHP}{C_D S_w}\right)^{1/3}$$

$$= \left(\frac{114.7 \times 10{,}404}{.00307 \times 29{,}792}\right)^{1/3} \approx 23.60 \text{ knots}$$

The predicted speed from test data of 23.6 kts. differed from the estimated speed of 25.3 kts. This difference in speed is the result of a larger drag coefficient and a slightly lower propulsion coefficient than was estimated. The attained propulsion coefficient was 0.90 compared to the estimated coefficient of 0.93.

Figure 30 represents the full speed range performance curve of the prototype ship. The horsepower in this figure represents that power which is available to the blades of the propeller.

4.2 Cavitation Performance

The test results indicate that the critical cavitation index at self propulsion is $\sigma_c = 4.5$. From the expression for cavitation index, the minimum cavitation-free depth at which the NEPPS submarine can operate at full power can be obtained:

$$\sigma_c = \frac{p_o - p_v}{\rho/2 \, V_o^2} = \frac{h' + 32}{V_o^2/2g}$$

$$h' = \frac{\sigma_c V^2}{2g} - 32 \, .$$

Where h' is the depth in feet to the uppermost blade. The distance to the ship's centerline is; therefore,

$$h = h' + \frac{D_f}{2} \qquad \text{where } D_f = \text{Hub Diameter of forward rotor}$$

$$h = \frac{\sigma_c V^2}{2g} - 32 + \frac{D_f}{2}$$

$$h = \frac{(4.5)(23.6 \times 1.689)^2}{2 \times 32.2} - 32 + 11.635$$

$$h = 92 \text{ ft.}$$

The calculated cavitation-free depth from design parameters was 23 ft, which is considerably less than that obtained from the test data. However, examination of the cavitation test data will shown that at the design advance ratio the critical cavitation index corresponds to a depth approximately equal to what was predicted.

Although accurate prediction of full scale cavitation performance from model tests is admittedly difficult, a comparison of the tabulated critical depths of the NEPPS model to those of the Skipjack model (SS(N)585) indicates a distinct advantage for NEPPS over the conventional propeller. Figure 31 is a comparison of the cavitation-free depth versus speed between the NEPPS model, the Skipjack model, and the Skipjack prototype. The Skipjack model data was obtained at the Ordnance Research Laboratory and the prototype data was obtained during the Skipjack acoustic sea trials. σ_c for the Skipjack model was 5.6.

Of particular interest in the cavitation results is the fact that the hub vortex, which is the critical cavitation for the Skipjack, is practically eliminated on the NEPPS model.

4.3 Starting and Backing Performance

Reference 10 discusses starting and backing down for two modes of operation of the machinery, and presents rough curves of maneuvering performance. Computation of these curves required, as one input, curves of propeller thrust and torque vs rpm with ship speed as a parameter. In the absence of better information, a set of curves was quite arbitrarily assumed.

Figure 32 shows both the assumed and the model test curves of the propeller torque versus rpm for 100% ship speed. Starting is a straightforward maneuver and no difficulty is expected.

With respect to backing down, the test curve, although only one of a set, does support some further observations since it is known that all curves for forward ship speeds less than 100% are above the one shown. It can thus be seen that the test torque is substantially less than the assumed torque and the machinery can more easily stop and reverse the propeller. This will lead to less heating in the machinery, which is of course desirable. However, since the propeller torque and thrust are approximately directly proportional, the thrust is smaller and the ship will not stop as quickly as predicted. However, the results of thrust and torque tests under static conditions with various rotor speeds, both normal and reverse rotation, indicate that after an initial Reynolds Number dependent effect, the thrust coefficient reduces to a nearly constant value. From these results it is seen that the reverse thrust is approximately 78% of the forward thrust, indicating very good backing down characteristics.

The two modes of backing down (astern stages and electrical switching), discussed in Reference 10, yield about the same stopping times based on the assumed curves. Ignoring for the moment the value of machinery simplicity for the astern stage mode, the test curve favors the switching mode, since reversing time with astern stages is determined primarily by the exceedingly large turbine generator inertia and does not benefit greatly from reduced propeller torque. Also the astern stages produce less torque at the high reverse rpm than the ahead stages do at the same absolute speed. However, a quantitative assessment of how large this difference is would require more extensive analysis.

V

RECOMMENDATIONS

It is considered that for the first design of such an unconventional propulsor as NEPPS, the test results are quite satisfactory. In view of the good propulsive efficiency and cavitation performance of this model, it is felt that sufficient promise has been demonstrated to warrant further development of the propeller. A redesign would aim to achieve self-propulsion at the design advance ratio and simultaneously to improve the cavitation performance. Further development of the hydrodynamic design would utilize the results of the present model tests and also incorporate some changes in the design technique. A new design would be adapted to the measured wake rather than an assumed one, and a somewhat different distribution of circulation on the blades would be used. In addition, the blade section lift coefficient would be decreased by increasing the blade area. Two effects would result from this, a slight decrease in propulsive efficiency and an improvement in the cavitation performance.

However, if a redesign is contemplated, the existing drag data and the value of the advance ratio at self-propulsion must be confirmed or more exact data obtained. A solution to this is to have drag tests of the model conducted in a towing tank at David Taylor Model Basin. Another approach would be to construct a wooden model of such a size that the wall interference in the tunnel facilities at ORL would be negligible. Reliable drag data would evolve from these small model tests, but no new information on self-propulsion would be obtained.

VI

REFERENCES

1. Lehman, August F., "The Garfield Thomas Water Tunnel," Ordnance Research Laboratory, Pennsylvania State University, NOrd 16597-56, Sept. 30, 1959.

2. Lehman, A. F.; Light, J. H.; Peirce, T. E.; "Elimination of Water Tunnel Interaction with a Coaxial Test Body by a Flow Correcting Liner and Application of the Technique to an Albacore Model," Ordnance Research Laboratory, Pennsylvania State University, NOrd 16597-39, July 25, 1958.

3. Casellini, L. M.; Hinger, A. C.; "Evaluation of Wind Tunnel and Water Tunnel Tests on a 1/28 Scale Model of a Submarine Prototype for a Novel Electric Power Propulsion System," Ordnance Research Laboratory, Pennsylvania State University, TM 19.2631-02, May 10, 1963.

4. Pakstys, M.; MacNeil, S.; McKenzie, A. S.; Dabrowski, N. J.; "Potential Flow Program for Bodies of Revolution," General Dynamics/Electric Boat U411-62-050, Oct. 19, 1962.

5. Smith, A. M. O.; Pierce, J.; "Exact Solution of the Neumann Problem: Calculation of Non-Circulatory Plane and Axially Symmetric Flows About or within Arbitrary Boundaries," Douglas Aircraft Co., El Segundo, California, ES-26988, April 25, 1958.

6. Truckenbrodt, E.; "A Method of Quadrature for Calculation of the Laminar and Turbulent Boundary Layer in Case of Plane and Rotationally Symmetrical Flow," NACA-TM 1379, May, 1955.

7. Dabrowski, N. J.; McManus, D. S.; Dollar, G. A.; "Procedures for Boundary Layer Calculations According to Truckenbrodt's Analysis," General Dynamics/Electric Boat, U411-62-034, Aug., 1962.

8. Schlichting, H., "Boundary Layer Theory," 4th Edition, McGraw-Hill, New York, 1960.

9. Jones, B. M., "The Measurement of Profile Drag by the Pitot Traverse Method," Aeronautical Research Council (British) R&M 1688, 1936.

10. Ryskiewich, B. S., "Feasibility of a Novel Electric Power Propulsion System (NEPPS) for a Submarine; Vol. I of III - Engineering Study," General Dynamics/Electric Boat, C411-62-024, March 30, 1962.

11. Gertler, M., "A Reanalysis of the Original Test Data for the Taylor Standard Series," DTMB 806, March, 1954.

FIG. 1 NEPPS HYDRODYNAMIC MODEL

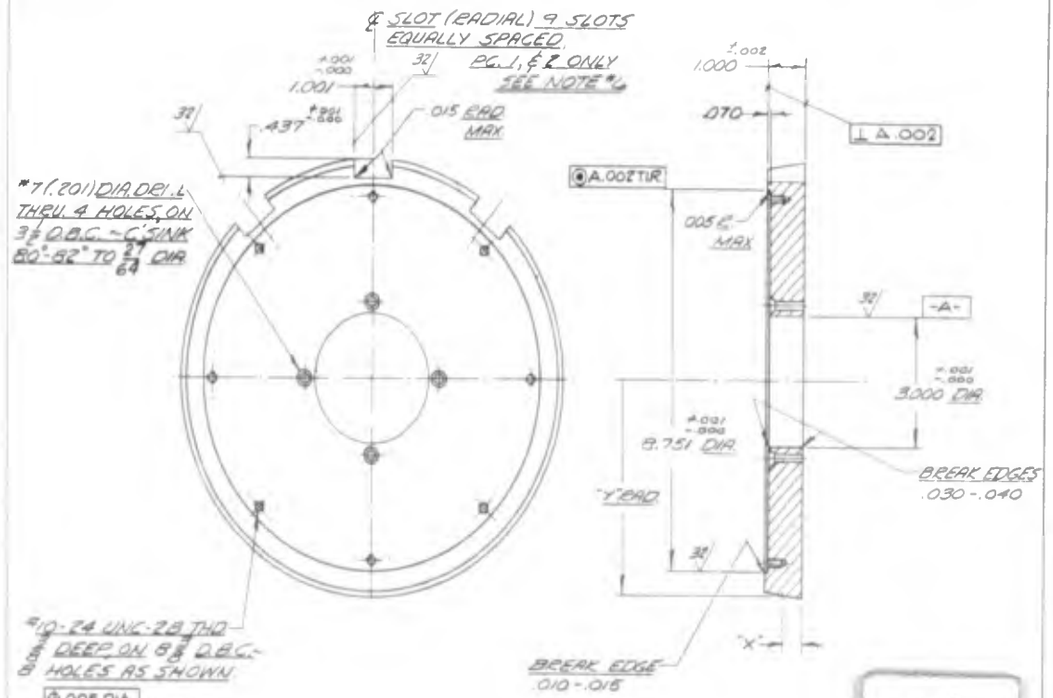

1 2 3 HUB, ROTOR

TABLE OF COORDINATES PC #1, 2 & 3

"X"	"Y" RADIUS
.000	5.029
.500	4.963
1.000	4.898

SEE NOTE "1"

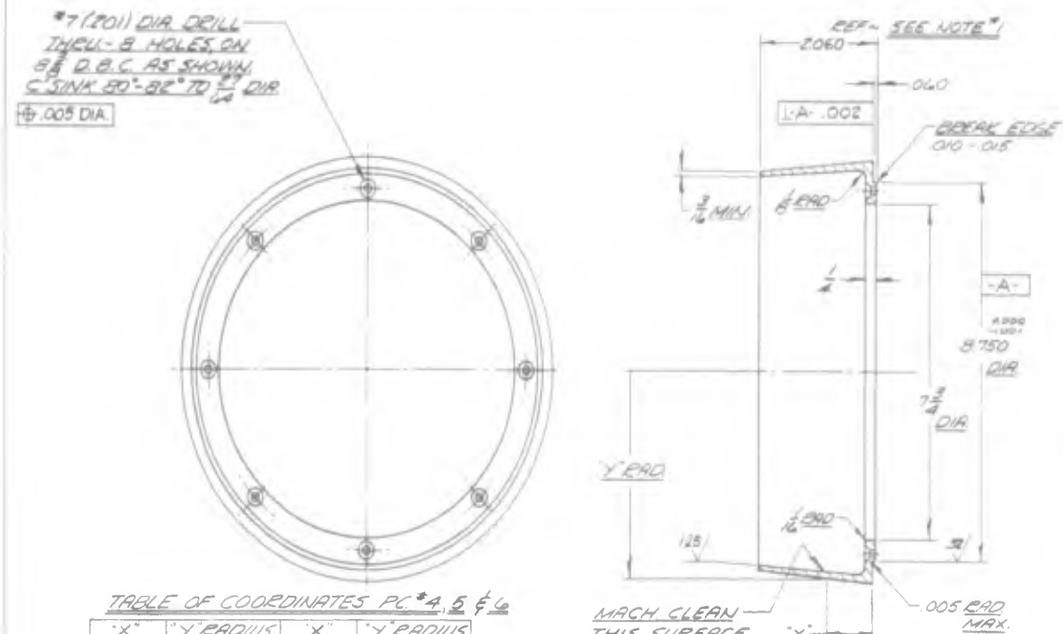

TABLE OF COORDINATES PC #4, 5 & 6

"X"	"Y" RADIUS	"X"	"Y" RADIUS
.000	4.898	1.500	4.679
.500	4.828	2.000	4.600
1.000	4.757	2.045	4.590

SEE NOTE "1"

4 5 6 EXTENSION, ROTOR

* PATT. No. 135007

PC. #

STA No.	REF. No.	R
1	1	4
4	2	5.
6	3	5.
8	4	5
9	5	5
10	6	6
2	-	5.
3	-	5.

A SEE NOTE #7

DIAGR
FOR LOCAT
SCALE

No.	TITLE
6	NEPAS BLADE PROFILE STA 10 ROTOR #1-R
5	STA 9
4	STA 8
3	STA 6
2	STA 4
1	NEPAS BLADE PROFILE STA 1 ROTOR #1-R

SYM	ENG ORDER	REVISIONS	DATE	BY	APP
A		ADDED NOTE #7 & STA #2 & #3 DELETED ITEMS #2 #5 AND #8 FROM L/M AND ALL REFERENCE TO THESE ITEMS	5-1962	REL	WTB

TABLE OF COORDINATES FOR ROTOR BLADE PROFILES ALL DIMENSIONS ARE LINEAR TOLERANCE ±.003

PC. No. 7

STA No.	REF No	RAD. AT STA.	LEADING EDGE X_1	LEADING EDGE Y_1	TRAILING EDGE X_2	TRAILING EDGE Y_2
1	1	4.985	.157	.410	.157	.410
4	2	5.155	.186	.353	.186	.353
6	3	5.375	.167	.304	.167	.304
8	4	5.668	.134	.242	.134	.242
9	5	5.838	.115	.208	.115	.208
10	6	6.023	.089	.172	.089	.172
SEE NOTE #7	2	-	5.020	.181	.392	.181	.392
	3	-	5.077	.188	.373	.188	.373

PC. No. 8

STA No.	REF No	RAD. AT STA	LEADING EDGE X_1	LEADING EDGE Y_1	TRAILING EDGE X_2	TRAILING EDGE Y_2
	7					
	8					
	9					
	10					
	11					
	12					

LOCATION OF LEADING EDGE AND TRAILING EDGE RADIUS

2

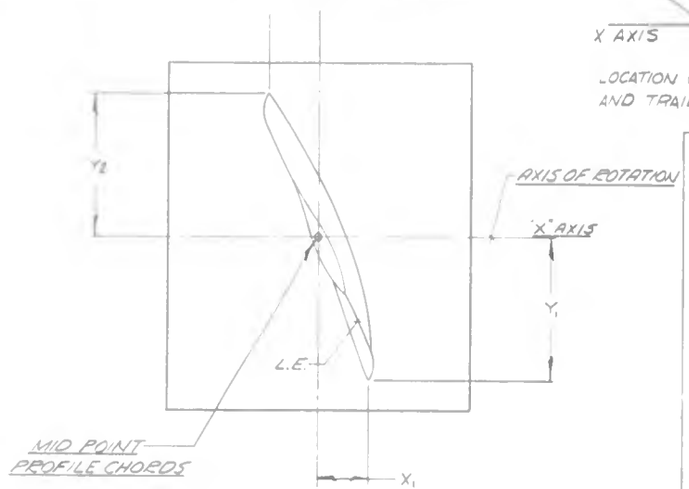

NOTES:

1. COORDINATES NOTED PCS. No. 1 THRU 6, TO BE USED FOR MACH ALLOWANCE ONLY, CONTOURS INDICATED, TO BE MACH. AT ASSY REF D-200318
2. ROTOR BLADE PROFILES TO BE MADE AS SHOWN FROM PROFILES OF RESPECTIVE STA (REF 1-6 FOR PC No. 7 - REF 7-12 FOR PC. No. 8) AND RELATED COORDINATE DATA BLADE TEMPLATES THEN TO BE LOCATED AS PER TABLE OF COORDINATES FOR PROFILES, TANGENT TO THIER RESPECTIVE STATION RADII.
3. REMOVE ALL BURRS & SHARP EDGES.
4. UNLESS OTHERWISE SPECIFIED, MACH. SURFACES TO BE 63 MICRO-IN. (MAX.)
5. PC # 3 TO BE IDENTICAL TO PC'S No. 1, & 2 EXCEPT FOR THE OMISSION OF SLOTS SHOWN.
6. FINISH FOR BLADES ITEMS 7 & 8 TO BE 16 MU IN. ALL OVER UNLESS OTHERWISE SPECIFIED
7. STATIONS #2 AND #3 ARE REFERENCE STATIONS TO BE USED FOR STACKING PURPOSES ONLY

DIAGRAM OF COORDINATES FOR LOCATION OF BLADE PROFILES SCALE ~ 4:1 (SEE TABLE)

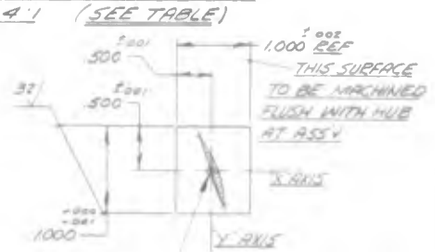

(7)(8) BLADE, ROTOR
SCALE ~ FULL SIZE

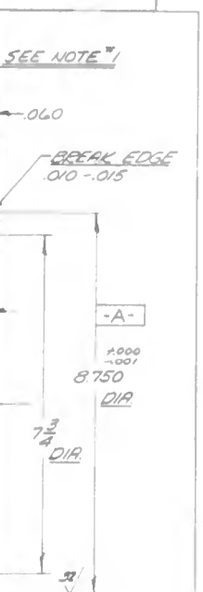

	N.E.P.P.S. BLADE PROFILE STA. ROTOR #1-A	D-200316 SHT.		N.E.P.P.S. BLADE PROFILE STA. ROTOR #1-B	D-200322 SHT.
6	STA 10	SHT. 6	12	STA	SHT. 6
5	STA 9	SHT. 5	11	STA	SHT. 5
4	STA 8	SHT. 4	10	STA	SHT. 4
3	STA 6	SHT. 3	9	STA	SHT. 3
2	STA 4	SHT. 2	8	STA	SHT. 2
1	N.E.P.P.S. BLADE PROFILE STA. ROTOR #1-A	D-200316 SHT. 1	7	N.E.P.P.S. BLADE PROFILE STA. ROTOR #1-B	D-200322 SHT. 1
No.	TITLE	DWG. No.	No.	TITLE	DWG. No.

REFERENCES

ITEM NO	REQD	PART NO	DESCRIPTION	MATL	MATL SPEC	UNIT WT
8	—	200319-8	BLADE, ROTOR #1-B	ST. STEEL	AISI 304	
7	—	200319-7	BLADE, ROTOR #1-A	ST. STEEL	AISI 304	
6	—	200319-6	EXTENSION, ROTOR #1-C	CAST ALUM.		
5	—	200319-5	EXTENSION, ROTOR #1-B	CAST ALUM.		
4	—	200319-4	EXTENSION, ROTOR #1-A	CAST ALUM.		
3	—	200319-3	HUB, ROTOR #1-C	ALUM		
2	—	200319-2	HUB, ROTOR #1-B	ALUM.		
1	—	200319-1	HUB, ROTOR #1-A	ALUM		

LIST OF MATERIAL

D-200318 — USED ASSY — USED ON

APPLICATION

UNLESS OTHERWISE SPECIFIED DIMENSIONS ARE IN INCHES TOLERANCES ON FRACTIONS ± 1/64 DECIMALS ± .005 ANGLES ± 1/2°

MATERIAL SEE L. M.

HEAT TREATMENT

FINAL PROTECTIVE FINISH

GENERAL DYNAMICS CORPORATION
ELECTRIC BOAT DIVISION, GROTON, CONN.
RESEARCH & DEVELOPMENT DEPARTMENT

	BY	DATE
DRAWN	W.E.	3/9/62
CHECKED	LACEY	3/9/62
EXAMINED	GP	3/9/62
APPROVED	WR	3/9/62

BLADE HALF SIDE # AS NOTED

DEVICE NO. N.E.P.P.S.
DWG TITLE ROTOR #1 DETAILS

DWG SIZE D — DWG NO 200319 — REV A — SHEET NO 1 OF 1

FIG. 2 ROTOR #1 DETAILS A-3

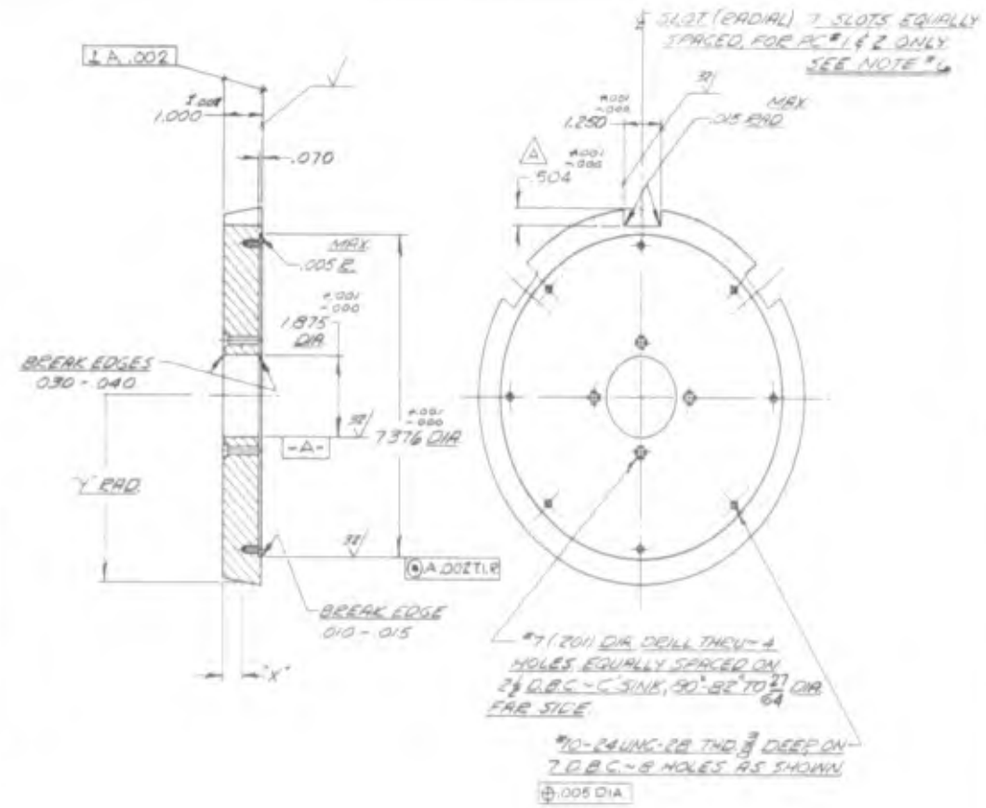

TABLE OF COORDINATES PC# 1, 3, & 2

"X"	"Y" RADIUS
.000	4.109
.500	4.185
1.000	4.281

SEE NOTE #1

(1)(2)(3) HUB, ROTOR

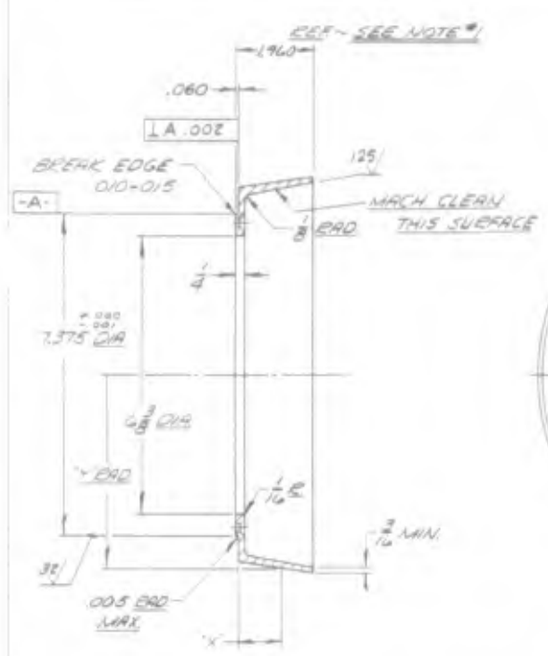

TABLE OF COORDINATES PC# 4 & 5

"X"	"Y" RADIUS
.000	4.281
.500	4.357
1.000	4.445
1.500	4.5[illegible]
1.930	4.590

SEE NOTE #3

(4)(5)(6) EXTENSION, ROTOR

PART # 135008

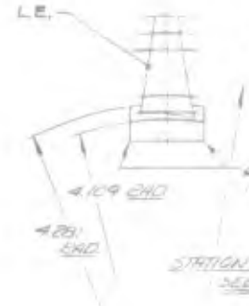

SYM	CHG ORDER	REVISIONS	DATE	BY	APP
A		ADDED NOTE #7 & STA #2 & #3 DELETED ITEMS #4, #5 AND #8 FROM L.M. & ALL REFERENCE TO THESE ITEMS-STA #6 Y, & Y2 WAS 361 504 DIM WAS 437-2 PLACES	3-19-62	PEL	R.T.B.

2

TABLE OF COORDINATES FOR ROTOR BLADE PROFILES ALL DIMENSIONS ARE LINEAR TOLERANCE ±.003

PC. No. 7

STA No.	REF. No.	RAD. AT STA.	LEADING EDGE X1	LEADING EDGE Y1	TRAILING EDGE X2	TRAILING EDGE Y2
1	1	4.182	.273	.495	.273	.495
4	2	4.368	.287	.424	.287	.424
6	3	4.605	.250	.361	.250	.367
8	4	4.916	.196	.296	.196	.296
9	5	5.096	.165	.255	.165	.255
10	6	5.290	.127	.214	.127	.214
SEE NOTE #7						
2	-	4.220	.296	.469	.296	.469
3	-	4.293	.296	.447	.296	.447

PC. No. 8

STA No.	REF. No.	RAD. AT STA.	LEADING EDGE X1	LEADING EDGE Y1	TRAILING EDGE X2	TRAILING EDGE Y2
	7					
	8					
	9					
	10					
	11					
	12					

LOCATION OF LEADING EDGE AND TRAILING EDGE RADIUS

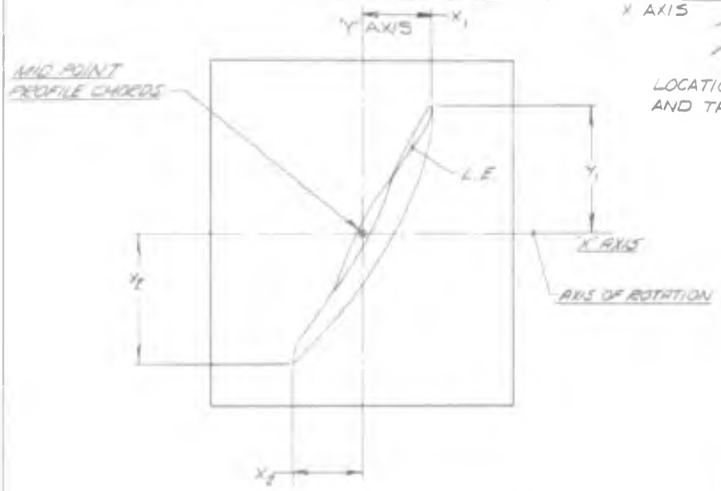

NOTES:

1. COORDINATES NOTED, PCS. No. 1, THRU 6, TO BE USED FOR MACH ALLOWANCE ONLY; CONTOURS INDICATED, TO BE MACH. AT ASSY REF D-200320
2. ROTOR BLADE PROFILES TO BE MADE AS SHOWN FROM PROFILES OF RESPECTIVE STA (REF 1-6 FOR PC No 7 ~ REF 7-12 FOR PC No 8) AND RELATED COORDINATE DATA BLADE TEMPLATES THEN TO BE LOCATED AS PER TABLE OF COORDINATES FOR PROFILES, TANGENT TO THEIR RESPECTIVE STATION RADII.
3. REMOVE ALL BURRS & SHARP EDGES
4. UNLESS OTHERWISE SPECIFIED, MACH. SURFACES TO BE 63 MICRO-IN. (MAX.)
5. PC #3 TO BE IDENTICAL TO PC'S No. 1, & 2, EXCEPT FOR THE OMISSION OF SLOTS SHOWN.
6. FINISH FOR BLADES ITEMS 7 & 8 TO BE 16 MU IN. ALL OVER UNLESS OTHERWISE SPECIFIED
7. STATIONS #2 AND #3 ARE REFERENCE STATIONS TO BE USED FOR STACKING PURPOSES ONLY

DIAGRAM OF COORDINATES FOR LOCATION OF BLADE PROFILES SCALE ~ 4/1 (SEE TABLE)

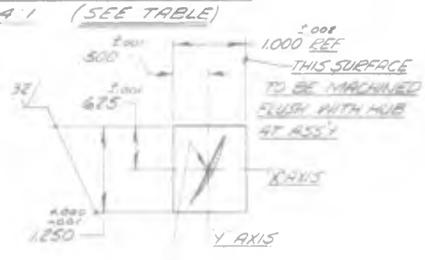

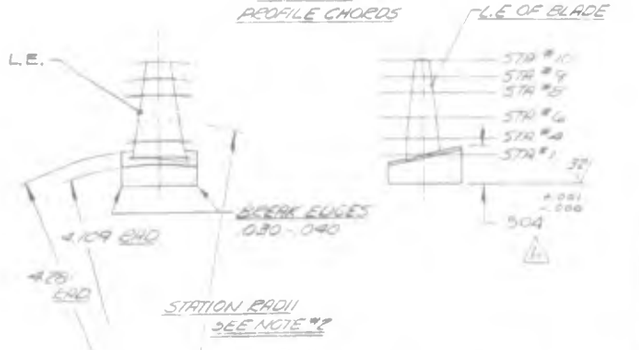

STATION RADII SEE NOTE #2

(7)(8) BLADE ROTOR SCALE ~ FULL SIZE

8	—	200321-9	BLADE, ROTOR #2-B	ST. STEEL	AISI 304	
7	—	200321-7	BLADE, ROTOR #2-A	ST. STEEL	AISI 304	
6	—	200321-6	EXTENSION, ROTOR #2-C	CAST ALUM.		
5	—	200321-5	EXTENSION, ROTOR #2-B	CAST ALUM.		
4	—	200321-4	EXTENSION, ROTOR #2-A	CAST ALUM.		
3	—	200321-3	HUB, ROTOR #2-C	ALUM.		
2	—	200321-2	HUB, ROTOR #2-B	ALUM.		
1	—	200321-1	HUB, ROTOR #2-A	ALUM		
ITEM NO	REQD	PART NO	DESCRIPTION	MATL	MATL SPEC	UNIT WT

D-200320 NEXT ASSY USED ON APPLICATION

LIST OF MATERIAL

GENERAL DYNAMICS CORPORATION ELECTRIC BOAT DIVISION GROTON, CONN. RESEARCH & DEVELOPMENT DEPARTMENT

SEE L.M.

N.E.P.P.S. ROTOR #2 DETAILS

SIZE D | CAGE NO. | DWG NO. 200321 | REV A | SHEET NO. 1 OF 1

REFERENCES

NO.	TITLE	DWG. NO.
1	NEPPS BLADE PROFILE STA #1 ROTOR #2-A	D-200323 SHT 1
2	NEPPS BLADE PROFILE STA #2 ROTOR #2-A	D-200323 SHT 2
3	NEPPS BLADE PROFILE STA #3 ROTOR #2-A	D-200323 SHT 3
4	NEPPS BLADE PROFILE STA #4 ROTOR #2-A	D-200323 SHT 4
5	NEPPS BLADE PROFILE STA #5 ROTOR #2-A	D-200323 SHT 5
6	NEPPS BLADE PROFILE STA #6 ROTOR #2-A	D-200323 SHT 6
7	NEPPS BLADE PROFILE STA #1 ROTOR #2-B	D-200324 SHT 1
8	NEPPS BLADE PROFILE STA #2 ROTOR #2-B	D-200324 SHT 2
9	NEPPS BLADE PROFILE STA #3 ROTOR #2-B	D-200324 SHT 3
10	NEPPS BLADE PROFILE STA #4 ROTOR #2-B	D-200324 SHT 4
11	NEPPS BLADE PROFILE STA #5 ROTOR #2-B	D-200324 SHT 5
12	NEPPS BLADE PROFILE STA #6 ROTOR #2-B	D-200324 SHT 6

FIG. 3 ROTOR #2 DETAILS A-5

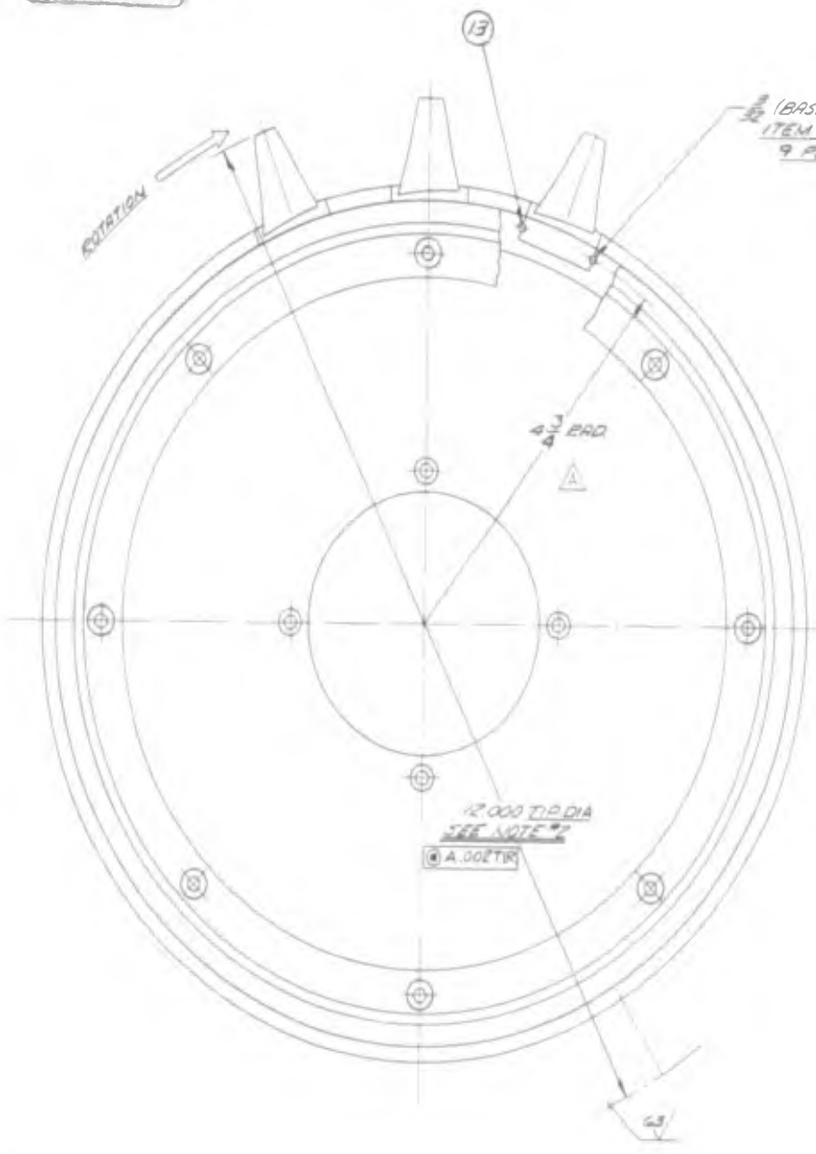

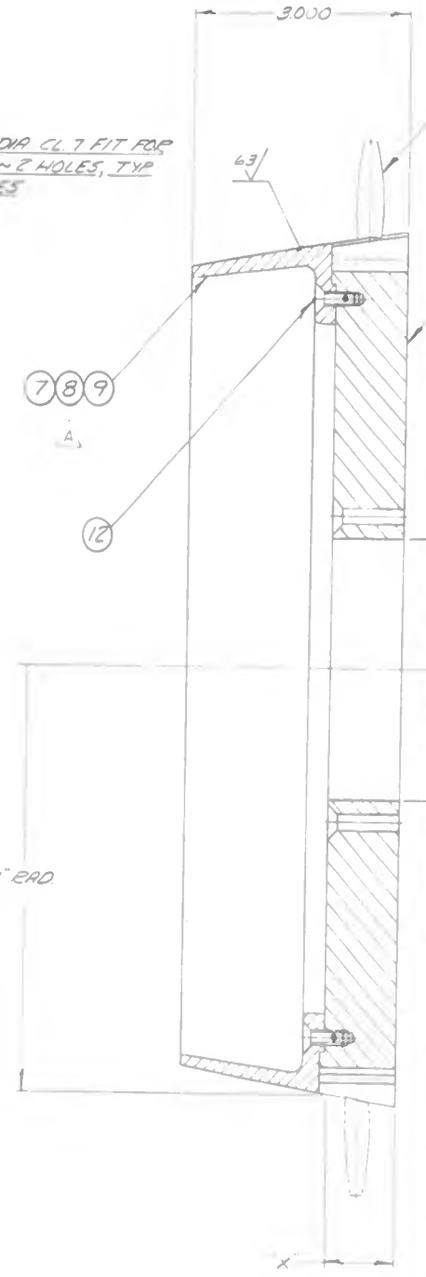

TABLE OF COORDINATES SEE NOTE #1

"X"	"Y" RADIUS
.000	5.029
.500	4.963
1.000	4.898
1.500	4.828
2.000	4.757
2.500	4.679
3.000	4.600
3.045	4.590

THIS COORDINATE FOR REF. ONLY

(1)(2)(3) ROTOR ASS'Y.

SYM	CHG ORDER	REVISIONS	DATE	BY	APP
A		4 3/4 RAD WAS 4 1/16 RAD DELETED ITEMS # 2, #5 #8 #11 AND ASSY # B FROM LIM & ALL REFERENCE TO THESE ITEMS - REV. NOTES #1 & #2	5-1-62	REL	A.L.

2

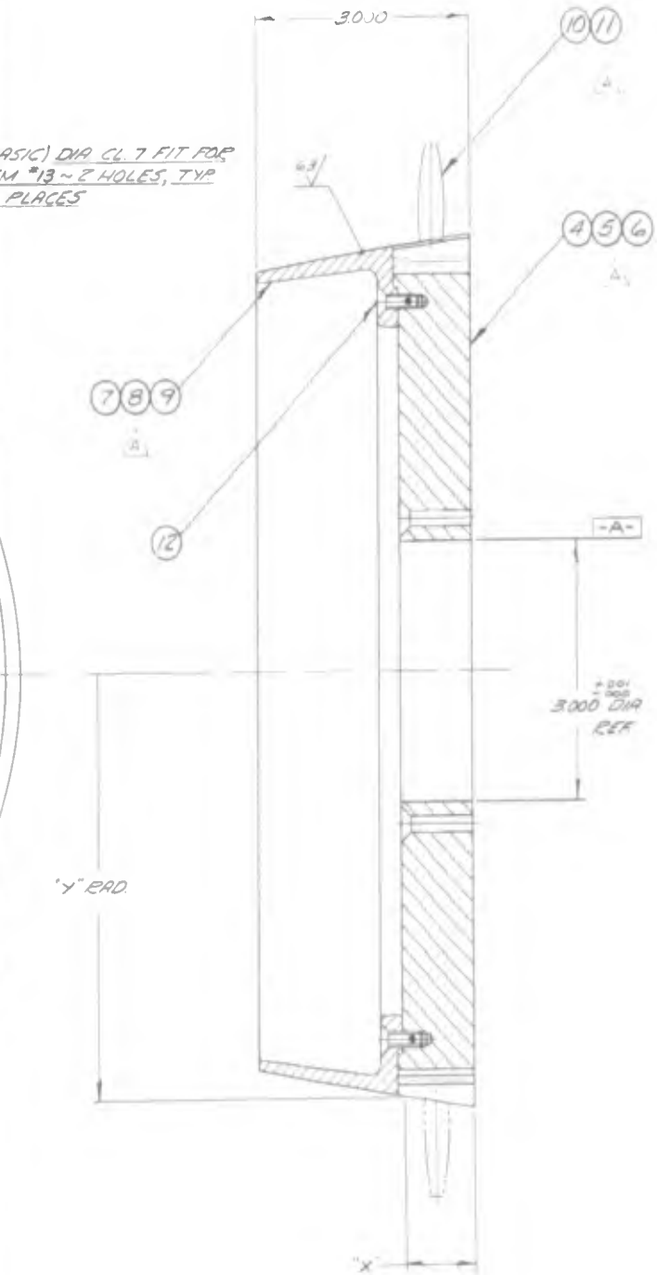

ASSY.

NOTES:

1. OUTSIDE CONTOUR OF ROTOR ASSY'S TO BE MACH. PER TABLE OF COORDINATES AFTER ASSY OF HUB, AND EXTENSION ~ WITH BLADES OMITTED FOR ITEMS #1 & 2.
2. TIP DIA NOTED TO BE MACHINED AFTER ASSY OF ROTOR ASSY'S. ~ ITEMS #1 & 2.
3. ALL ROTOR ASSY'S TO BE STATICALLY & DYNAMICALLY BALANCED TO WITHIN .003 IN. OZ.
4. BALANCING TO BE ACCOMPLISHED BY REMOVAL OF METAL ONLY.
5. AFTER ASSY OF ROTOR ASSY'S, ITEMS #1 & 2, BLADES TO BE MATCH MARKED, 1 – 9, WITH CORRESPONDING NO'S ON RESPECTIVE HUBS TO IDENTIFY THEIR PROPER LOCATION.
6. REMOVE ALL BURRS & SHARP EDGES.

ASSY A	ASSY B	ASSY C	ITEM NO	PART NO	DESCRIPTION	MATL	MATL SPEC	UNIT WT
QUANTITY					LIST OF MATERIAL			
18	18	—	13		PIN, DOWEL 3/32 DIA X 1"	ST. STEEL	COM'L	
8	8	8	12	NYLOK MS21044-B6	SCREW, HEX SOC. H.D. #10-24 X 1/2 LG.	ST. STEEL	COM'L	
—	9	—	11	200319-8	BLADE, ROTOR #1-B	ST. STEEL		
9	—	—	10	200319-7	BLADE, ROTOR #1-A	ST. STEEL		
—	—	1	9	200319-6	EXTENSION, ROTOR #1-C	ALUM.		
—	1	—	8	200319-5	EXTENSION, ROTOR #1-B	"		
1	—	—	7	200319-4	EXTENSION, ROTOR #1-A			
—	—	1	6	200319-3	HUB, ROTOR #1-C			
—	1	—	5	200319-2	HUB, ROTOR #1-B	"		
1	—	—	4	200319-1	HUB, ROTOR #1-A	ALUM		
—	—	1	3	200318-3	ROTOR ASSY #1-C			
—	1	—	2	200318-2	ROTOR ASSY. #1-B			
1	—	—	1	200318-1	ROTOR ASSY. #1-A			

GENERAL DYNAMICS CORPORATION
ELECTRIC BOAT DIVISION, GROTON, CONN
RESEARCH & DEVELOPMENT DEPARTMENT

DRAWN	W.E.	10/6/61
CHECKED	LACEY	3/19/62
ENGR APPR	[illegible]	4-27-62
APPROVED	[illegible]	4/27/62

DEVICE NO. / DWG TITLE: N.E.P.P.S. ROTOR #1 ASSEMBLIES

DWG SIZE	DWG NO	REV
D	200318	A

SHEET NO 1 OF 1

MATERIAL	SEE L.M.	
HEAT TREATMENT		
FINAL PROTECTIVE FINISH		
SCALE	FULL SIZE	

UNLESS OTHERWISE SPECIFIED DIMENSIONS ARE IN INCHES. TOLERANCES ON: FRACTIONS ± 1/64 DECIMALS ± .005 ANGLES ±

M-200811 — NEXT ASSY — USED ON — APPLICATION

FIG. 4 ROTOR #1 ASSEMBLY A-7

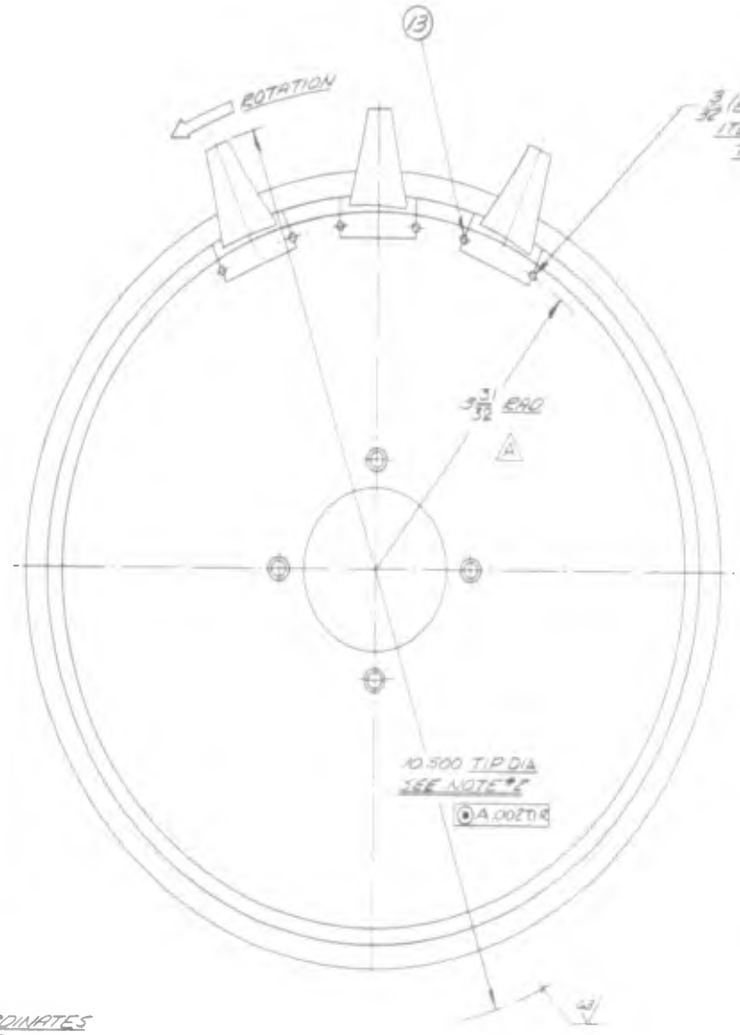

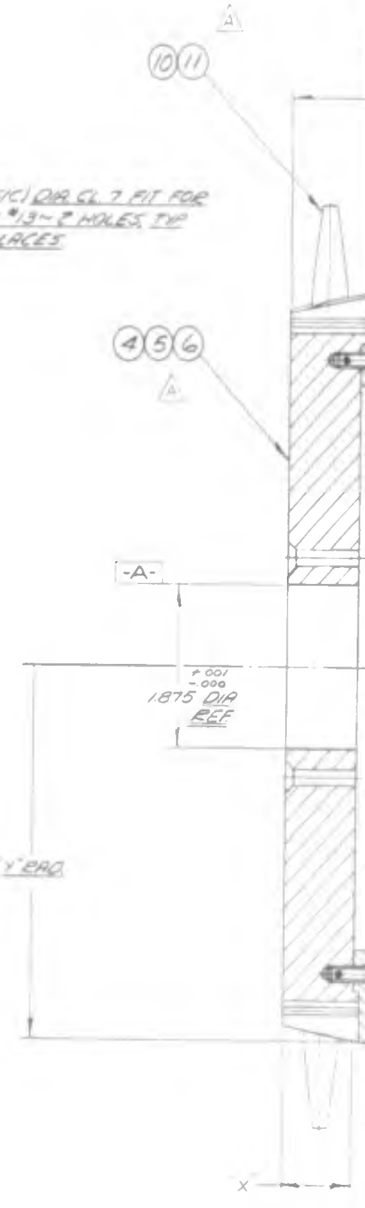

1

TABLE OF COORDINATES
SEE NOTE #1

"X"	"Y" RADIUS
.000	4.109
.500	4.185
1.000	4.281
1.500	4.357
2.000	4.445
2.500	4.520
2.930	4.590

— THIS COORDINATE FOR REF ONLY

1 2 3 ROTOR ASSY

SYM	CHG ORDER	REVISIONS	DATE	BY	APP
A		3 31/32 PAD WAS 3 15/16 PAD DELETED ITEMS #2, #5, #8, & ASSY #B FROM L/M & ALL REFERENCE TO THESE ITEMS - REVISED NOTES #1 AND #2	3 1944	REL	X78.

2

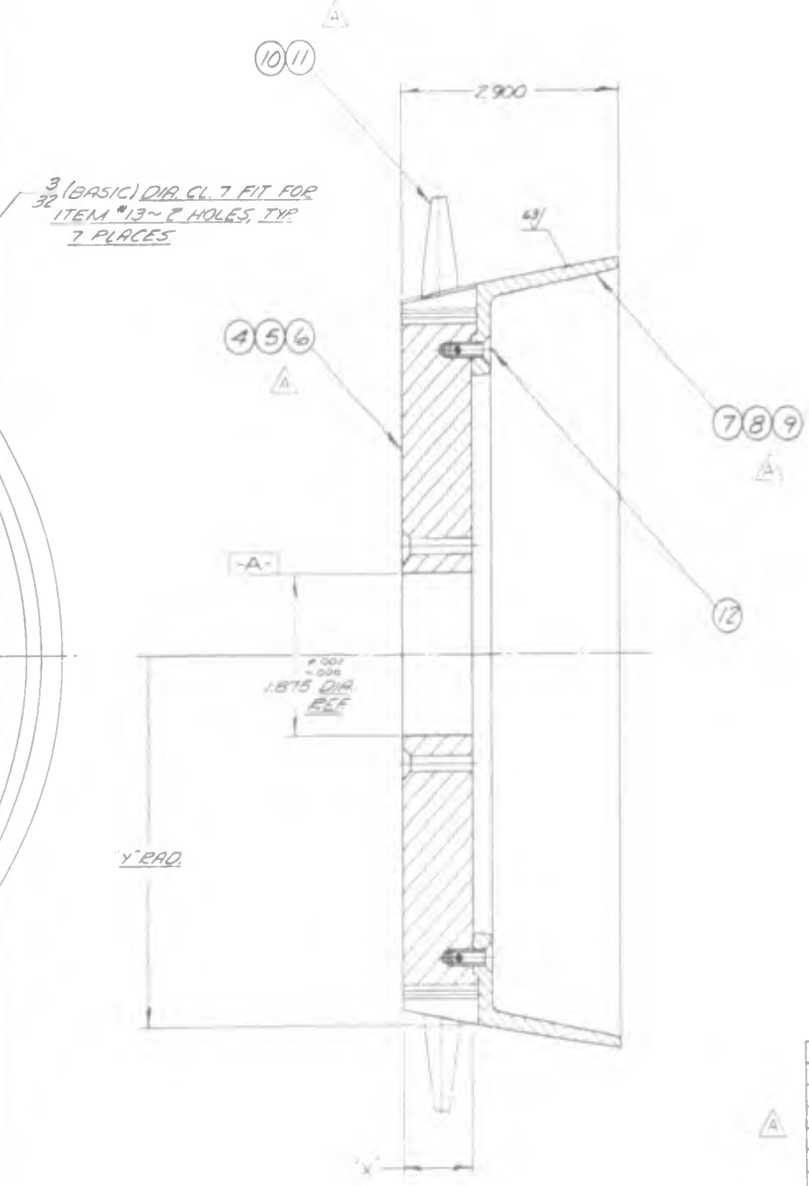

NOTES:

1. OUTSIDE CONTOUR OF ROTOR ASSY'S TO BE MACH. PER TABLE OF COORDINATES AFTER ASSY OF HUB AND EXTENSION ~ WITH BLADES OMITTED FOR ITEMS #1 & 2.
2. TIP DIA. NOTED TO BE MACHINED AFTER ASSY OF ROTOR ASSY'S ~ ITEMS #1, & 2.
3. ALL ROTOR ASSY'S TO BE STATICALLY & DYNAMICALLY BALANCED TO WITHIN.003 IN. OZ
4. BALANCING TO BE ACCOMPLISHED BY REMOVAL OF METAL ONLY.
5. AFTER ASSY. OF ROTOR ASSY'S, ITEMS #1, & 2, BLADES TO BE MATCH MARKED, 1 – 7, WITH CORRESPONDING NO'S ON RESPECTIVE HUBS TO IDENTIFY THEIR PROPER LOCATION.
6. REMOVE ALL BURRS & SHARP EDGES.

ASSY "A"	ASSY "B"	ASSY "C"	ITEM NO	PART NO	DESCRIPTION	MATL	MATL SPEC	UNIT WT
14	14	—	13		PIN, DOWEL 3/32 DIA x 1"	ST. STEEL	COM'L	
8	8	8	12	NYLOK MUTCHLOCK	SCREW, NET SOC. HD. NO. 10-32 x 3/8 LG.	ST. STEEL	COM'L	
—	7	—	11	200321-B	BLADE, ROTOR #2-B	ST. STEEL		
7	—	—	10	200321-7	BLADE, ROTOR #2-A	ST. STEEL		
—	—	1	9	200321-6	EXTENSION, ROTOR #2-C	CAST ALUM.		
—	1	—	8	200321-5	EXTENSION, ROTOR #2-B	CAST ALUM.		
1	—	—	7	200321-4	EXTENSION, ROTOR #2-A	CAST ALUM.		
—	—	1	6	200321-3	HUB, ROTOR	ALUM.		
—	1	—	5	200321-2	HUB, ROTOR	ALUM.		
1	—	—	4	200321-1	HUB, ROTOR	ALUM.		
—	—	1	3	200320-3	ROTOR ASSY. #2-C			
—	1	—	2	200320-2	ROTOR ASSY. #2-B			
1	—	—	1	200320-1	ROTOR ASSY #2-A			

QUANTITY — LIST OF MATERIAL

ASSY

UNLESS OTHERWISE SPECIFIED DIMENSIONS ARE IN INCHES. TOLERANCES ON: FRACTIONS ±1/64, DEC. PLS ±.005, ANGLES —

MATERIAL: SEE L.M.

HEAT TREATMENT: —

FINAL PROTECTIVE FINISH: —

APPLICATION

GENERAL DYNAMICS CORPORATION
ELECTRIC BOAT DIVISION GROTON CONN
RESEARCH & DEVELOPMENT DEPARTMENT

	BY	DATE
DRAWN	W.E.	7/9/62
CHECKED	LACEY	7/9/62
EXAMINED	G.P.	7/9/62
APPROVED	R.J.R.	7/9/62

SCALE: FULL SIZE

DEVICE NO. DWG TITLE: MEPPS ROTOR #2 ASSEMBLIES

CAGE SIZE: D

DWG NO: 200320

REV: L

SHEET NO: 1 OF 1

FIG. 5 ROTOR #2 ASSEMBLY A-9

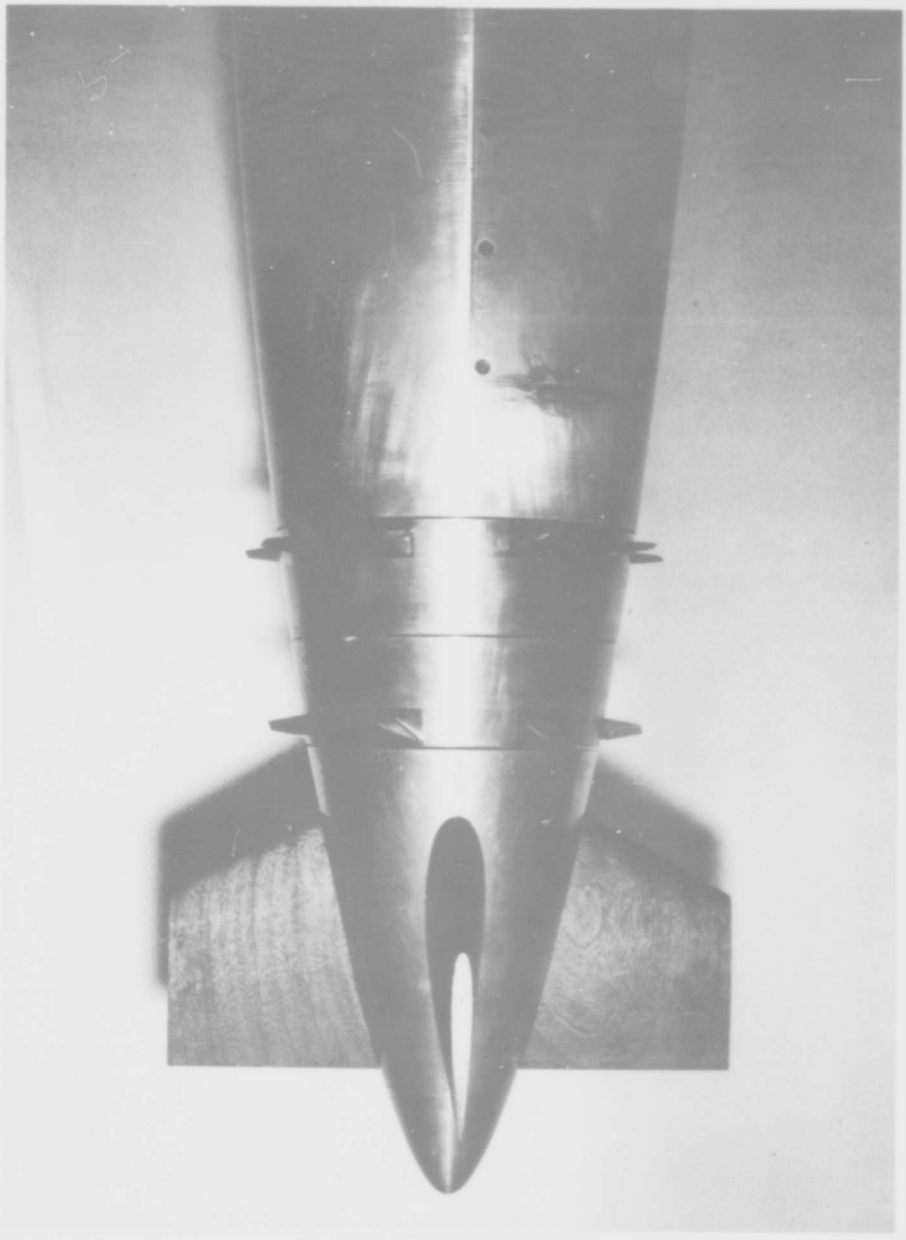

FIG. 6 PROPULSOR ASSEMBLY

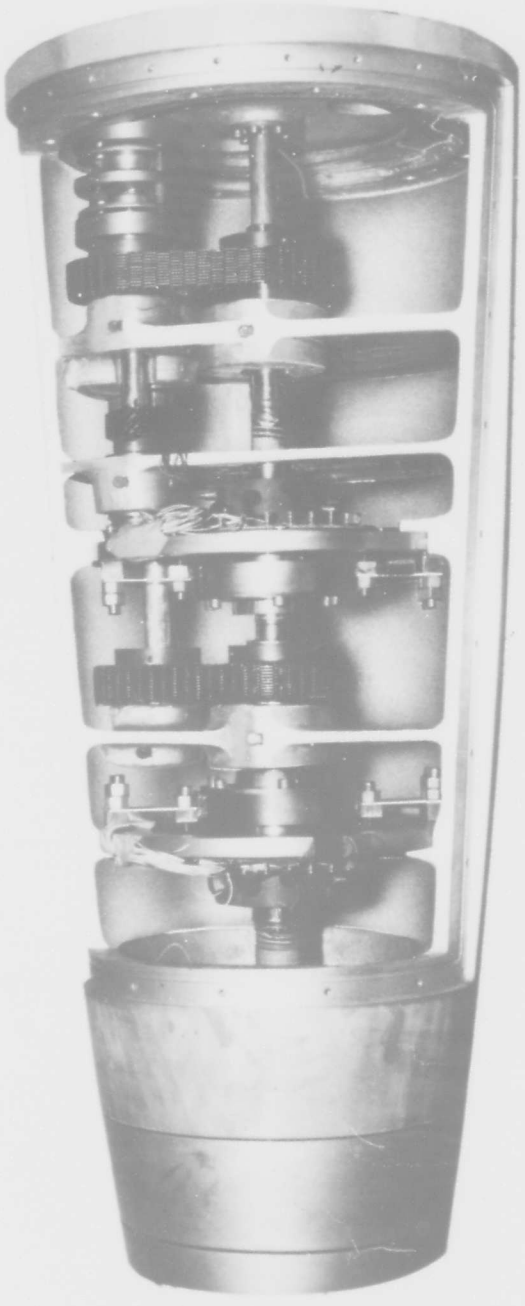

FIG. 7 PROPULSOR POWER TRAIN

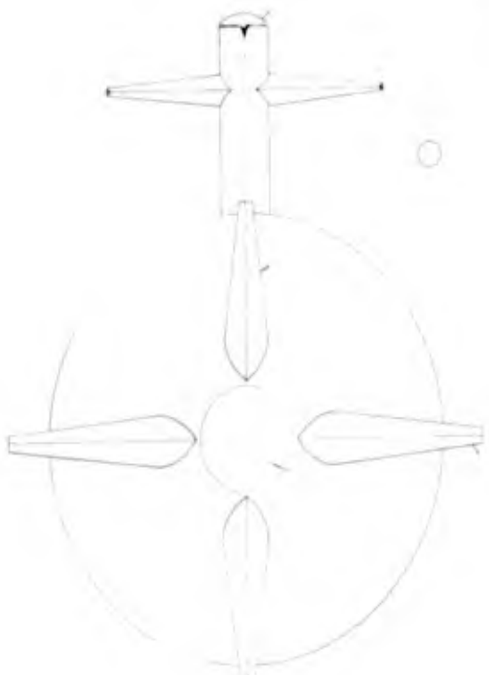

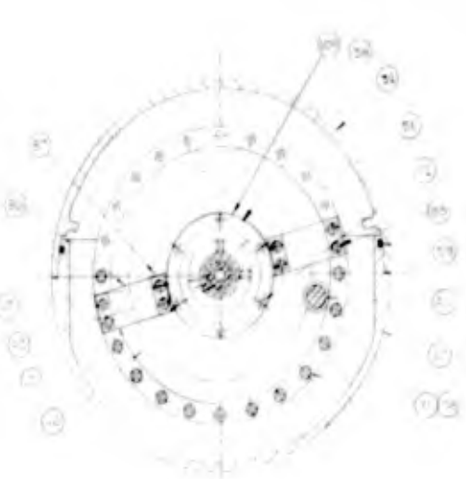

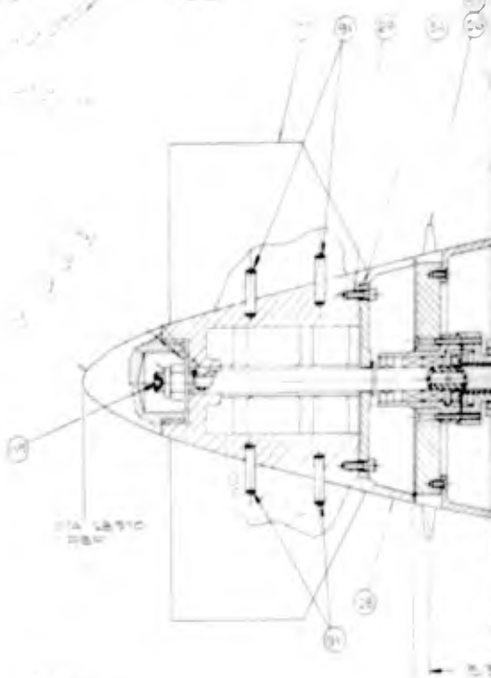

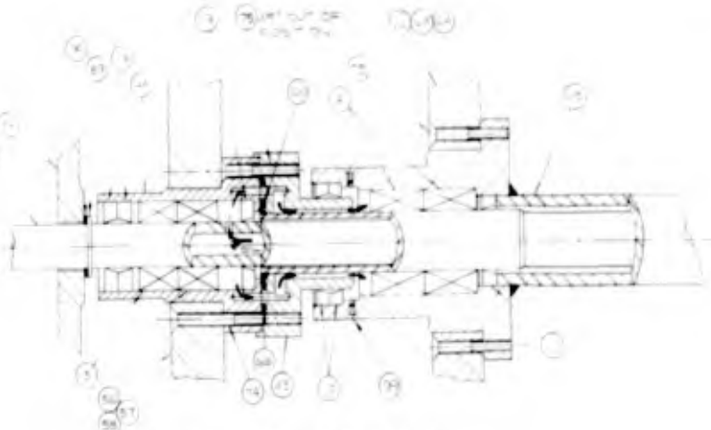

1

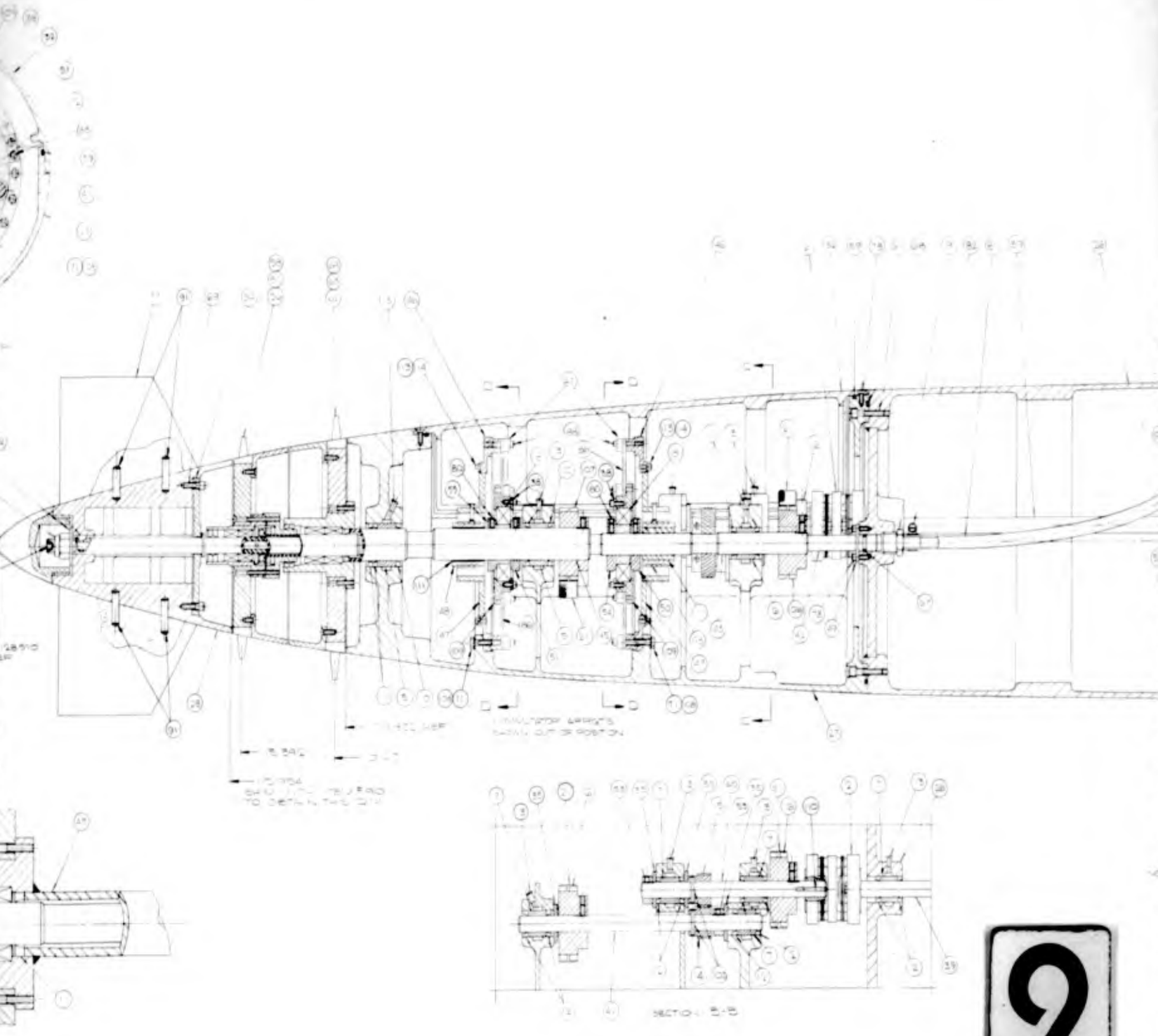

2

3

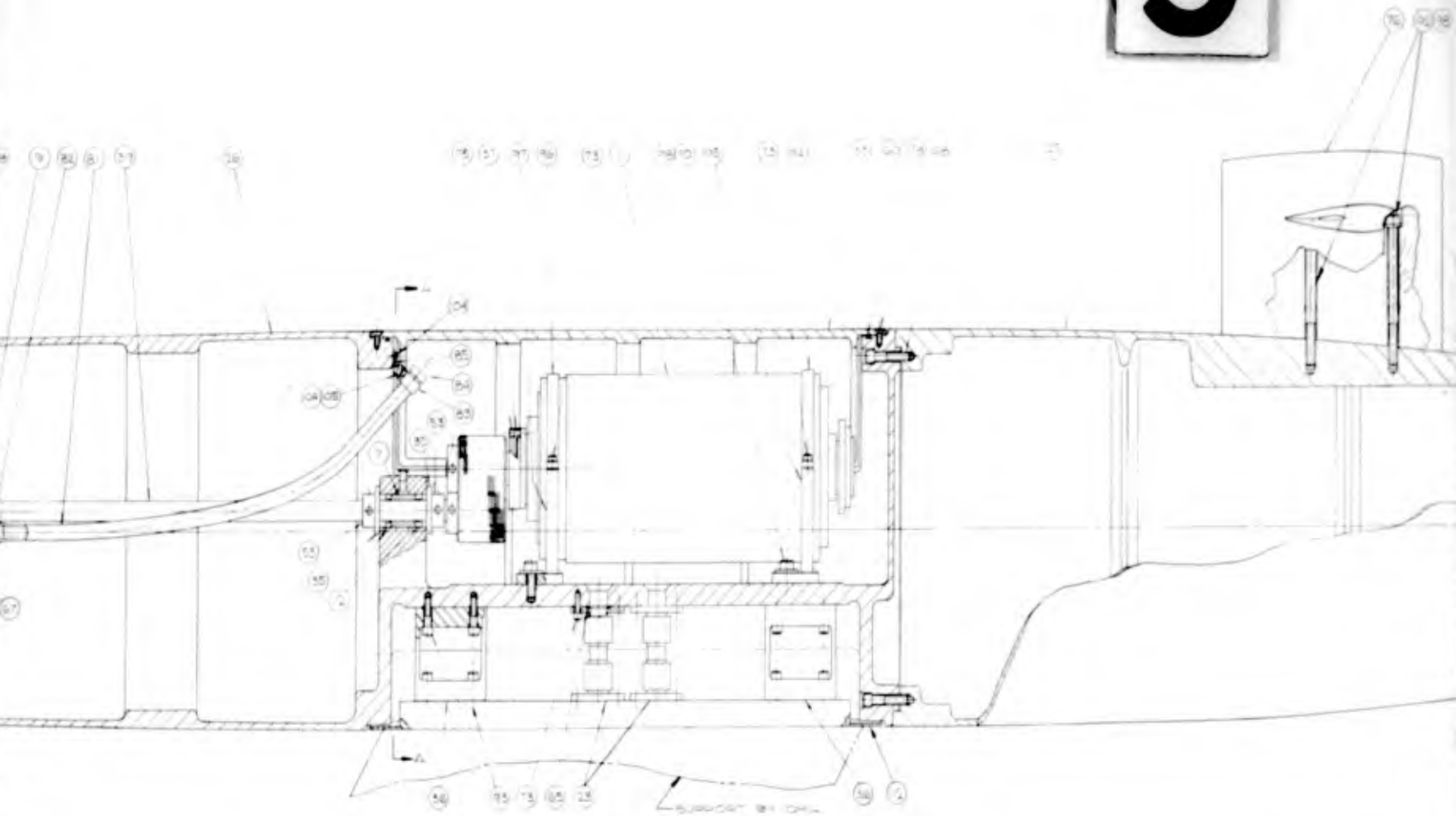

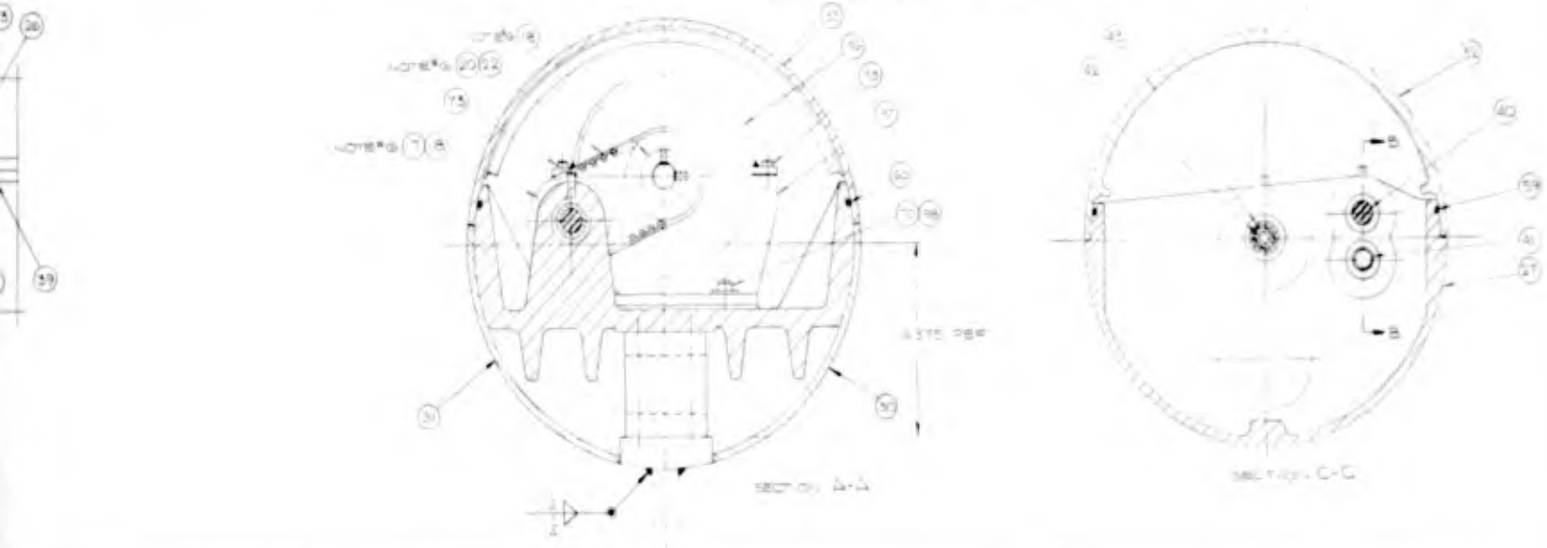

		LIST OF MATERIAL (PART
NO	QTY	DESCRIPTION
9	4	FLAT WASHER .13 DIA.
10	1	BRG HOUSING
12	*	SET SCREW
13	*	GROUNDING SHOE
14	1	MOUNTING PLATE
15	4	SOCKET SET SCREW
16	2	MOUNTING CLIP
17	1	HOLLOW HEX PLUG

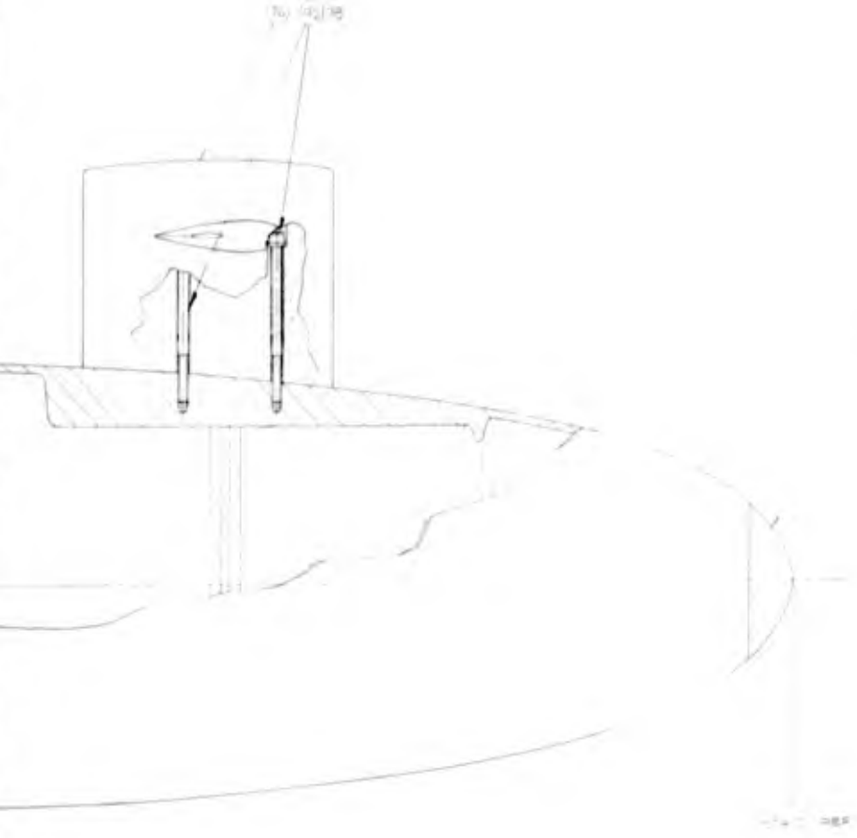

4

FIG. 8 M

LIST OF MATERIAL CONT'D

ITEM NO	REQD	PART NO	DESCRIPTION	MATL	MATL SPEC	
108	20	[illegible]	FLT WASHER 1/4 DIA	CRES		
109	2	200329-2	BRG HOUSING			
110	2		KEY 1/16 SQ x [illegible] LG	CRES		
111	2	BY ORL	COMMUTATOR SHIM	STL		
112	1	200330-1	MOUNTING PLATE	STL		
113	12	[illegible]-4P	SOC HD CAP SCR #4-40	CRES		
114	12	P.C. CAT NO [illegible]-1	MOUNTING CLEAT	ST ST		
115	1	PARKER [illegible]	HOLLOW HEX PLUG	STL		

NOTES

1. ITEM #14 HELICAL GEAR TO BE [illegible] 24 [illegible] BORE [illegible] FACE [illegible] CAT NO [illegible] ITEM #15 HELICAL GEAR TO BE [illegible] 24 NOM BORE [illegible] FACE [illegible] CAT NO [illegible] AS SUPPLIED BY MORSE CHAIN CO. 80 CHURCH ST. NEW YORK.
2. ITEM #4 TO BE McGILL GAGEROL BRG OUTER RING NO MR-20-N, INNER RING NO [illegible] 1000 NOM BORE. ITEM #3 TO BE McGILL GAGEROL BRG OUTER RING NO MR-[illegible]-N, INNER RING NO [illegible] .750 NOM BORE.
3. ITEM #2 TO BE THOMAS FLEXIBLE COUPLING NO. 6 DBZ WITH .750 BORE WITH 3/16 STD KEYWAY NOM THOMAS FLEXIBLE COUPLING COMPANY, WARREN, PENN.
4. SPROCKET ITEMS #16, 17, 18, #106 AND #107 TO BE AS FOLLOWS

	PD	TEETH	BORE	FACE	HUB DIA
ITEM #16	3.349	28	.75	[illegible]	[illegible]
#17	4.534	38	.75	[illegible]	[illegible]
#18	2.278	9	.75	[illegible]	[illegible]
#106	3.349	28	.50	[illegible]	[illegible]
#107	3.349	28	.50	[illegible]	[illegible]

TO BE [illegible] AND SUPPLIED WITH TWO 1/4-20 NYLOK SOC SET SCRS 3/8 LG AS SUPPLIED BY MORSE CHAIN CO. 80 CHURCH ST. NEW YORK, N.Y.

5. SILENT CHAINS ITEMS #20, #21 AND #22 TO BE AS FOLLOWS

	PITCHES	[illegible]	CAT NO
ITEM #20	50	[illegible]	#305
#21	48	[illegible]	#304
#22	40	[illegible]	#306

6. [illegible]
7. ALL COMMERCIAL ITEMS TO BE EQUAL TO THOSE RECOMMENDED.
8. O RINGS ITEMS #59 AND #60 TO BE MADE TO SUIT AT ASSY.

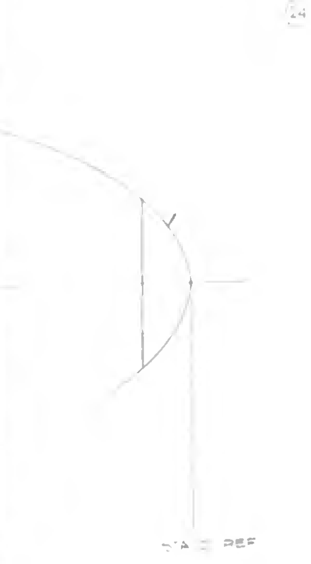

5

ITEM NO	REQD	PART NO	DESCRIPTION	MATL	MATL SPEC	
107	1	NOTE #4	SPROCKET			
106	1	NOTE #4	SPROCKET			
105	1	[illegible]	HEX NUT #8-32	CRES		
104	2		RD HD MACH SCR #8-32	CRES		3/8 LG
103	2		DOWEL 1/8 DIA x 1/4	CRES		
102	1		FLAT WASHER 9/16 MED	CRES		
101	1	[illegible]	ELAS STOP NUT 9/16-18	CRES		
100	1	[illegible]	O RING 1 3/8 ID x 1/16	BUNA N		
99	2	[illegible]	FLT HD MACH SCR #2-40	CRES		3/16 LG
98	6	[illegible]	FLT WASHER 3/8 MED	CRES		
97	1	200333-1	MOUNT, MOTOR FRONT	STL		
96	1	200333-3	STRAP, MOTOR FRONT	STL		
95	1	200333-2	MOUNT, MOTOR REAR	STL		
94	1	200333-4	STRAP, MOTOR REAR	STL		
93	16	[illegible]	SOC HD CAP SCR 1/4-20	CRES		1 1/4 LG
92	[illegible]	[illegible]	SOC HD CAP SCR 5/16-18	CRES		[illegible] LG
91	8		DOWEL 1/8 DIA x 1/2	CRES		
90	[illegible]		SHIM LAM [illegible]	BRASS		
89	1	[illegible]	RETAINING RING	STL		
88	16	[illegible]	SOC HD CAP SCR 1/4-28	CRES		[illegible] LG
87	4	BY ORL	PAD	-		
86	2	BY ORL	FLEXTURE PC	-		
85	1	200333-6	STAND OFF	STL		
84	[illegible]	200333-8	PLUG	PLASTIC		
83	[illegible]	[illegible]	TUBE CLIP 1/2 O	STL		
82	1	[illegible]	TUBE CLAMP 1/2 OD	CRES		
81	[illegible]		FLEX TUBING 1/2 OD [illegible]	PLASTIC		
80	8	[illegible]	SOC SET SCR 1/4-20	CRES		3/8 LG
79	2	200333-	STABILIZER	WOOD		
78	109	[illegible]	FLT HD MACH SCR #10-24	CRES		1/2 LG
77	2	200333-2	RUDDER	WOOD		
76	1	200332-1	SAIL ARRGT	WOOD		
75	6	[illegible]	FLT HD MACH SCR #10-24	CRES		[illegible] LG
74	6	[illegible]	FLT HD MACH SCR #10-24	CRES		[illegible] LG
73	32	[illegible]	SOC HD CAP SCR #10-24	CRES		[illegible] LG
72	12	[illegible]	SOC HD CAP SCR #10-24	CRES		[illegible] LG
71	24	[illegible]	HEX HD BOLT 1/4-20	STL		[illegible] LG
70	4	[illegible]	SOC HD CAP SCR [illegible]-18	CRES		[illegible] LG
69	4	[illegible]	SOC HD CAP SCR #10-24	CRES		3/4 LG
68	24	[illegible]	SOC HD CAP SCR 1/4-20	CRES		[illegible] LG
67	1	[illegible]	O RING 5/8 ID x 1/16	BUNA N		
66	[illegible]	[illegible]	O RING 2 ID x 1/16	BUNA N		
65	2	[illegible]	O RING 3/4 ID x 1/16	BUNA N		
64		[illegible]-3	ROTOR ASSY #1-C	-		
63		[illegible]-2	ROTOR ASSY #1-B	-		
62		[illegible]-1	ROTOR ASSY #1-A	-		
61		[illegible]	O RING [illegible] ID x 1/8	BUNA N		
60		NOTE #8	O RING 1/8 SECTION	BUNA N		
59	1	NOTE #8	O RING 1/8 SECTION	BUNA N		
58		200320-2	ROTOR ASSY #2-B	-		
57	1	200320-1	ROTOR ASSY #2-A	-		
56		200320-3	ROTOR ASSY #2-C	-		
55	1	200328-5	BRG BUSHING	CRES		
54		200328-6	BRG BUSHING	CRES		
53	4	[illegible]	COLLAR	STL		
52		MFG NO 3	WOODRUFF KEY 1/16 x 5/8	CRES		
51	1	200328-2	BRG COLLAR	CRES		
50	1	200328-1	BRG COLLAR	CRES		
49	1	200333-7	RETAINER PLATE	CRES		
48	2	BY ORL	COMMUTATOR ROTOR	-		
47	2	BY ORL	COMMUTATOR STATOR	-		
46	2	200329-1	SUPPORT RING	STL		
45		200326-1	SHAFT-FWD PROP	CRES		
44	1	200325-2	HUB-AFT PROP	CRES		
43		200325-1	SHAFT-AFT PROP	CRES		
42		200326-2	SHAFT-CENTER	CRES		
41		200327-3	SHAFT-IDLER	CRES		
40		200327-2	SHAFT-JACK	CRES		
39		200327-1	SHAFT-MAIN DRIVE	CRES		
38	2	200329-3	BRG RETAINER RING	STL		
37		200333-5	ADAPTER, MTR SHAFT	STL		
36	2	200328-4	SUPPORT BLOCK	CRES		
35	2	[illegible]	WASHER, THRUST	[illegible]		
34		[illegible]-5	SUPPORT, SHAFT	ALUM		
33		[illegible]-1	COVER, MOTOR	ALUM		
32		[illegible]-2	COVER, GEARING	ALUM		
31		[illegible]-3	COVER, BOTTOM RIGHT	ALUM		
30		[illegible]-4	COVER, BOTTOM LEFT	ALUM		
29		[illegible]	TAIL	ALUM		
28		[illegible]-3	SECTION FOUR	ALUM		
27		[illegible]	SECTION THREE	ALUM		
26		[illegible]	SECTION TWO	ALUM		
25		[illegible]	SECTION ONE	ALUM		
24		[illegible]	NOSE	ALUM		
23	2	200328-3	BELLOWS ASSY	-		
22		NOTE #5	CHAIN, SILENT	COML		
21	2	NOTE #5	CHAIN, SILENT	COML		
20		NOTE #5	CHAIN, SILENT	COML		
19	3	[illegible]	SEAL	COML		
18	2	NOTE #4	SPROCKET	COML		
17		NOTE #4	SPROCKET	COML		
16		NOTE #4	SPROCKET	COML		
15		NOTE #1	GEAR HELICAL	COML		
14		NOTE #1	GEAR HELICAL	COML		
13	4	[illegible]	OIL HOLE COVER	COML		
12		[illegible]	SEAL	COML		
11		[illegible]	SEAL	COML		
10		[illegible]	SEAL	COML		
9		[illegible]	ADAPTER, TUBE	BRASS		
8		[illegible]	BRG BALL	COML		
7	3	[illegible]	BRG SLEEVE 3/4 BORE	COML		
6		[illegible]	BRG SLEEVE [illegible] BORE	COML		
5		[illegible]	BRG SLEEVE 1/2 BORE	COML		
4		NOTE #2	BRG GAGEROL	COML		
3		NOTE #2	BRG GAGEROL	COML		
2		NOTE #3	COUPLING	COML		
1		BY ORL	MOTOR	-		

LIST OF MATERIAL

NERPS
GEN ARRANGEMENT
2003[illegible]

FIG. 8 MODEL GENERAL ARRANGEMENT

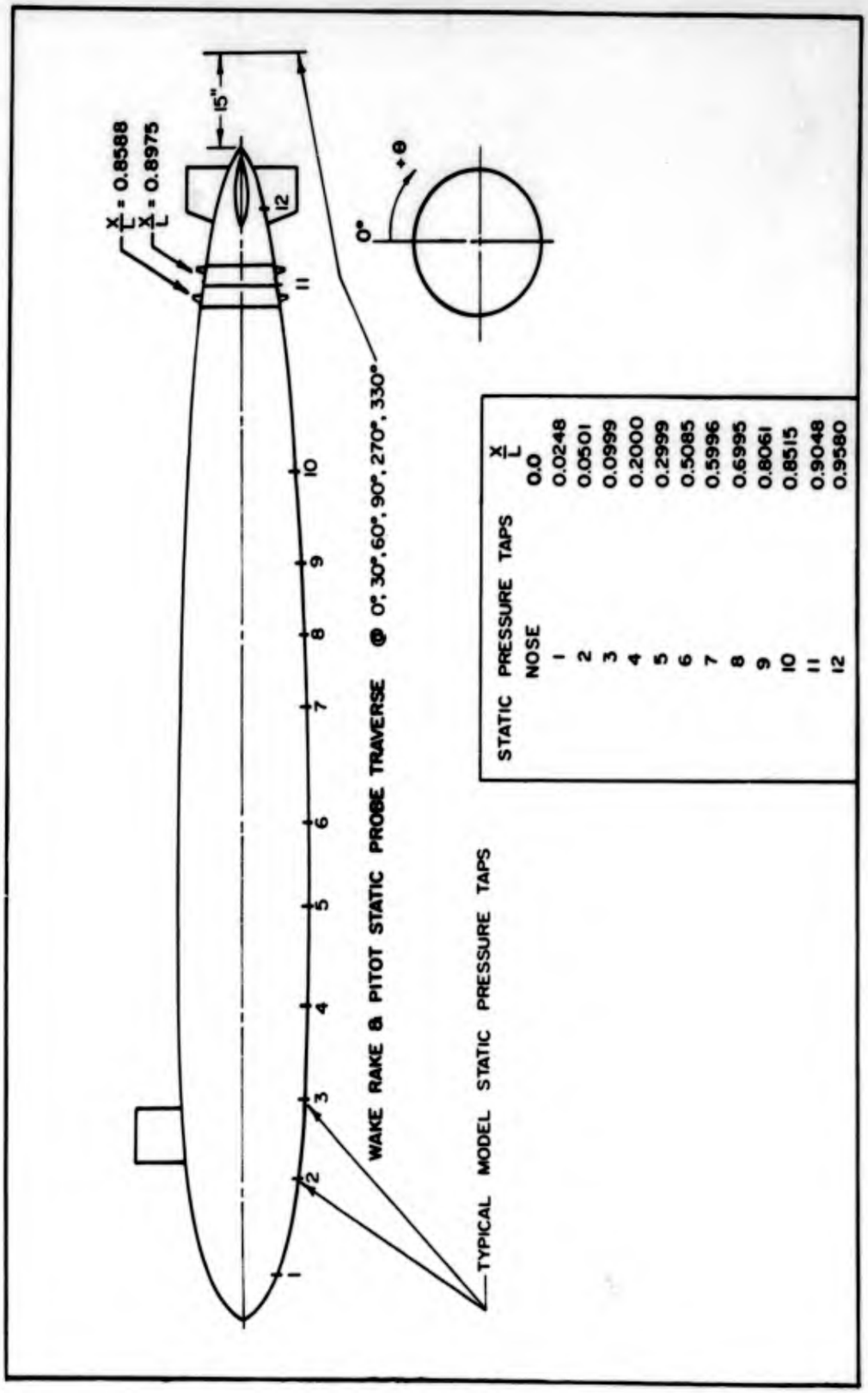

FIG. 9 LOCATION OF MODEL INSTRUMENTATION

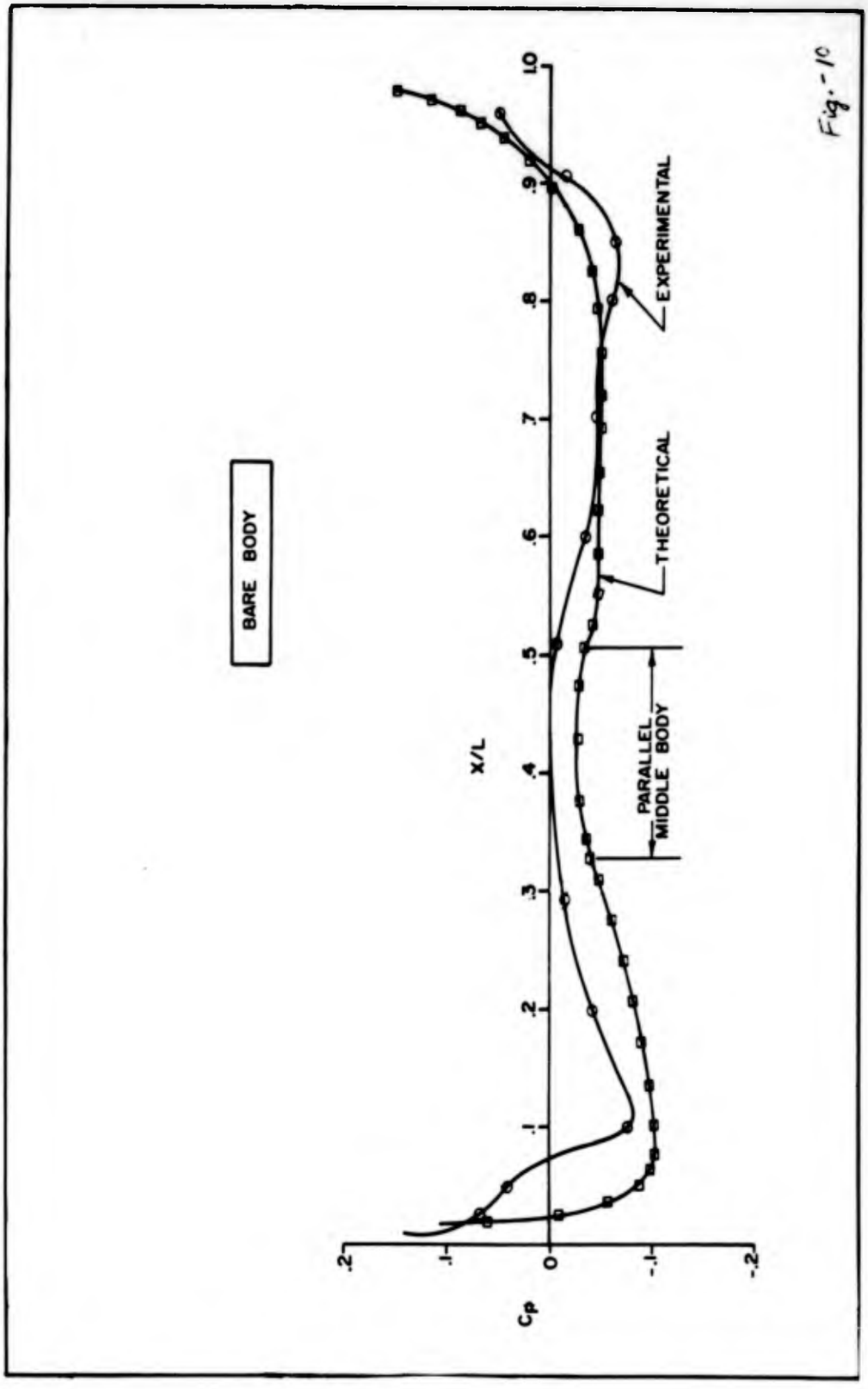

FIG. 10 COMPARISON OF EXPERIMENTAL AND THEORETICAL PRESSURE DISTRIBUTION

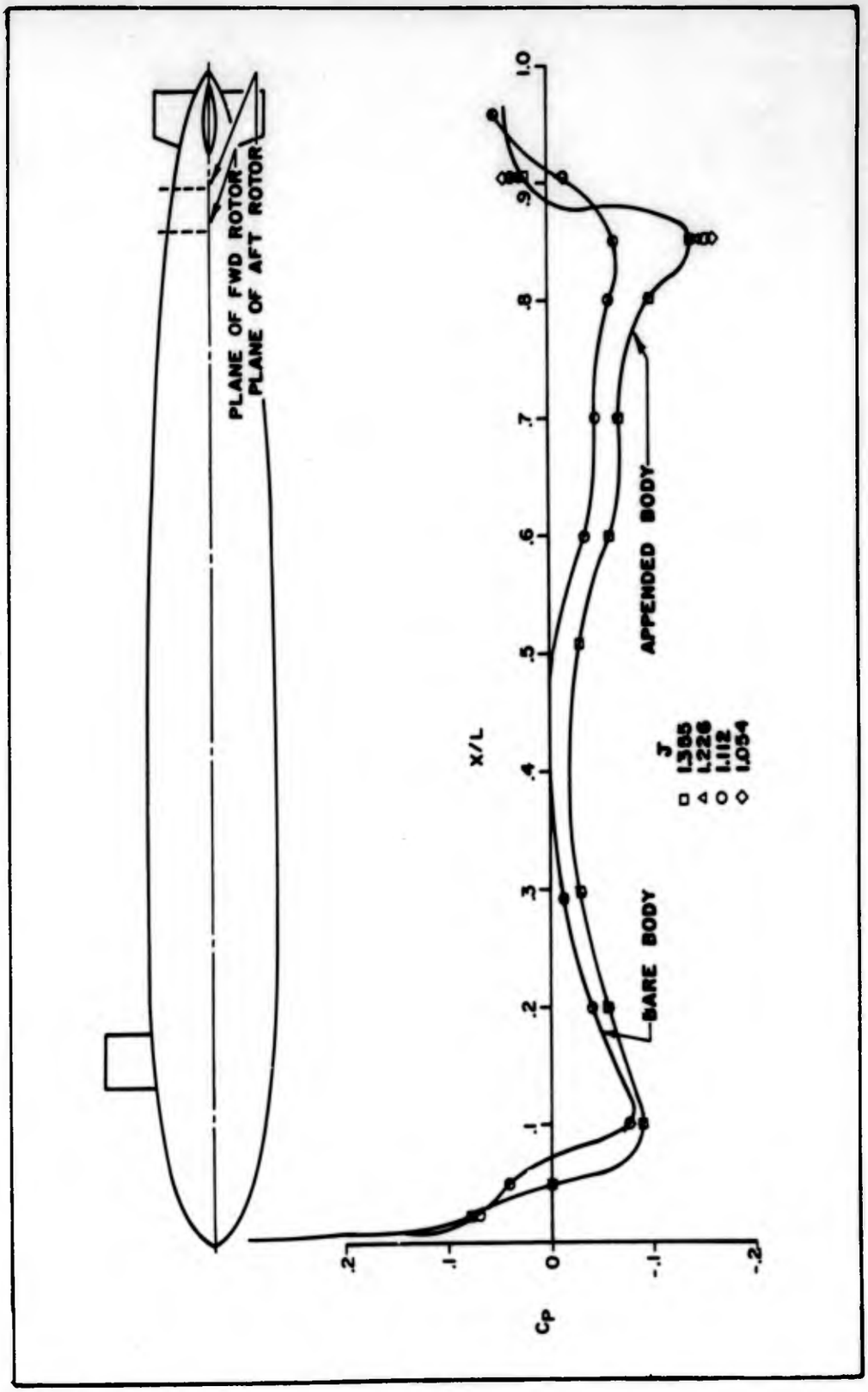

FIG. 11 EFFECT OF PROPULSOR AND APPENDAGES ON PRESSURE DISTRIBUTION

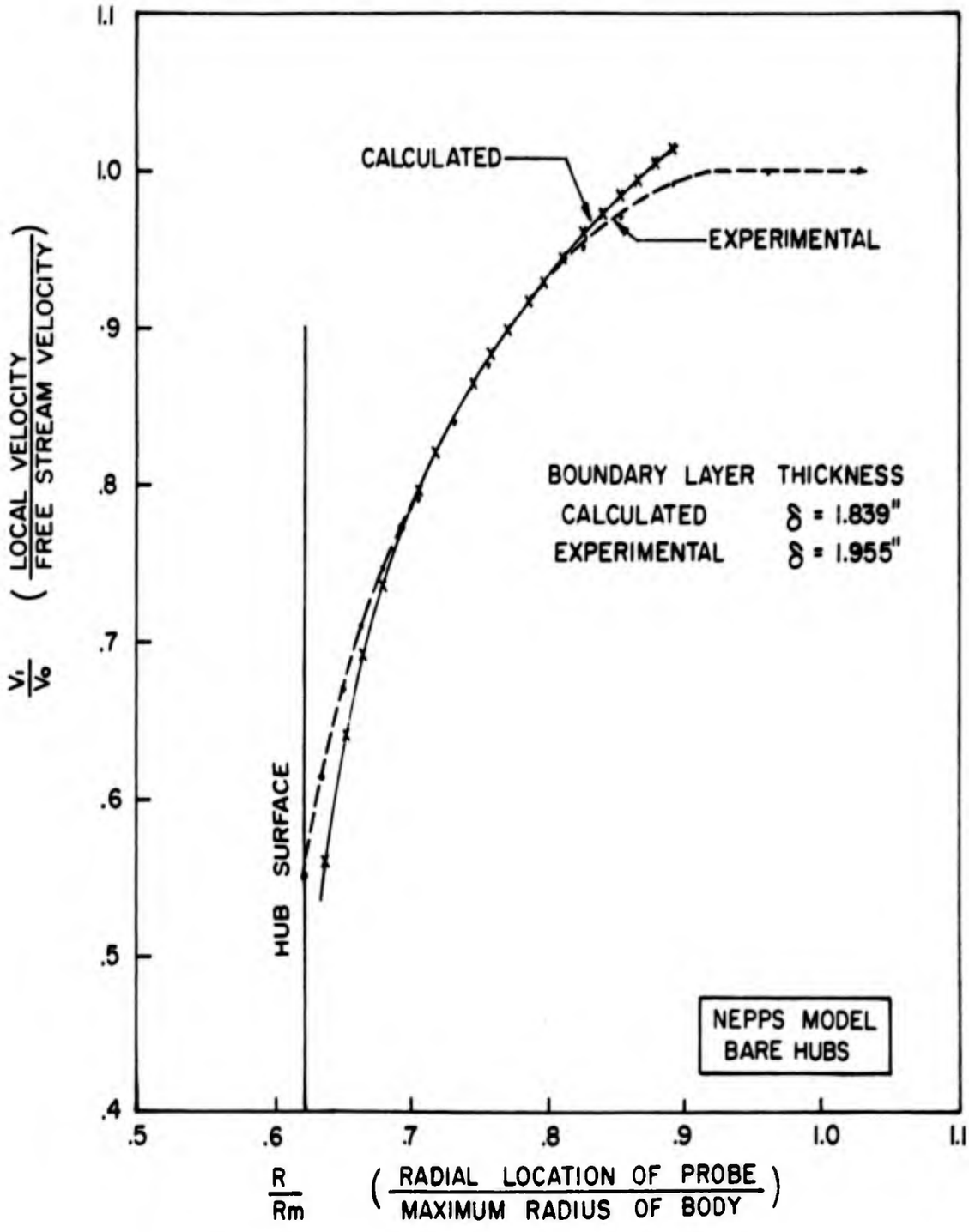

FIG. 12 COMPARISON OF CALCULATED AND MEASURED BOUNDARY LAYER VELOCITY PROFILES

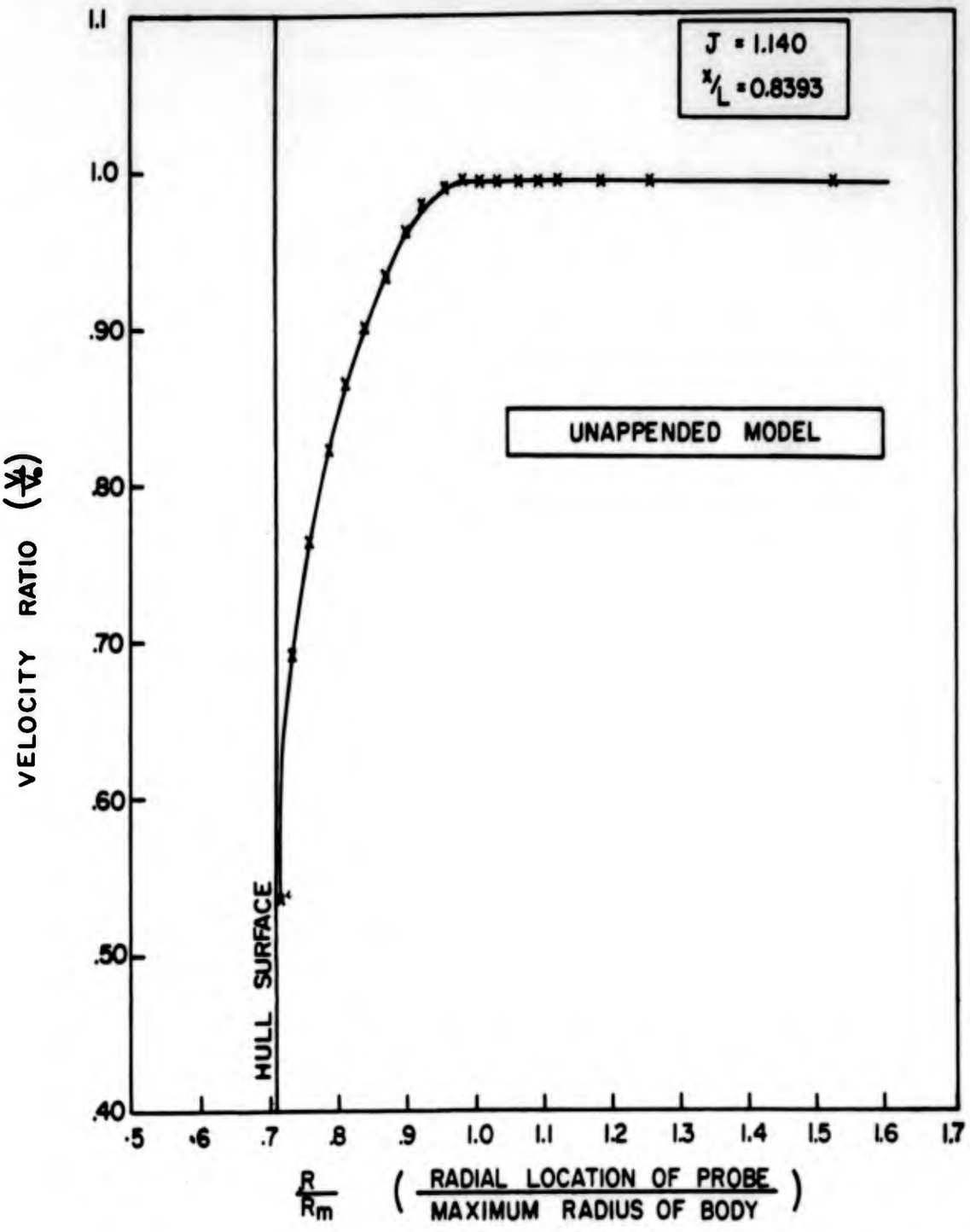

FIG. 13 VELOCITY PROFILE FORWARD OF FIRST HUB (PROPULSOR OPERATING)

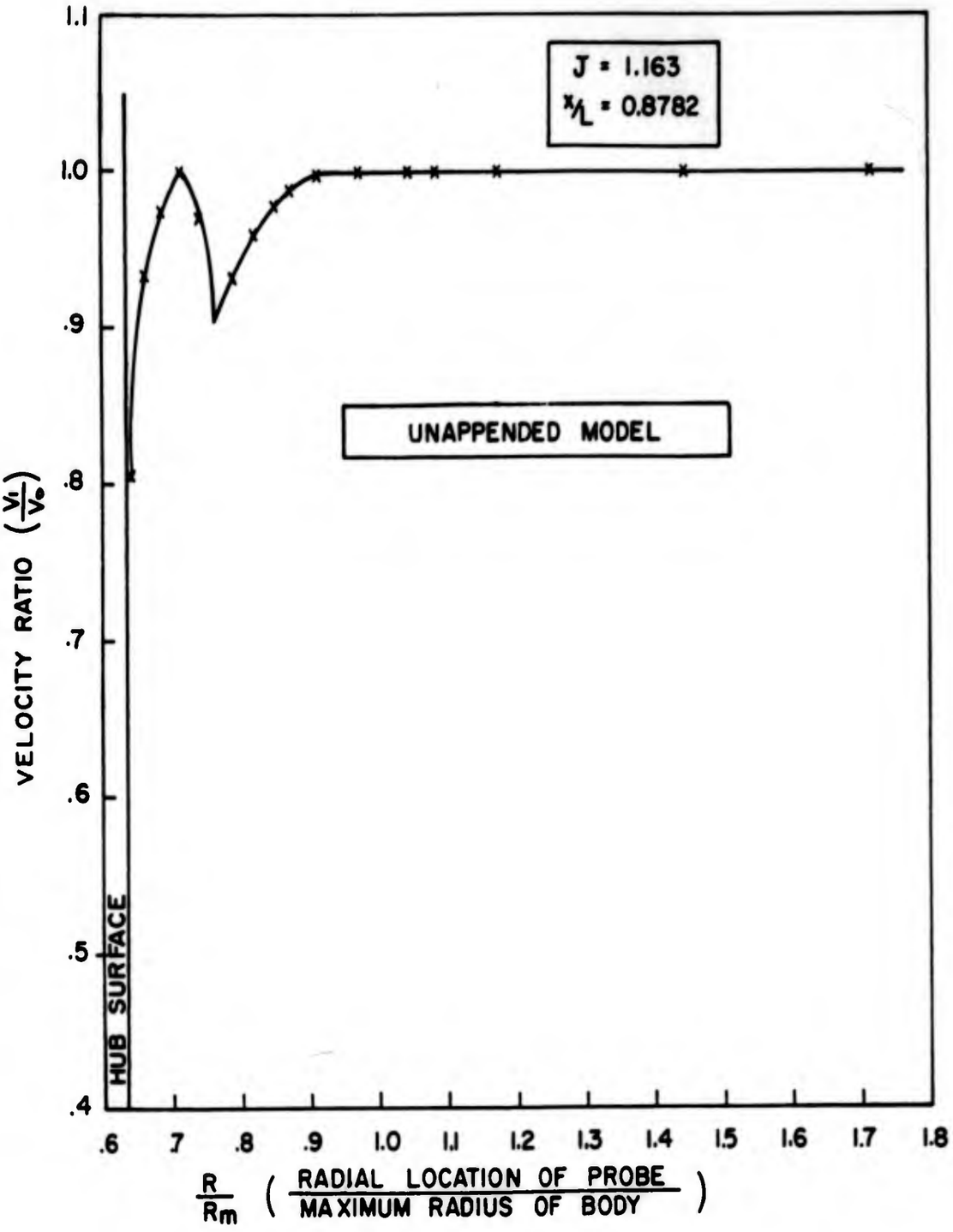

FIG. 14 VELOCITY PROFILE BETWEEN ROTORS (PROPULSOR OPERATING)

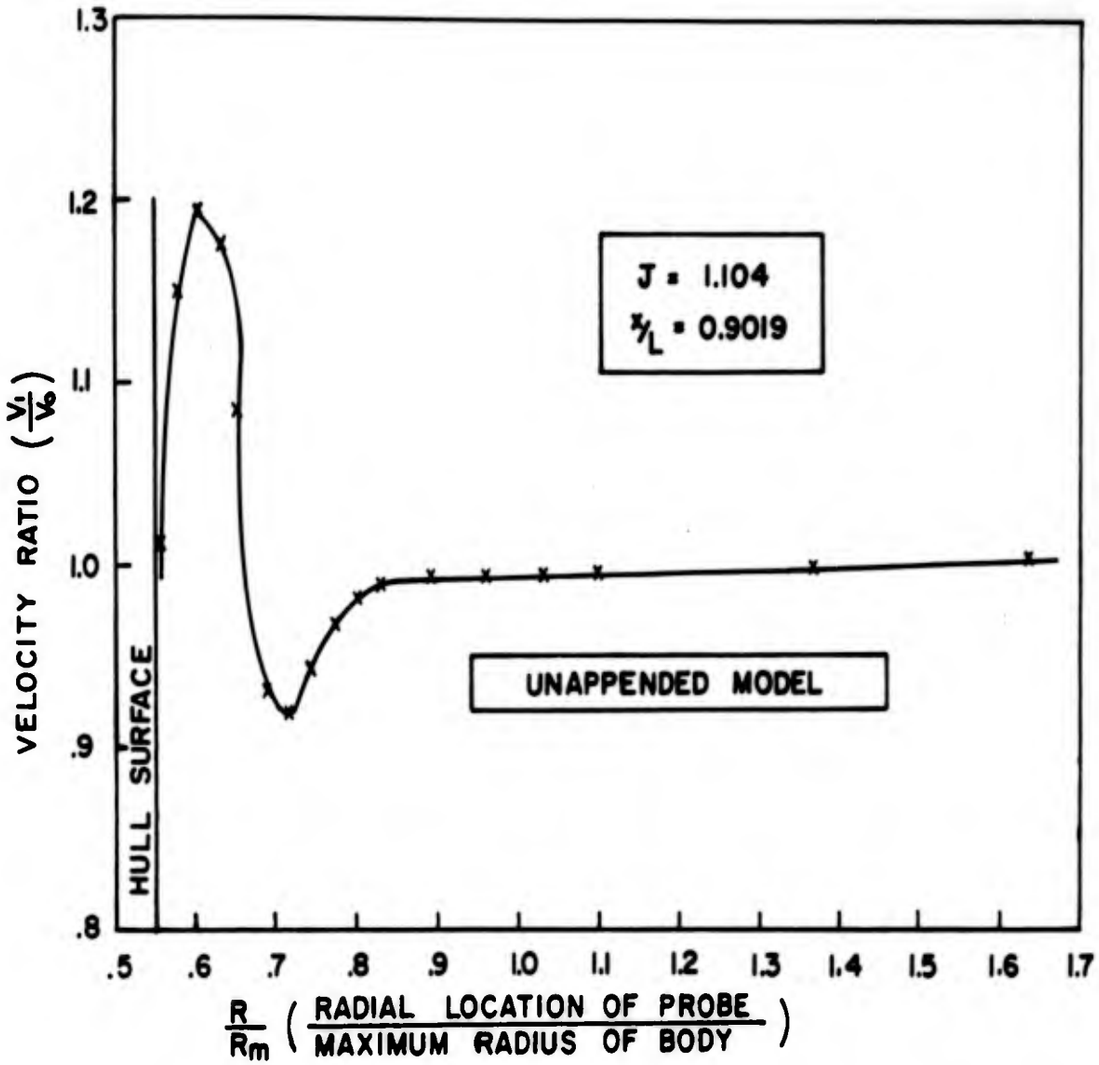

FIG. 15 VELOCITY PROFILE AFT OF REAR HUB (PROPULSOR OPERATING)

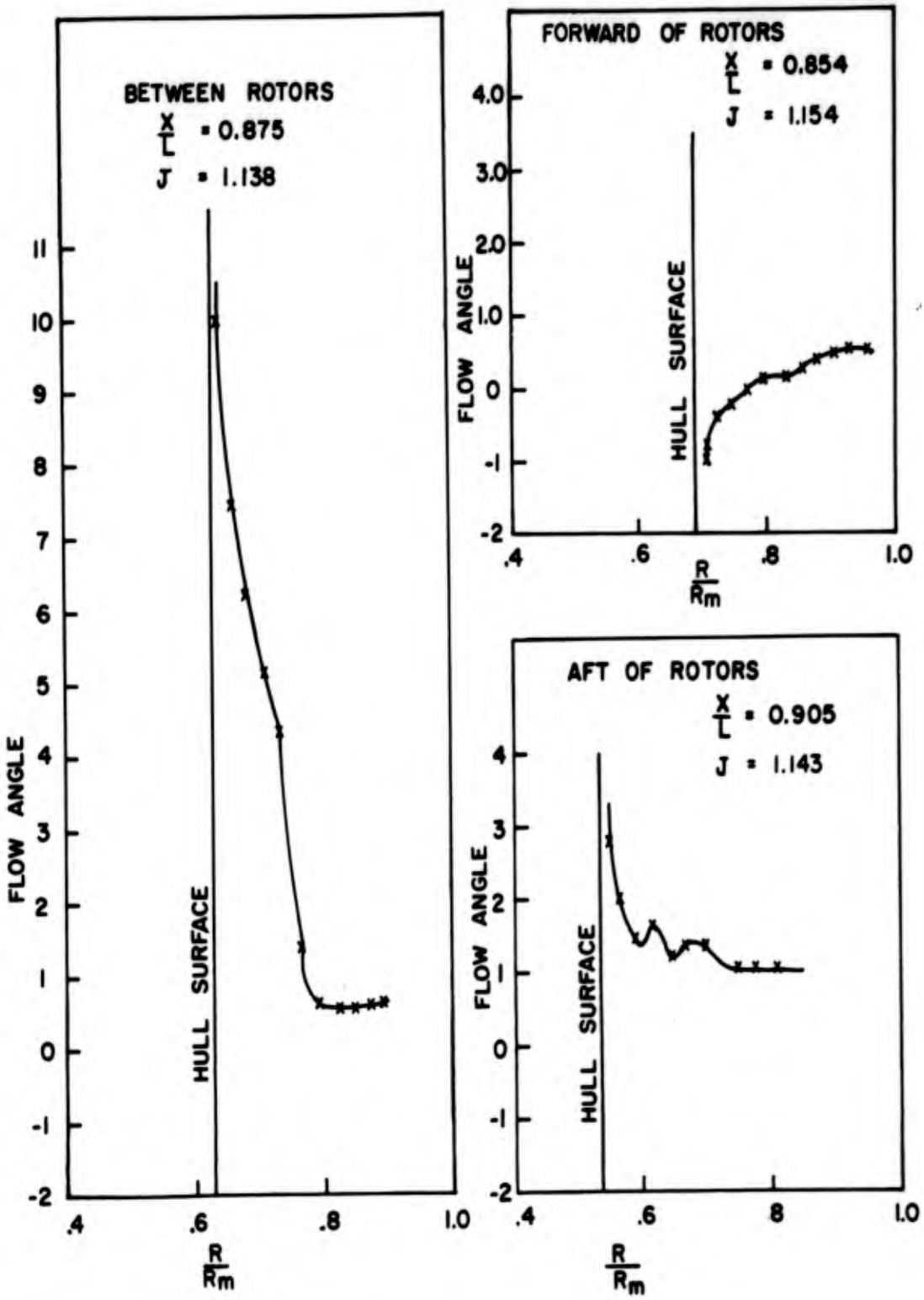

FIG. 16 FLOW ANGULARITY, UNAPPENDED MODEL

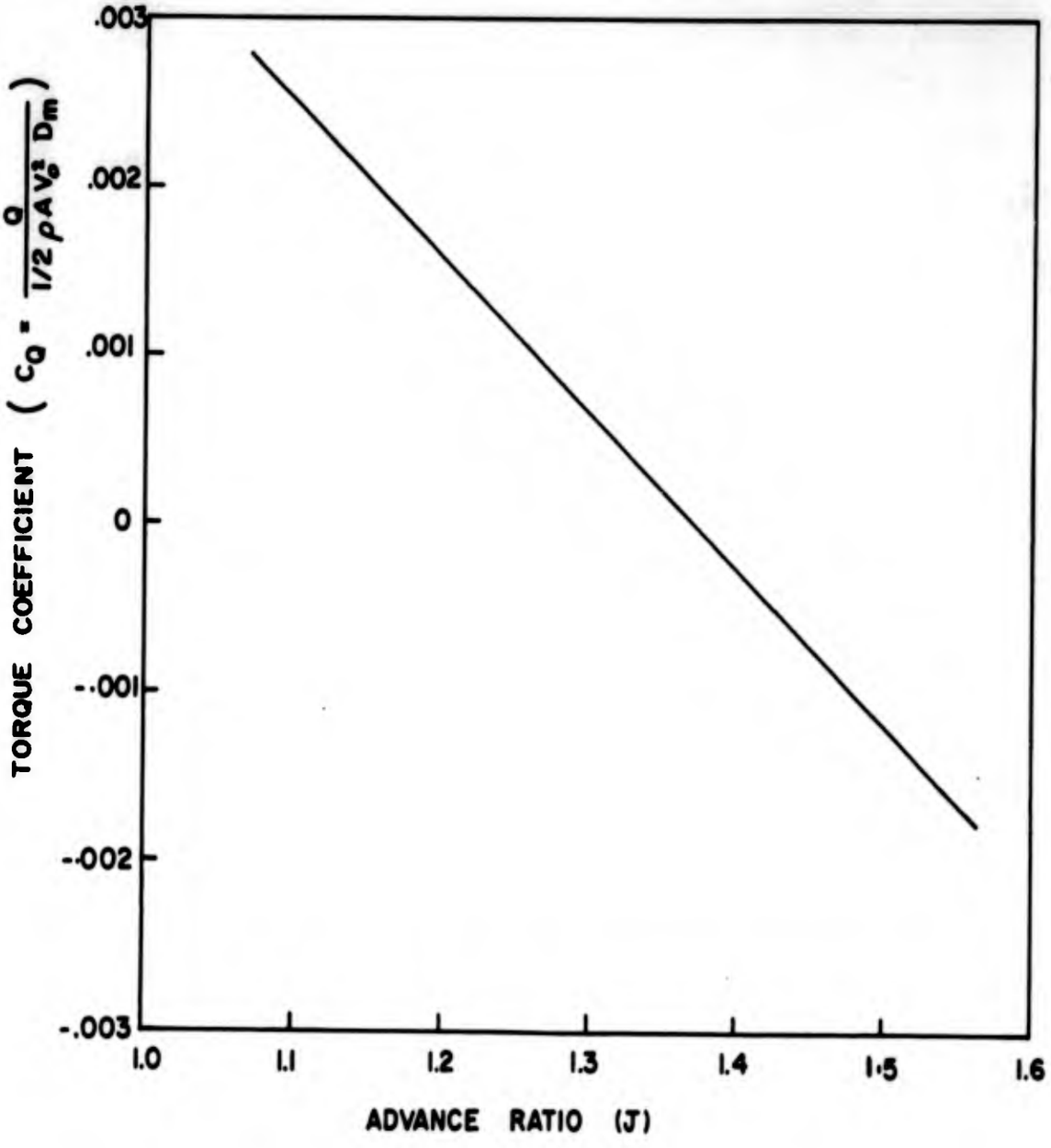

FIG. 17 FIN TORQUE COEFFICIENT VS. ADVANCE RATIO

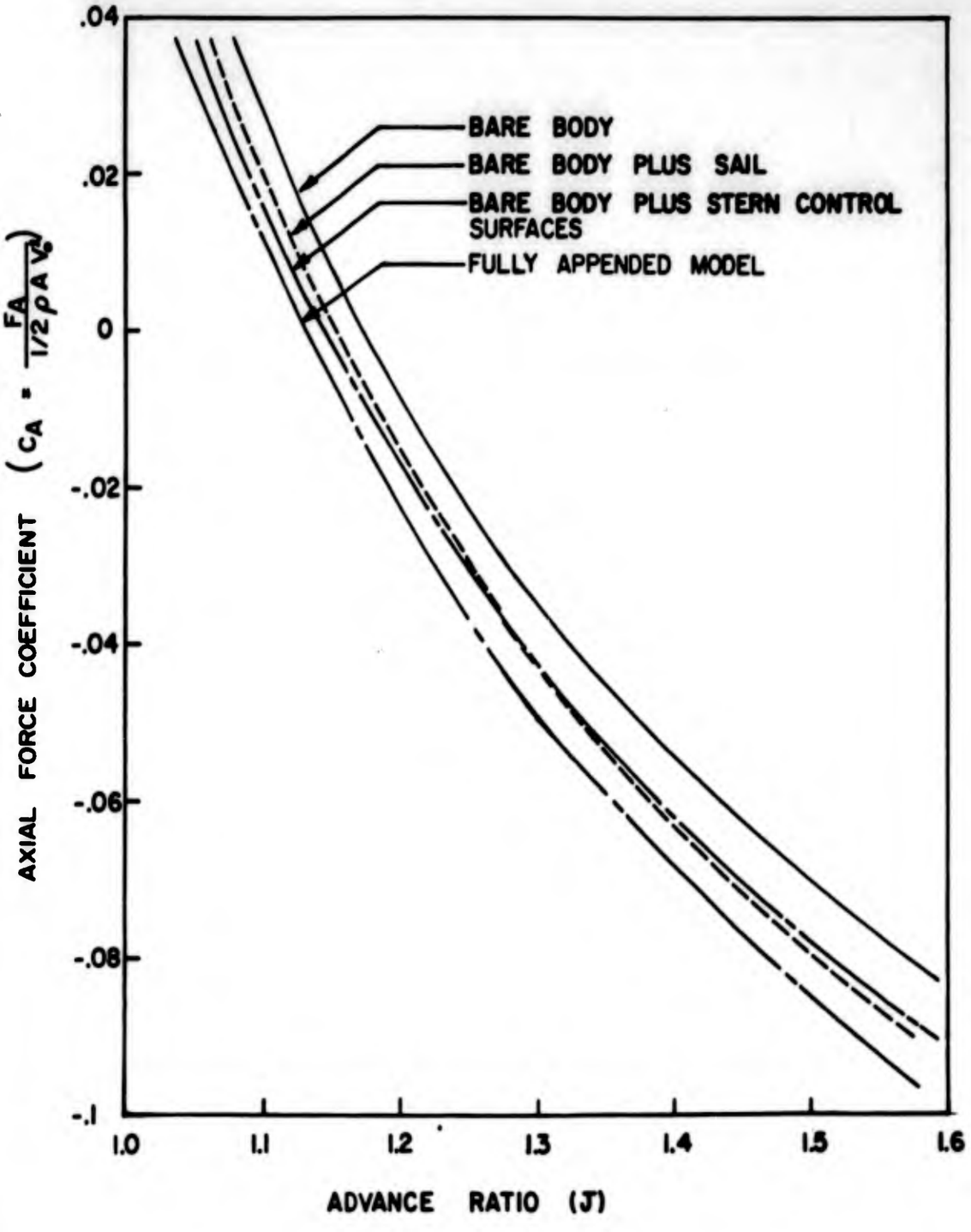

FIG. 18 AXIAL FORCE COEFFICIENT VS. ADVANCE RATIO

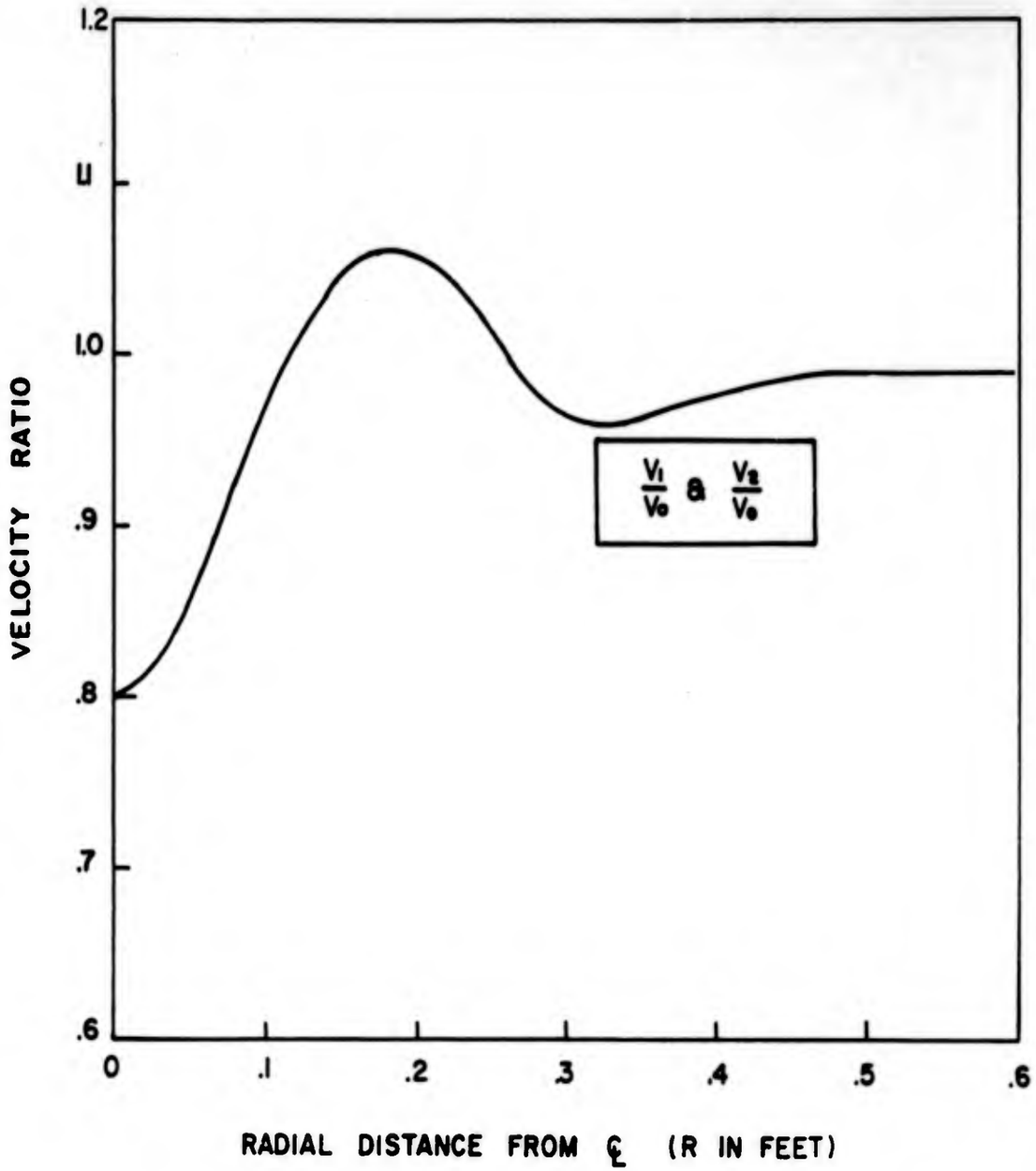

FIG. 19 WAKE SURVEY, BARE BODY, POWERED

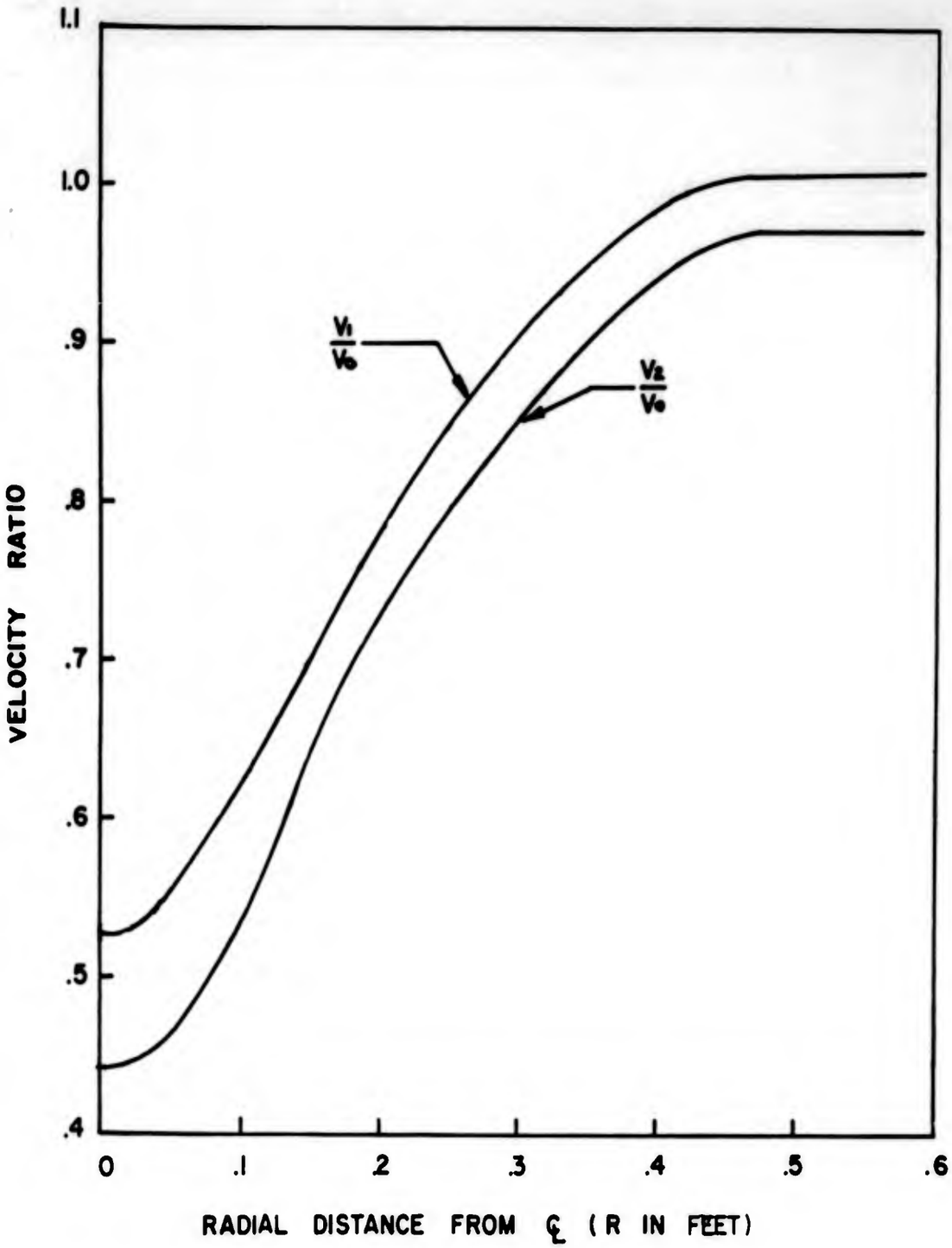

FIG. 20 WAKE SURVEY, BARE BODY, UNPOWERED

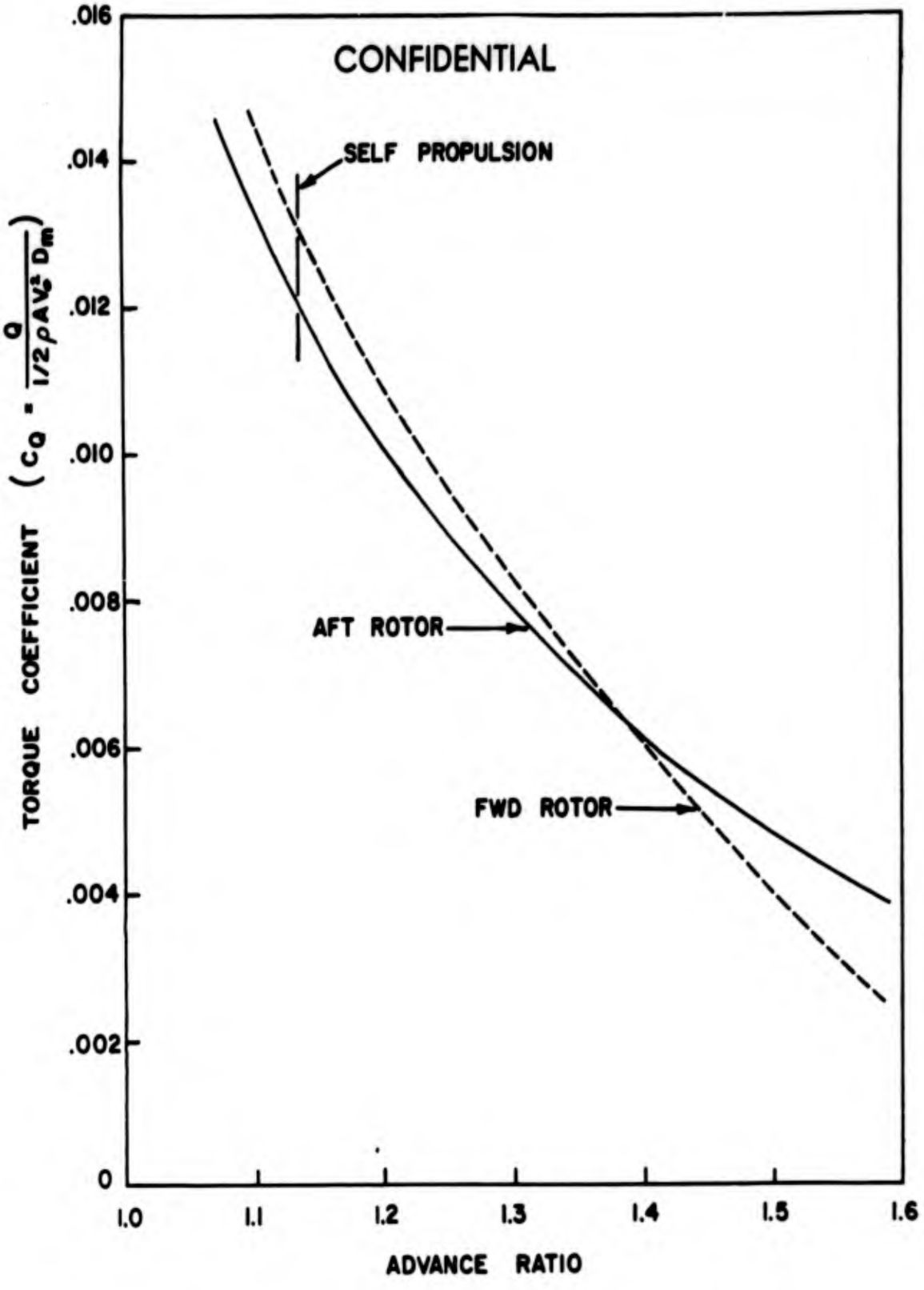

FIG. 21 BLADE TORQUE COEFFICIENT VS. ADVANCE RATIO

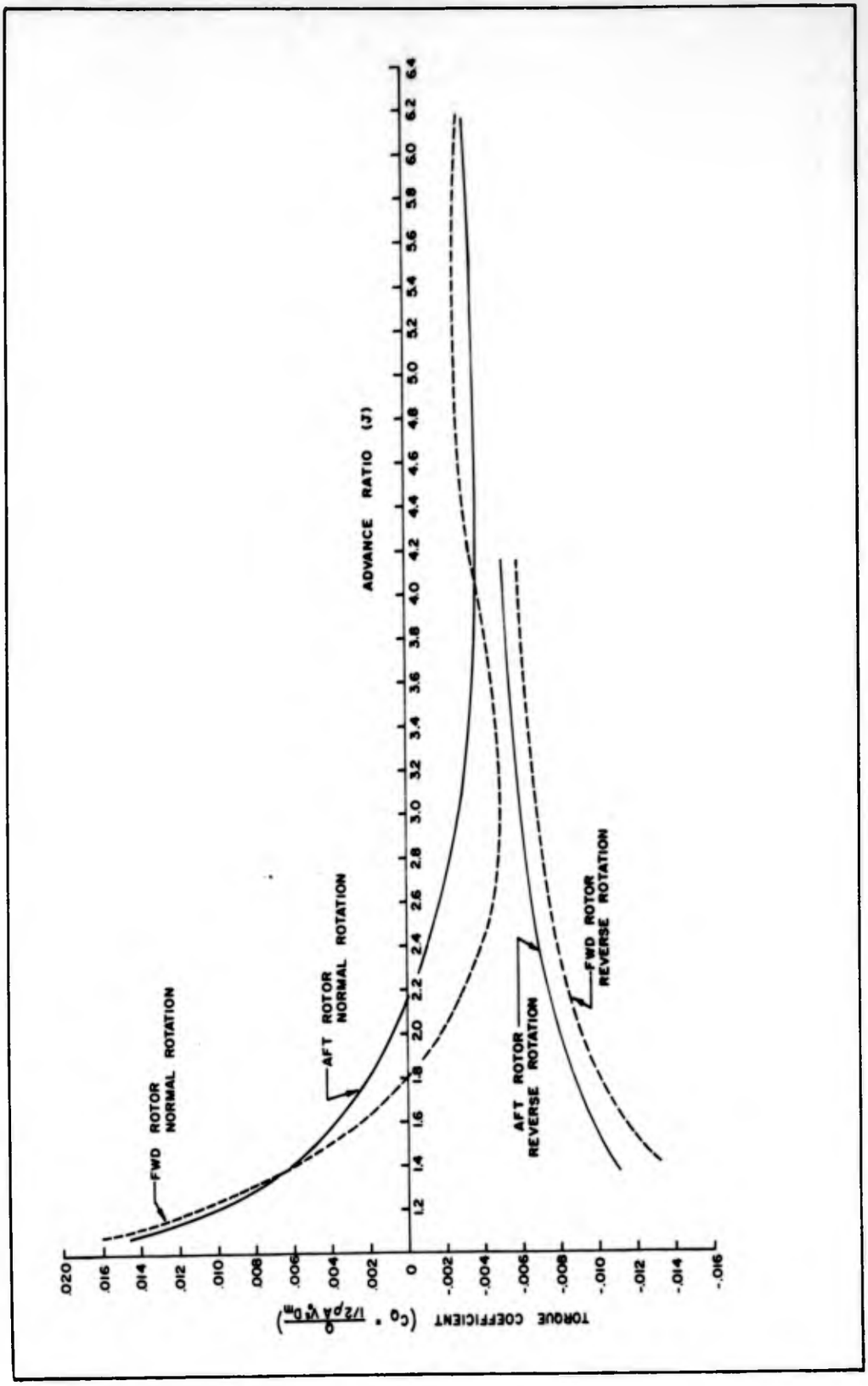

FIG. 22 BLADE TORQUE COEFFICIENT VS. ADVANCE RATIO (FULL RANGE)

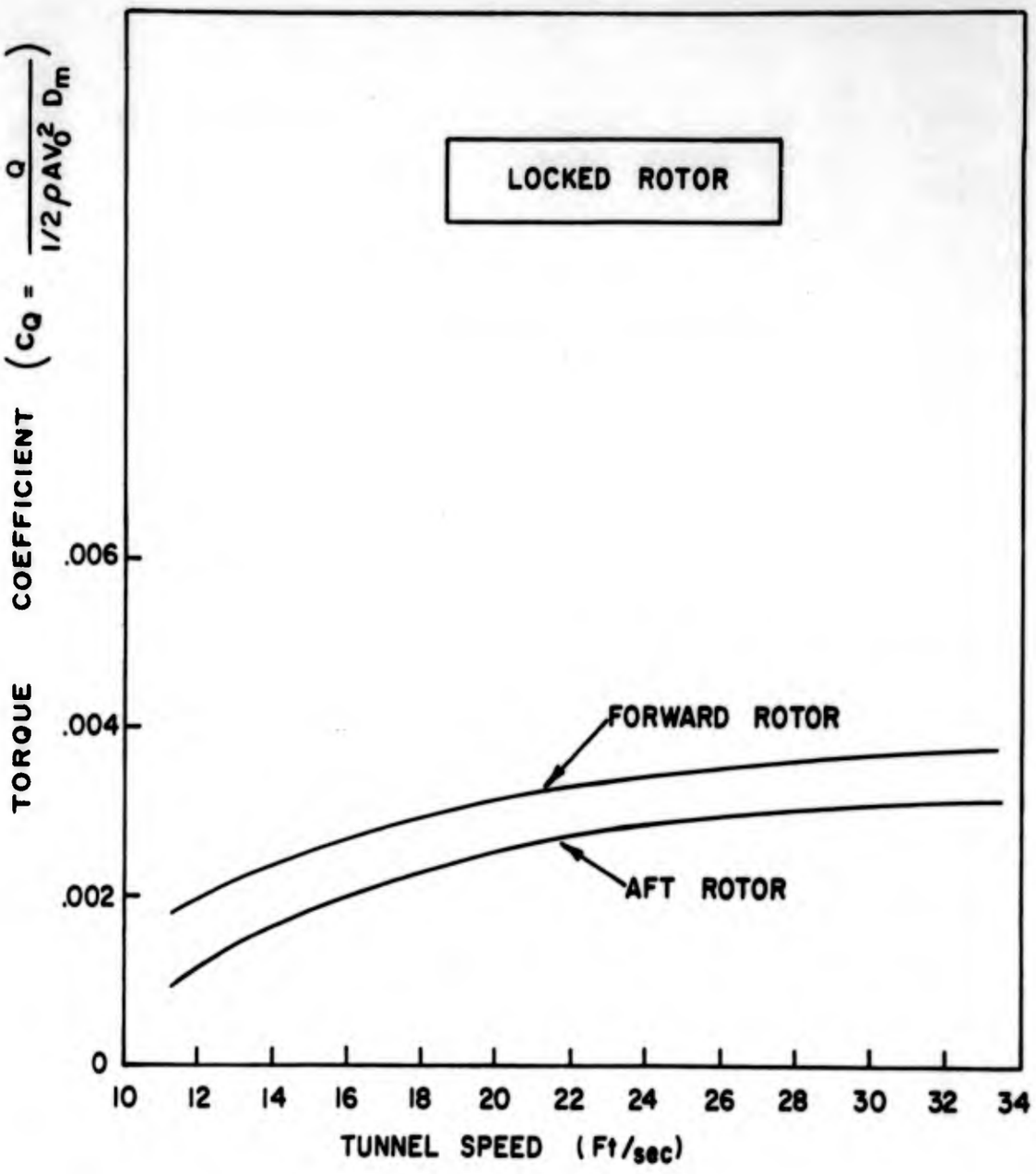

FIG. 23 TORQUE COEFFICIENT VS. TUNNEL SPEED (LOCKED ROTOR)

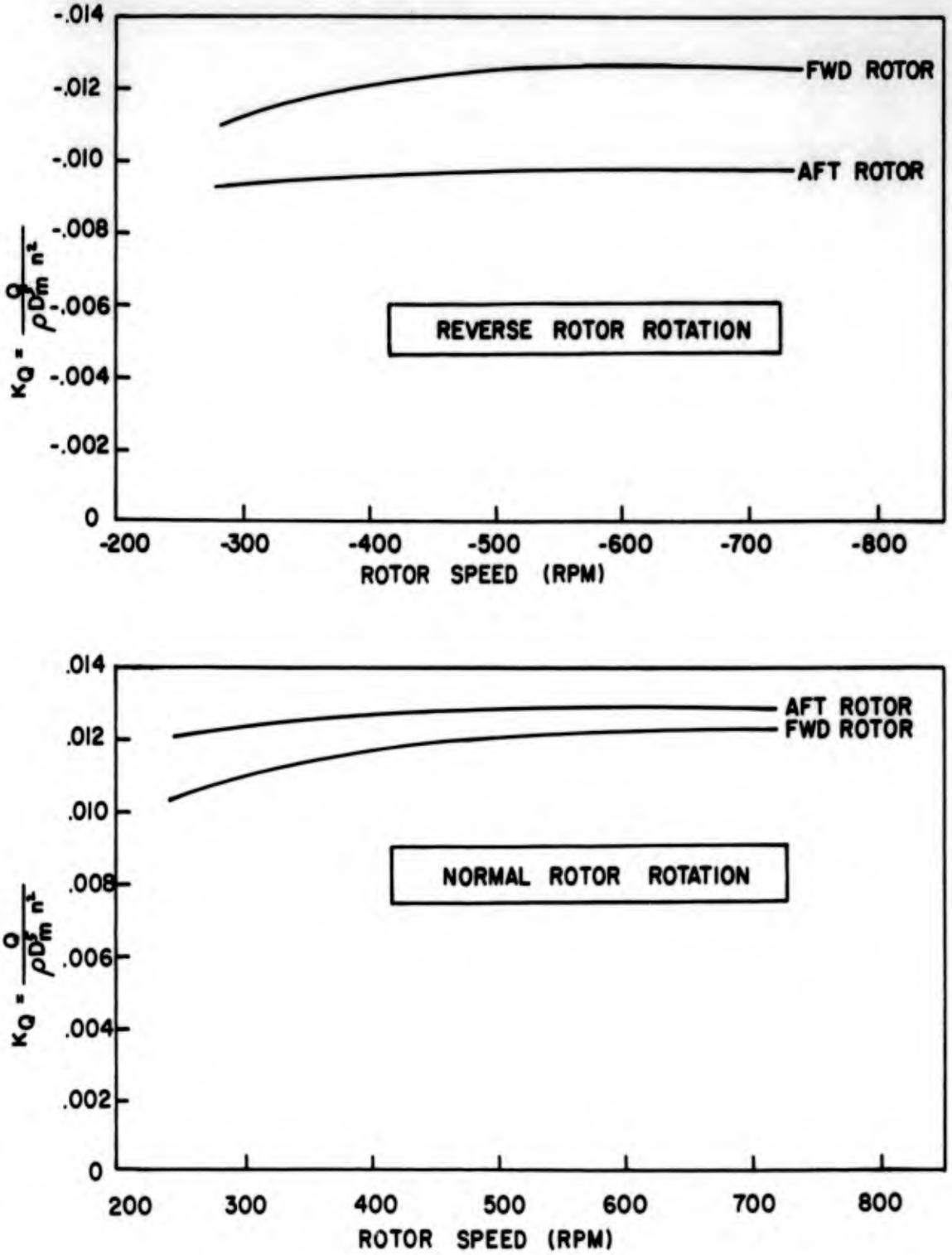

FIG. 24 BLADE TORQUE COEFFICIENT VS. ROTOR SPEED (ZERO TUNNEL FLOW)

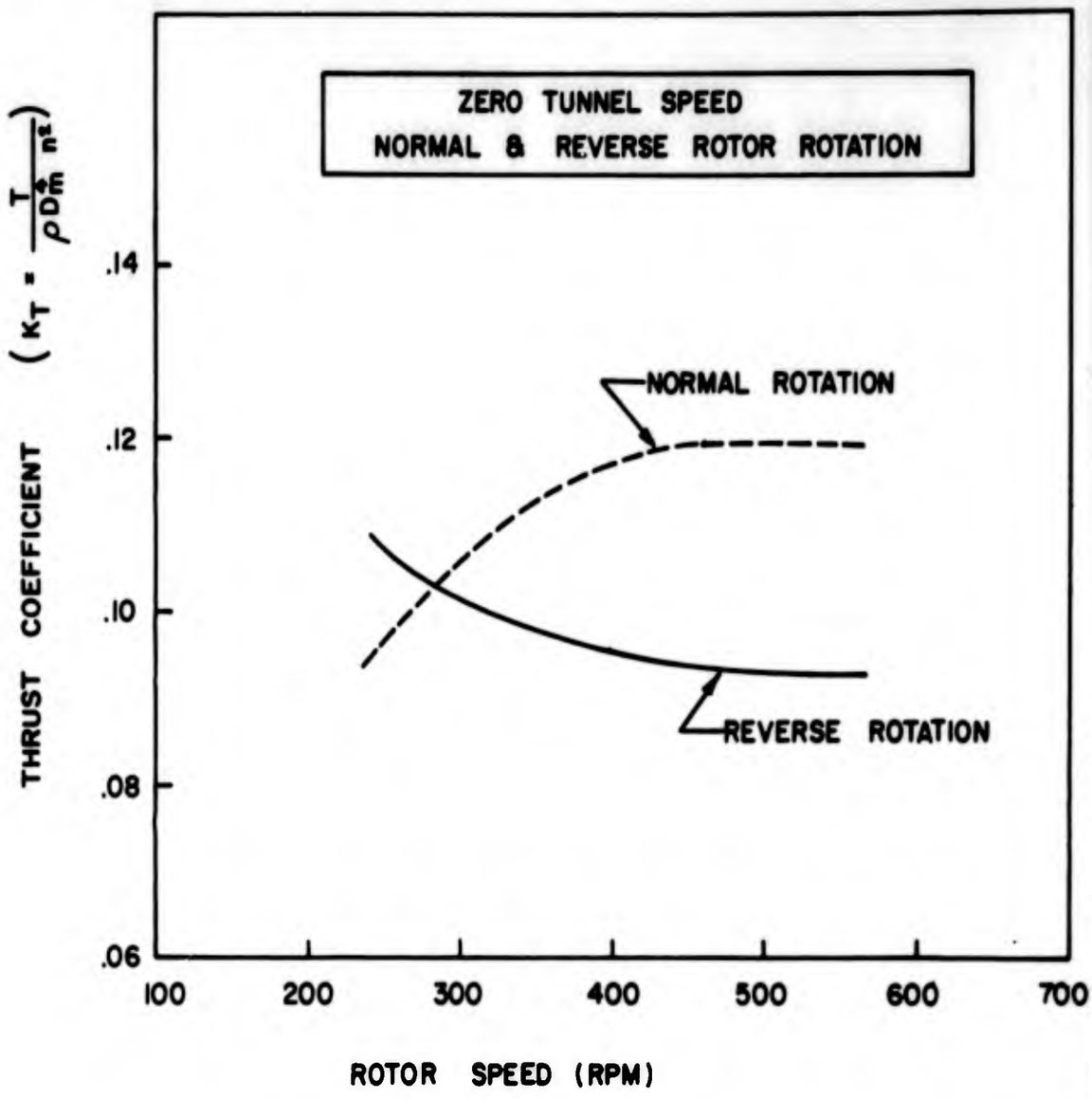

FIG. 25 THRUST COEFFICIENT VS. ROTOR SPEED (ZERO TUNNEL FLOW)

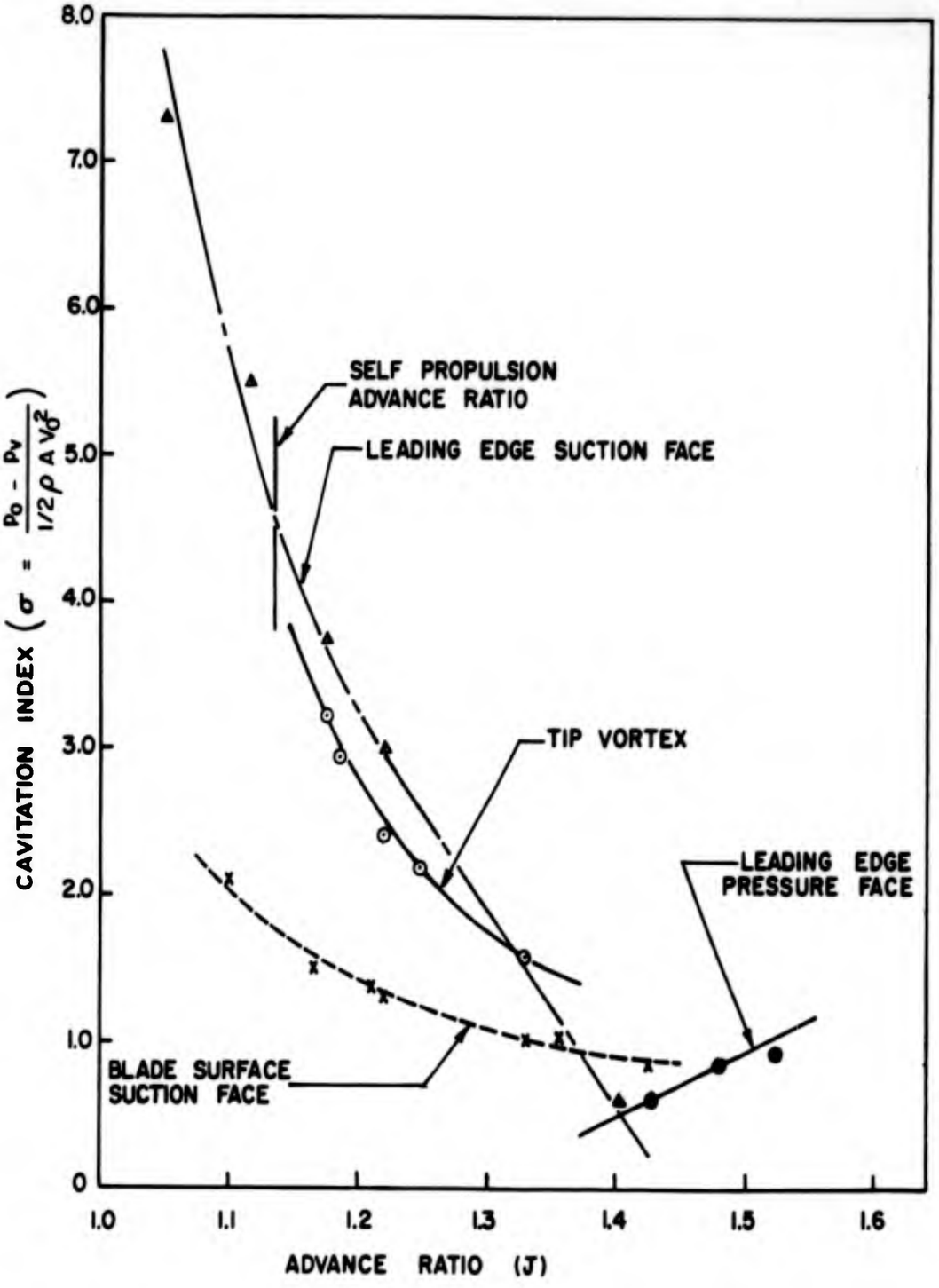

FIG. 26 CAVITATION INDEX VS. ADVANCE RATIO, FORWARD ROTOR

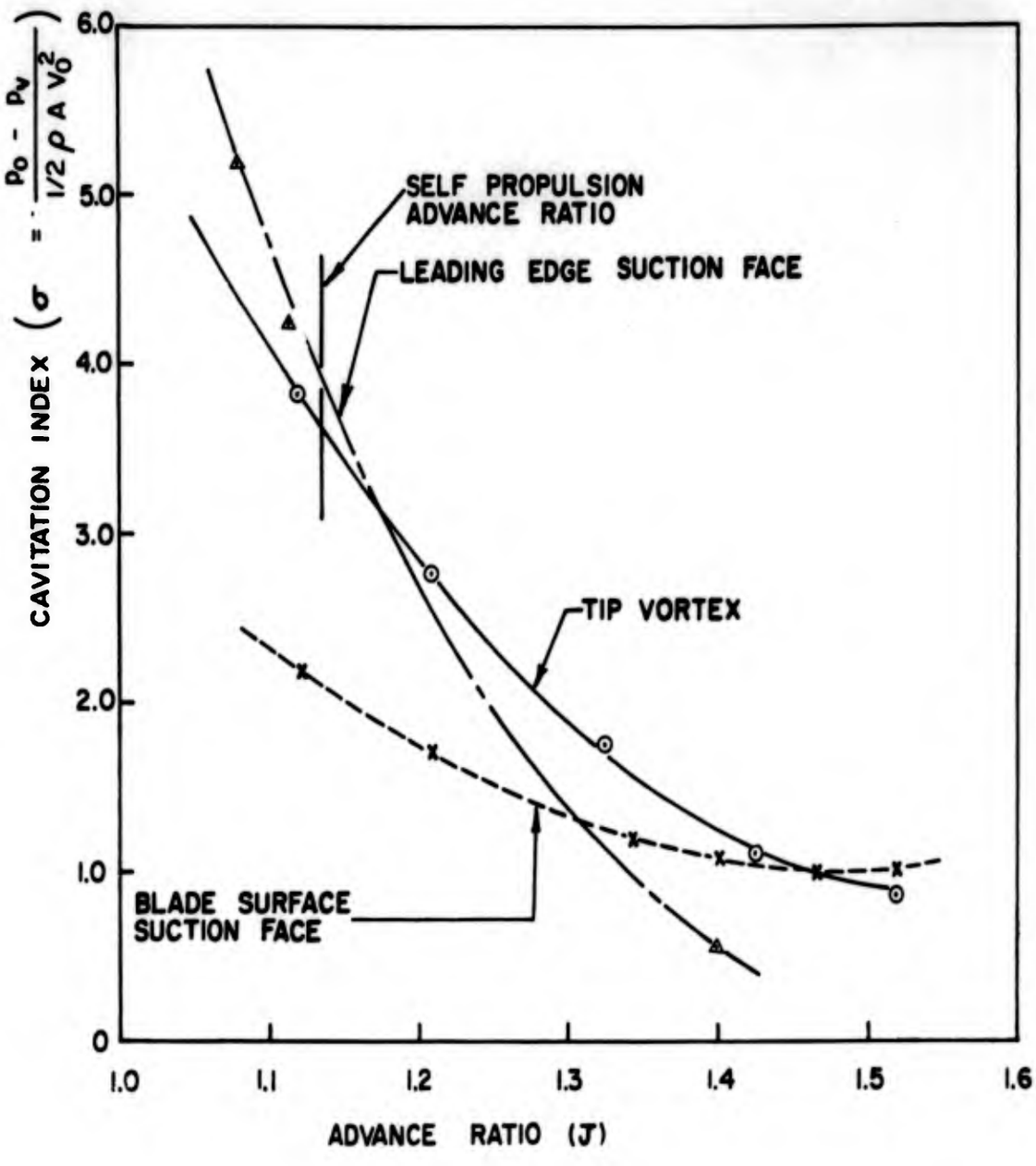

FIG. 27 CAVITATION INDEX VS. ADVANCE RATIO, AFT ROTOR

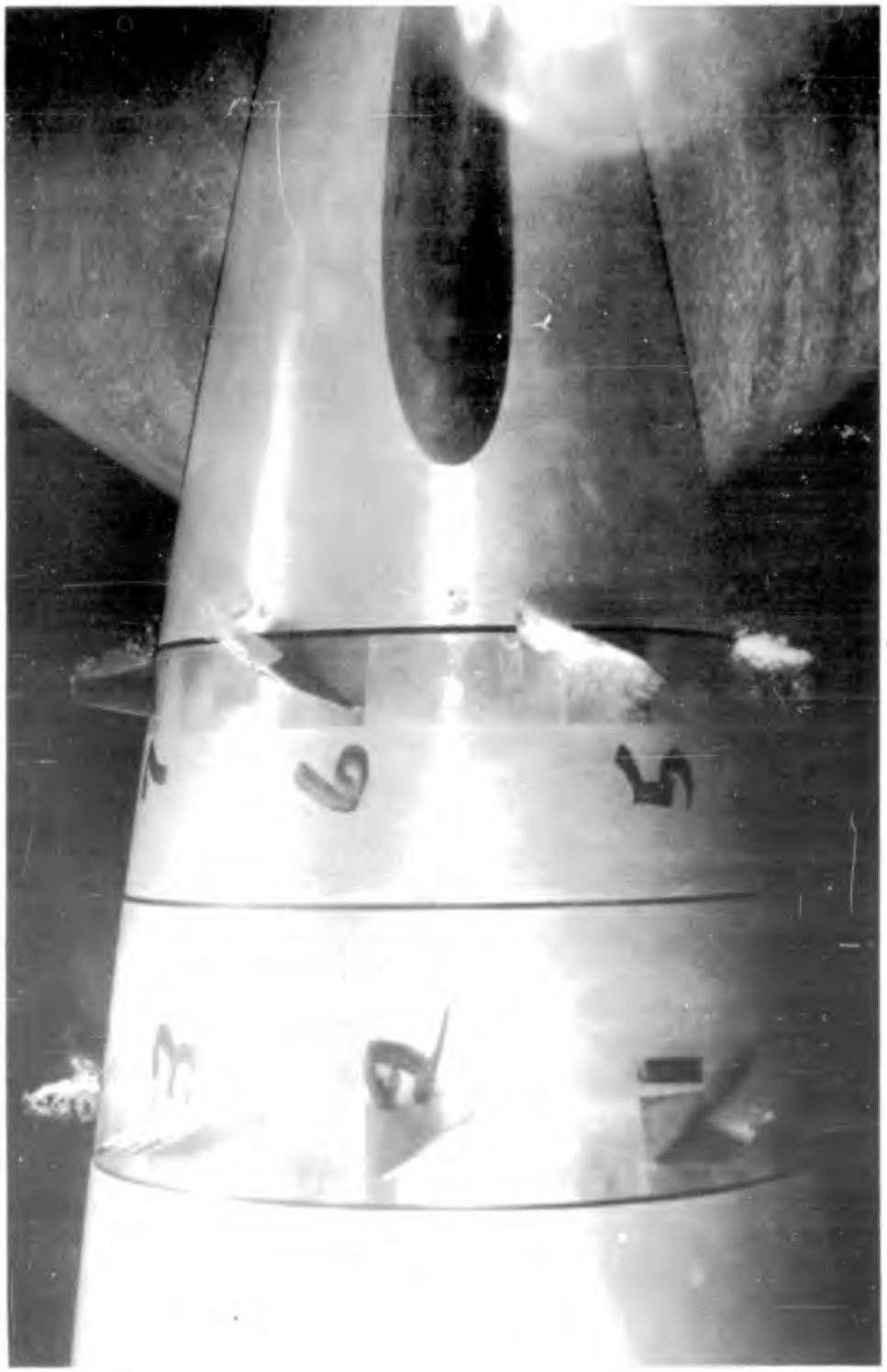

FIG. 28 TYPICAL BLADE SUCTION FACE CAVITATION

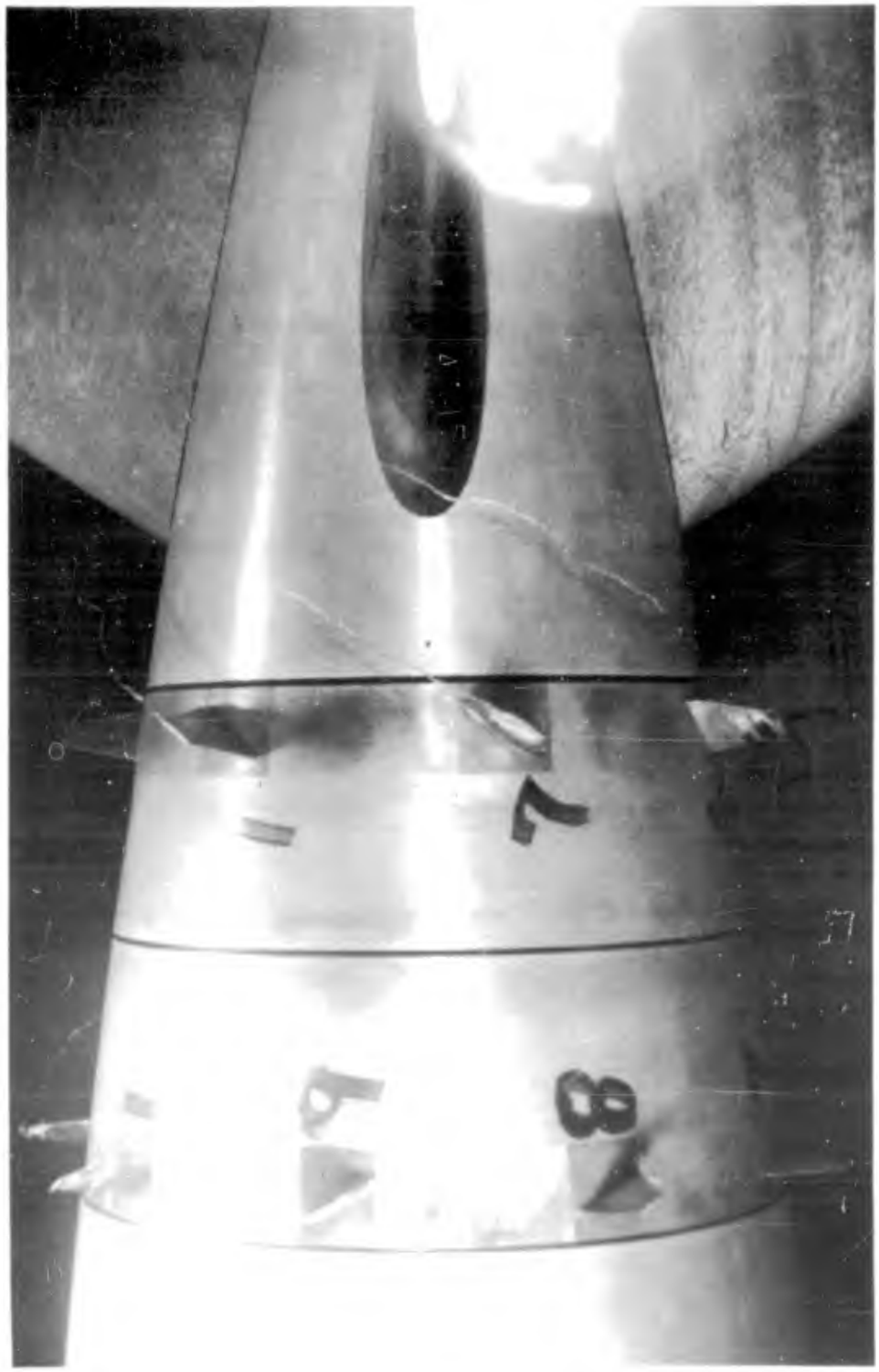

FIG. 29 TYPICAL BLADE TIP VORTEX CAVITATION

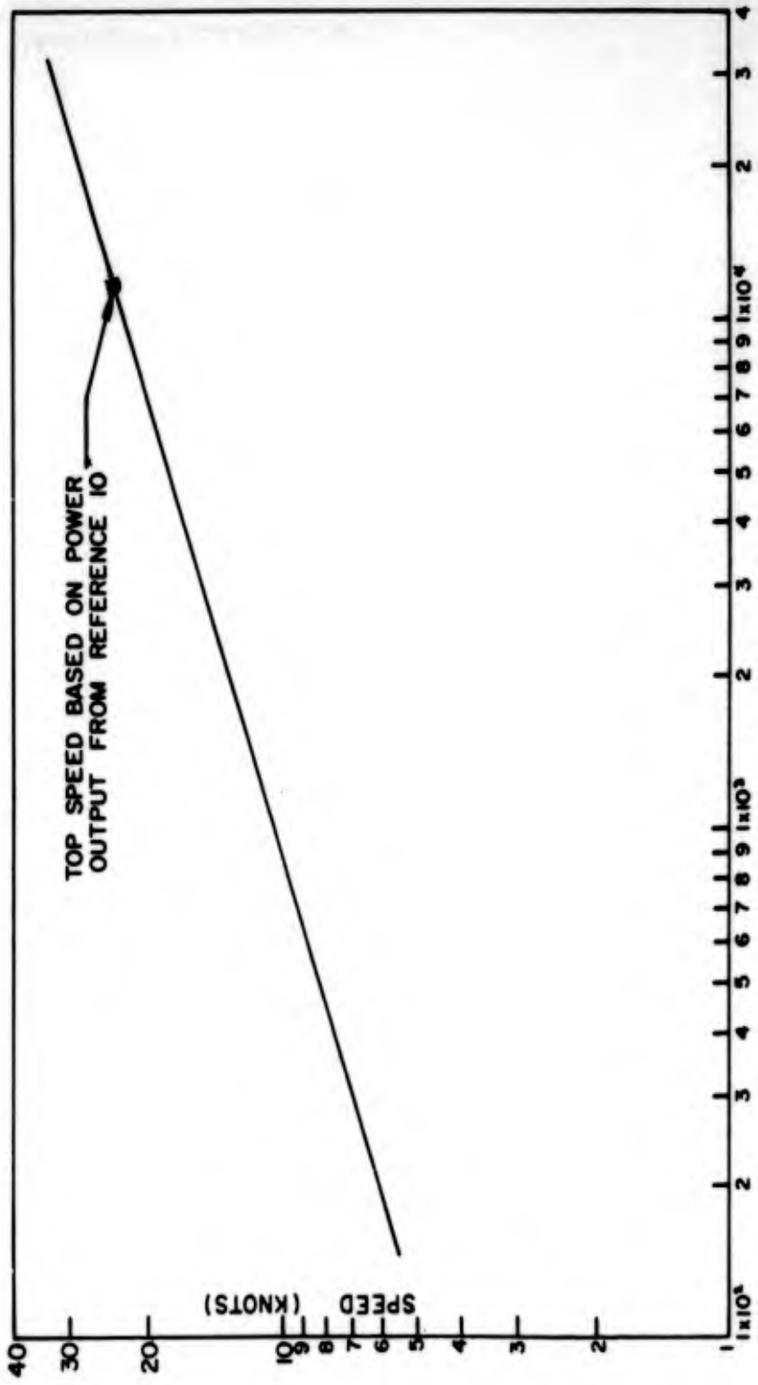

FIG. 30 PREDICTED PROTOTYPE PERFORMANCE CURVE

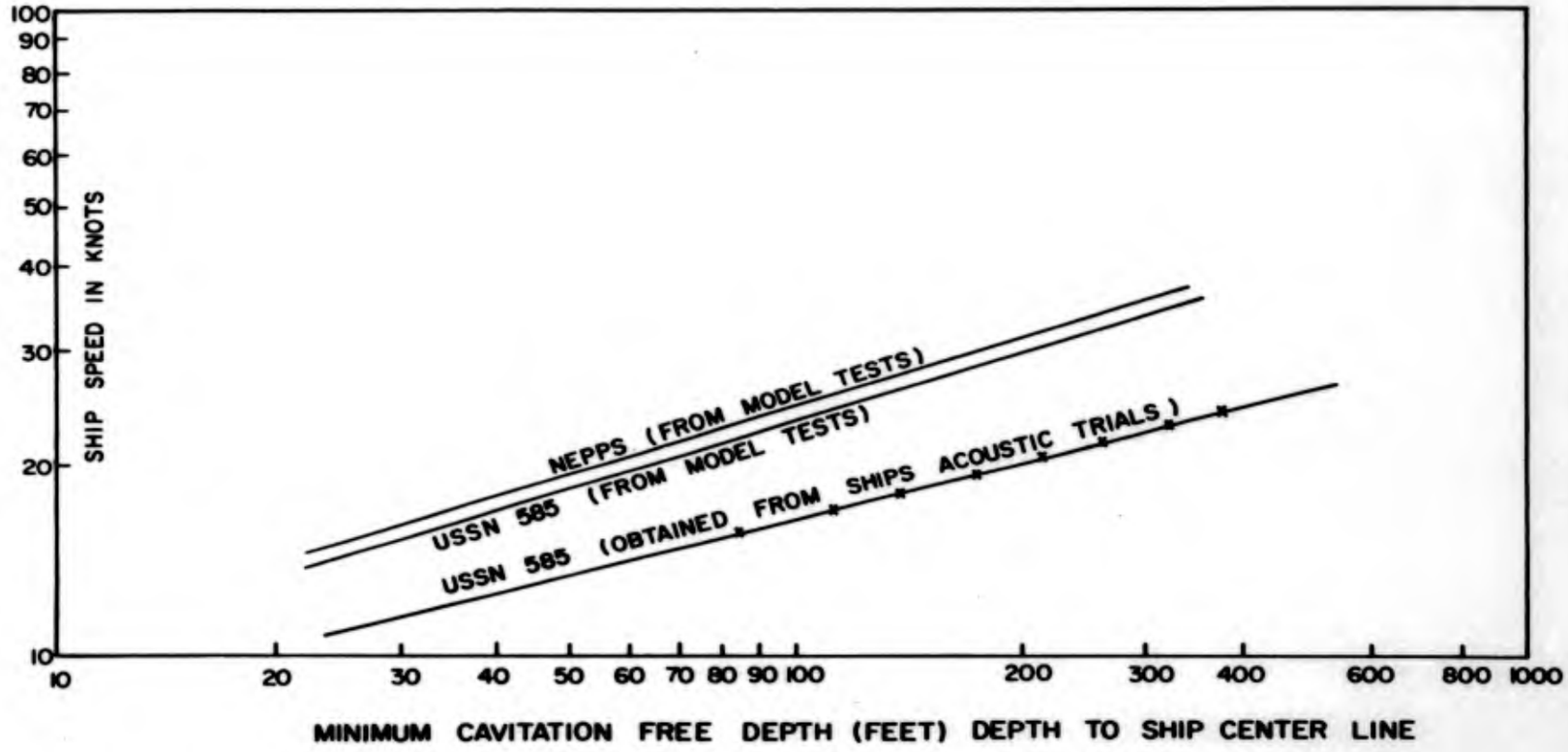

FIG. 31 CAVITATION FREE DEPTH VS. SHIP SPEED

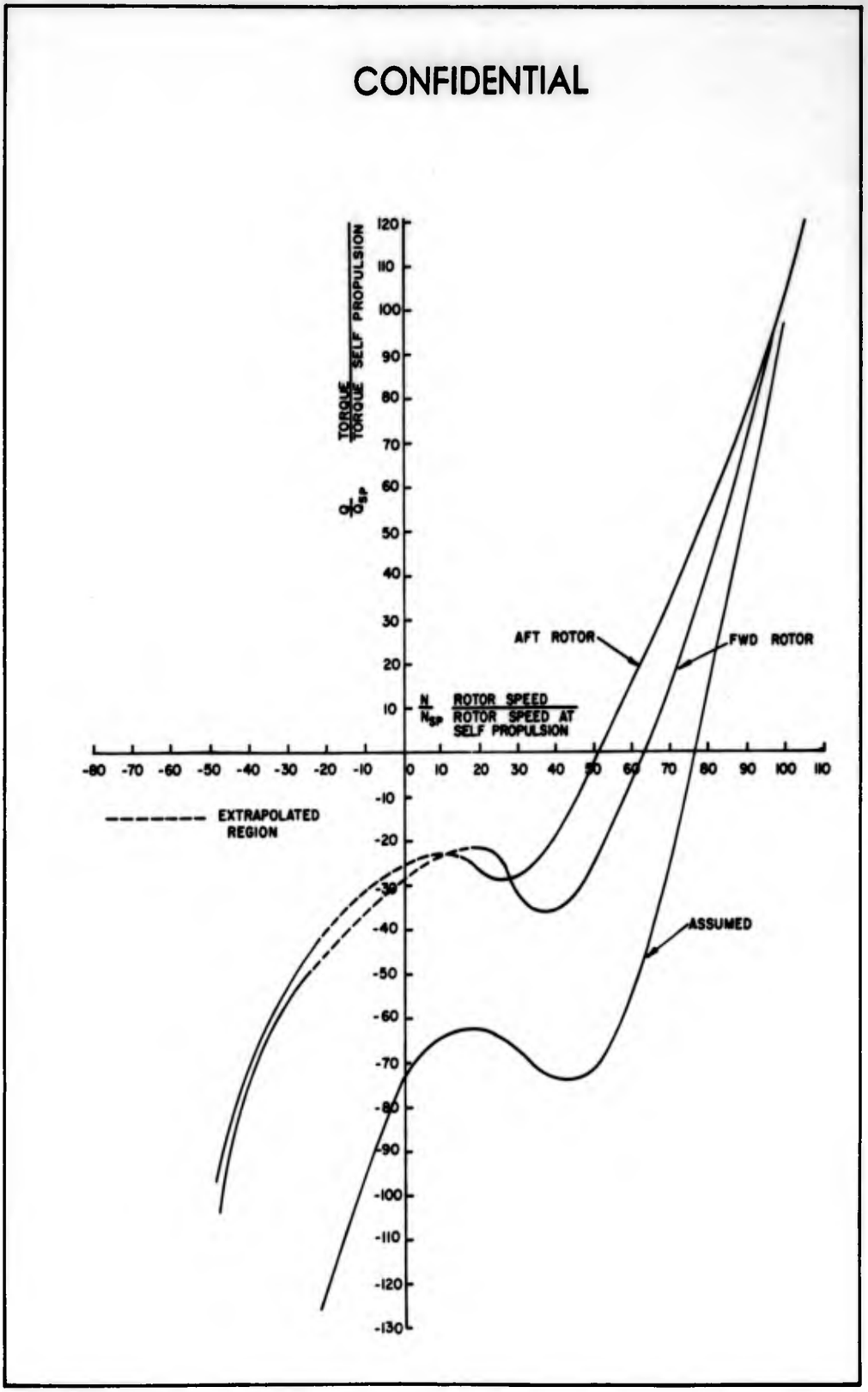

FIG. 32 PROPELLER TORQUE VS. ROTOR SPEED FOR 100% SHIP SPEED

TABLE - I
NEPPS HULL OFFSETS

x/L	y/D	x/L	y/D
.0	.0	.51700000	.50000000
.00174000	.065499993	.53200000	.49963710
.00433400	.10279103	.56650000	.49631661
.00867000	.14402163	.60120000	.48998591
.01730000	.19968431	.63590000	.48102295
.02600900	.24031413	.67060000	.46947929
.03468000	.27243328	.70520000	.45512912
.04337000	.29914065	.73990000	.43730608
.05202000	.32176564	.77460000	.41517204
.06936000	.35856095	.80930000	.38759013
.08670000	.38717884	.84390000	.35329051
.12140000	.42840657	.87860000	.31043750
.15610000	.45578603	.91330000	.25706686
.19070000	.47428437	.93060000	.22564366
.22540000	.48676502	.94800000	.19002015
.26010000	.49472550	.95660000	.17059543
.29480000	.49899440	.96530000	.14940009
.32200000	.50000000	.97400000	.12618291
.33303000	.50000000	.98270000	.099980579
.35000000	.50000000	.99130000	.068522231
.40000000	.50000000	.99570000	.047222123
.45000000	.50000000	.99820000	.030184708
.50000000	.50000000	1.00000000	.0

Tail Radius $\frac{RL}{D^2} = 0.248446$

Nose Radius $\frac{RL}{D^2} = 1.24223$

TABLE - II
BODY CHARACTERISTICS

	Model	Prototype
Overall Length (ft)	10.71	300
Maximum Diameter (ft)	1.23	34.5
Bare Body Surface Area (ft^2)	34.375	26,950.
Total Surface Area (ft^2)	38.000	29,792.
Finness Ratio (L/D)	8.79	8.79

TABLE - III
PROPELLER GEOMETRY

	Model		Prototype	
	Fwd	Aft	Fwd	Aft
Tip Diameter (ft)	1.004	0.882	28.11	24.69
Hub Diameter (ft)	0.829	0.695	23.21	19.46
Rotor Speed (rpm)	-	-	50	50
Number of Blades	9	7	9	7
Root Cord (ft)	0.074	0.0948	2.065	2.654
Tip Cord (ft)	0.033	0.042	0.903	1.161
Thickness Ratio (t/c)	0.1	0.1	0.1	0.1
Blade Form	NACA 65 series			

APPENDIX C

Counter-rotating Propeller Design Method

by

Q. R. Wald

NOMENCLATURE

B - Number of blades in one propeller

C_L - Lift coefficient

C_T - Thrust coefficient, $T/\frac{1}{2}\rho\pi\Omega^2R^4$

C_Q - Torque coefficient, $Q/\frac{1}{2}\rho\pi\Omega^2R^5$

c - Blade chord

Q - Torque

R - Radius to outer boundary of the trailing vortex sheets

r - Radial coordinate

T - Thrust

U - Resultant velocity in a plane normal to a radius

V - Stream velocity parallel to the z axis

v - Axial velocity of trailing vortex system relative to the surrounding fluid

w - Induced velocity

w_θ - Tangential component of induced velocity on the vortex sheet far downstream

w_z - Axial component of induced velocity on the vortex sheet far downstream

x - = r/R, non-dimensional radial coordinate

z - Axial coordinate

Γ - Circulation

δ - Induced axial velocity factor

ϵ - Section profile drag/lift ratio, c_d/c_ℓ

K - Circulation factor for finite number of blades

λ - Advance ratio $V/\Omega R$

μ - Non-dimensional axial velocity of vortex sheets, $v/\Omega R$

ρ - Fluid mass density

φ - Helix angle of the trailing vortex sheets

φ_1, φ_2 - Helix angles of resultant relative velocity at the propeller

Ω - Angular velocity of propeller

Subscripts

1 - At forward propeller or on vortex sheet shed by it

2 - At aft propeller or on vortex sheet shed by it

No subscript generally indicates conditions in the wake

Counter-rotating Propeller Design Method

General Principles

The design of a wake adapted counter-rotating propeller with large diameter hub is a somewhat unusual problem requiring modifications to usual propeller design methods. It was decided that the complexities could be minimized by a vortex analysis beginning with the theorem of Betz:*

> "For a propeller with the circulation distributed along the blade in such a way that, for a given thrust, the energy loss is a minimum, the flow far behind the propeller is the same as if the vortex sheet formed by the trailing vortices was a solid membrane moving backwards in the direction of its axis with constant velocity."

The propeller analysis and design accordingly proceed from a computation of the induced velocities on a symmetrical set of intersecting right and left hand helical vortex sheets of equal pitch and diameter. The induced velocities are proportional to the relative backward velocity v of the helical vortex sheets; hence the velocity of the vortex sheets is the most convenient independent variable in the design problem. By considerations of circulation on appropriate paths of integration and by continuity the induced velocity and circulation at a blade element may be related to the induced velocity on the vortex sheet. Consequently, the circulation and induced velocity at each blade element is finally obtained as a function of the single independent variable v. The thrust and torque of the blade element then follow very simply from the Kutta-Joukowski theorem. The total thrust and torque are then obtained by integration.

The general procedure outlined above makes it unnecessary to solve directly the problem of the optimum circulation on a counter-rotating propeller with a large hub, since an optimum condition can be established on the ultimate wake where the vortex sheets extend into the axis. Admittedly, approximations are involved in relating the propeller to the wake.

*Betz, A.; "Schraubenpropeller mit Geringstem Energieverlust," Göttinger Nachr., 1919, p. 193. Also see: Durand, "Aerodynamic Theory," vol. 4, page 254.

The Prandt-Betz circulation function has been used to account for the effect of a finite number of blades.

The computations were carried out on a high speed digital computer starting with an arbitrarily assumed value of the vortex sheet velocity V + v. The resulting thrust is compared with the desired value, the magnitude of V + v adjusted accordingly, and a new solution is computed. The final solution for circulation, torque, and induced velocities at a blade element for the required total thrust is thus arrived at by an iteration process.

The analysis is essentially a lifting line method, but a camber correction for stream curvature is applied in the final stages of the design.

A brief outline of the essentials of the analysis and a summary of the basic equations follows. It is anticipated that the complete analysis and design procedure will eventually be issued as a separate report.

Velocities induced by the vortex sheets

We consider a cylindrical section r = constant through the system of right and left hand helical vortex sheets which translate axially at a velocity v relative to the fluid in the wake.

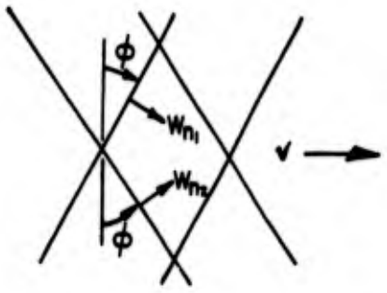

FIG. 1

The component of velocity W_{n_1} normal to one vortex sheet at its surface must be equal to v cosφ. The velocity W_{n_1} is composed of the self-induced velocity $W_{n_{11}}$ which is normal to the sheet and $W_{n_{12}}$, a component of the induced velocity due to the vortex sheets of opposite rotation.

The latter component is $Kw_{n_{22}}\cos 2\varphi$ since 2φ is the angle between the two sets of helicoids. K is a reduction factor which is the ratio of the average velocity induced between the vortex sheets to the velocity on the surface of the sheets. Consequently,

$$w_{n_1} = v\cos\varphi = w_{n_{11}} + Kw_{n_{22}}\cos 2\varphi$$

$$w_{n_2} = v\cos\varphi = w_{n_{22}} + Kw_{n_{11}}\cos 2\varphi$$

Therefore, the induced component on either set of vortex sheets is

$$w_n = w_{n_{11}} = w_{n_{22}} = \frac{v\cos\varphi}{1+K\cos 2\varphi}$$

The axial induced velocity is then

$$w_z = w_n\cos\varphi = \frac{v\cos 2\varphi}{1+K\cos 2\varphi} \qquad (1)$$

and the tangential component is

$$w_\theta = w_n\sin\varphi = \frac{v\sin\varphi\cos\varphi}{1+K\cos 2\varphi} \qquad (2)$$

The pitch of the helix is given by

$$\tan\varphi = (V+v)/\Omega r \qquad (3)$$

Neglecting the effect of radial displacement of vortex filaments due to slipstream contraction or the influence of the propeller hub, the velocities induced at the propeller are those at the terminal edges of a semi-infinite set of helical vortex sheets. Since there is screw symmetry, these velocities are one half those at an infinitely long sheet or one half of those existing far downstream (Figure 2). The effect of changes in the radial coordinate of a vortex filament may be accounted for by maintaining constant circulation around the propeller axis. This requires that the tangential velocity at a vortex filament

FIGURE 2

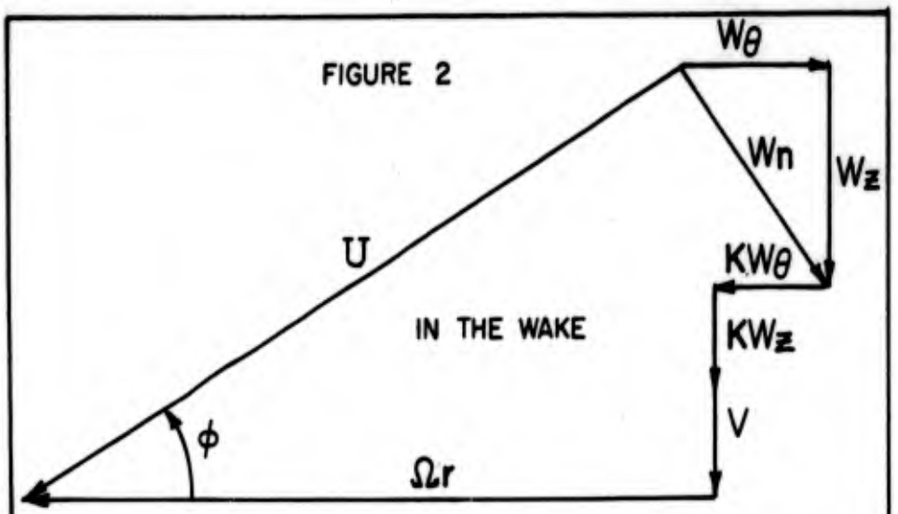

FIGURE 3A

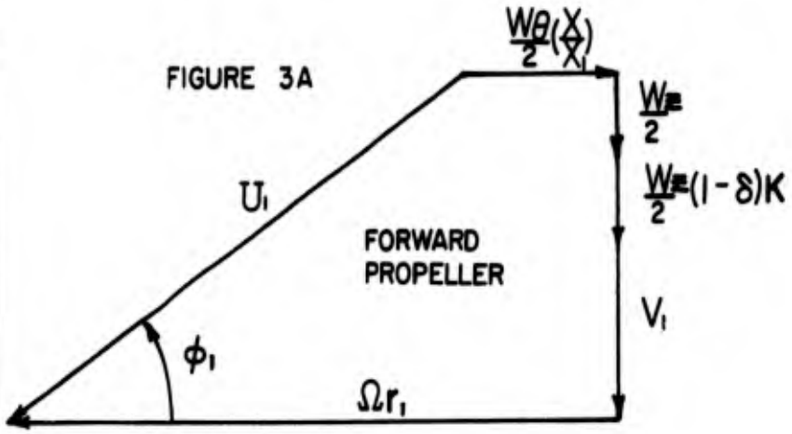

FIGURE 3B

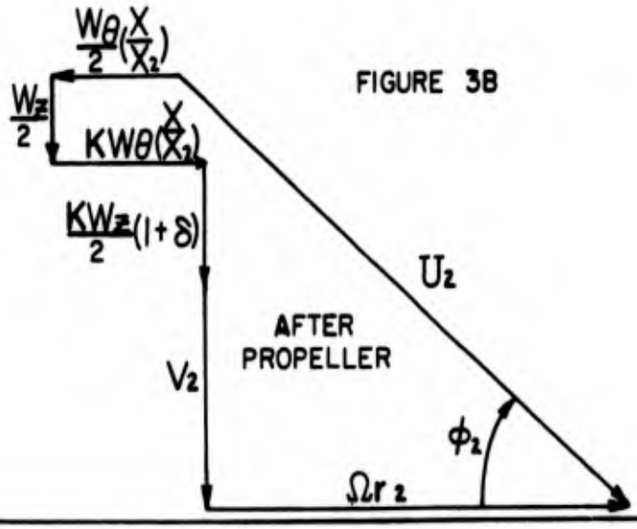

vary inversely as the radius when it is displaced. The velocities at the propeller blades are then as shown in figure 3. The factor δ arises due to the finite distance between the propellers.

Thrust and Torque Gradients

The thrust and torque gradients at any radius on the propeller blade may now be evaluated. The axial and tangential components of force may be written out from the Kutta-Joukowski law

$$\vec{F} = \rho \vec{U} \times \vec{\Gamma} \tag{4}$$

where u is the mean relative velocity. We may separately identify the axial and tangential forces by observing the component of velocity relative to the blade element which is normal to the force under consideration. The magnitude of u appropriate to each component of force may be written out directly by inspection of Figure 3. Primes are used to indicate that no account has been taken of profile drag. The number of blades in each propeller, B_1 and B_2, are introduced to give the total gradients for each propeller.

$$\left.\begin{aligned}
\frac{dT_1'}{dr_1} &= \rho B_1 \Gamma_1 \left[\Omega r_1 - \frac{w_\theta}{2} \frac{x}{x_1} \right] \\
\frac{dQ_1'}{dr_1} &= \rho B_1 \Gamma_1 \left[V_1 + \frac{w_z}{2} (1 + K - K\delta) \right] r_1 \\
\frac{dT_2'}{dr_2} &= \rho B_2 \Gamma_2 \left[\Omega r_2 + w_\theta \frac{x}{x_2} (K - \frac{1}{2}) \right] \\
\frac{dQ_2'}{dr_2} &= \rho B_2 \Gamma_2 \left[V_2 + \frac{w_z}{2} (1 + K + K\delta) \right] r_2
\end{aligned}\right\} \tag{5}$$

The bound circulation on a propeller blade at any radius is related to the induced velocity on the trailing vortex system in the wake by the relation

$$B_1 \Gamma_1 = B_2 \Gamma_2 = 2\pi r K w_\theta \tag{6}$$

where r is the radius to a vortex filament in the wake, and Γ_1 and Γ_2 is the circulation on the blade at the point from which the vortex filament originates.

Substituting (6) in (5) and expressing in non-dimensional form, we obtain

$$\left.\begin{aligned}
\left(\frac{dC'_{T_1}}{dx_1}\right) &= 4Kx\left(\frac{w_\theta}{\Omega R}\right)\left[x_1 - \tfrac{1}{2}\frac{x}{x_1}\frac{w_\theta}{\Omega R}\right] \\
\left(\frac{dC'_{Q_1}}{dx_1}\right) &= 4Kxx_1\left(\frac{w_\theta}{\Omega R}\right)\left[\lambda_1 + \tfrac{1}{2}\frac{w_z}{\Omega R}(1 + K - K\delta)\right] \\
\left(\frac{dC'_{T_2}}{dx_2}\right) &= 4Kx\left(\frac{w_\theta}{\Omega R}\right)\left[x_2 + \frac{x}{x_2}\frac{w_\theta}{\Omega R}(K - \tfrac{1}{2})\right] \\
\left(\frac{dC'_{Q_2}}{dx_2}\right) &= 4Kxx_2\left(\frac{w_\theta}{\Omega R}\right)\left[\lambda_2 + \tfrac{1}{2}\frac{w_z}{\Omega R}(1 + K + K\delta)\right]
\end{aligned}\right\} \qquad (7)$$

The induced velocities given by equations (1) and (2) may also be written in convenient non-dimensional form with the aid of equations (3) and trigonometric identities.

$$\left.\begin{aligned}
\frac{w_z}{\Omega R} &= \frac{\mu x^2}{(1+K)x^2+(1-K)(\lambda+\mu)^2} \\
\frac{w_\theta}{\Omega R} &= \frac{\mu x(\lambda+\mu)}{(1+K)x^2+(1-K)(\lambda+\mu)^2}.
\end{aligned}\right\} \qquad (8)$$

Equations (7) and (8) define the thrust and torque distribution on an ideal counter-rotating propeller without friction as a function of an independent variable μ, which determines the magnitude of the thrust and torque. The factor K is a function of the advance ratio λ and the number of blades, while δ is a function of the axial spacing of the propellers. The thrust and torque gradients at radial coordinates x_1 and x_2 are expressed as functions of μ, λ and K at the corresponding radial coordinate x in the wake.

The friction forces on the propeller blades may now be introduced. It can be shown that the net thrust and torque gradients with friction are related to the frictionless gradients by the following relations.

$$\left.\begin{aligned}
\frac{dC_{T_1}}{dx_1} &= \left(\frac{dC'_{T_1}}{dx_1}\right) - \frac{\epsilon_1}{x_1}\left(\frac{dC'_{Q_1}}{dx_1}\right) \\
\frac{dC_{Q_1}}{dx_1} &= \left(\frac{dC'_{Q_1}}{dx_1}\right) + \epsilon_1 x_1 \left(\frac{dC'_{T_1}}{dx_1}\right) \\
\frac{dC_{T_2}}{dx_2} &= \left(\frac{dC'_{T_2}}{dx_2}\right) - \frac{\epsilon_2}{x_2}\left(\frac{dC'_{Q_2}}{dx_2}\right) \\
\frac{dC_{Q_2}}{dx_2} &= \left(\frac{dC'_{Q_2}}{dx_2}\right) + \epsilon_2 x_2 \left(\frac{dC'_{T_2}}{dx_2}\right)
\end{aligned}\right\} \qquad (9)$$

where ϵ_1 and ϵ_2 are the profile draft/lift ratios of the blade sections.

The total thrust and torque of each propeller is obtained by integrating the gradients from the hub to the tip.

In the application of these equations to a propeller running in an axi-symmetric wake, the condition stated by Betz and quoted above is met when V + v is held constant where V is a function of r. Consequently, $\lambda + \mu$ is held constant while λ varies with r according to the distribution of velocities in the axi-symmetric wake or boundary layer. The computed boundary layer profile in which the NEPPS propeller operates is of the power law type where $v/v_o = (y/\delta)^{1/5}$. The entire propeller is within the boundary layer.

In the iteration solution of the equations, successive constant values of $\lambda + \mu$ are assumed.

The efficiency of the propeller, neglecting hub friction, is $\eta = \lambda_o C_T/C_Q$. The propeller blade efficiency was found to be very high in the present case, but large hydrodynamic losses associated with the hub and massive internal rotating components were severely compromising. The necessity of keeping these to reasonable magnitudes dictated the use of a relatively low rotational speed of 50 rpm.

Determination of Propeller Geometry

The foregoing discussion indicates how the induced velocities and circulation at the propeller blade at any radius r are determined for a given thrust requirement. It remains to relate the geometry of the blade to the velocity and circulation information.

From equation (4) and the definition of lift coefficient we obtain the relation

$$BC_L c = 2B\Gamma/U \qquad (10)$$

Hence the product of lift coefficient, number of blades, and chord are readily determined at each radial station. The individual magnitudes of these quantities is, to a certain extent, a matter of choice. Lift coefficient must be kept to a moderately low value to obtain good cavitation characteristics. The number of blades is influenced by considerations of finite blade number effects and blade rate noise, and chord is influenced by considerations of structural stiffness of the blades.

It may be shown that the change in axial velocity is small in the neighborhood of the blades, while all of the tangential velocity is acquired in passing through the blades. From these facts the change in mean relative velocity in passing through each propeller may be readily computed from the known induced velocities. The mean camber of each blade section is then constructed upon a parabola, the tangents at the ends of which are parallel to the computed relative inflow and outflow velocities. The ordinates of the camber line for the desired chordwise loading of the blade are added to the ordinates of the parabola (relative to its chord). In the present design an NACA a=1 type camber (corresponding to a uniform chordwise loading) was used. The thickness distribution is NACA 65-010.

UNCLASSIFIED